

MULTISCALE MODELING OF FREE-RADICAL POLYMERIZATION KINETICS

A Thesis
Presented to
The Academic Faculty

by

Jonathan A. Rawlston

In Partial Fulfillment
of the Requirements for the Degree
Doctor of Philosophy in the
School of Chemical and Biomolecular Engineering

Georgia Institute of Technology
May 2010

MULTISCALE MODELING OF FREE-RADICAL POLYMERIZATION KINETICS

Approved by:

Professor F. Joseph Schork,
Committee Chair
School of Chemical and Biomolecular
Engineering
Georgia Institute of Technology

Professor Martha Grover, Advisor
School of Chemical and Biomolecular
Engineering
Georgia Institute of Technology

Professor Haskell Beckham
School of Polymer, Textile, and Fiber
Engineering
Georgia Institute of Technology

Professor Yulin Deng
School of Chemical and Biomolecular
Engineering
Georgia Institute of Technology

Professor Peter Ludovice
School of Chemical and Biomolecular
Engineering
Georgia Institute of Technology

Date Approved: 4 March 2010

ACKNOWLEDGEMENTS

First of all, I would like to thank my advisor, Dr. Martha Grover, for her encouragement and guidance throughout my time at Georgia Tech. Her enthusiasm for research is truly contagious, keeping me inspired whenever days and weeks of coding turned into months. I am also indebted to my co-advisor Dr. F. Joseph Schork, who has maintained a high level of involvement in my research in spite of living in another city for the past 3+ years and having the responsibilities of a department chair. I am honored to be his final graduate student. Both Dr. Grover and Dr. Schork encouraged me to spend a summer abroad doing research at Imperial College London, and for that encouragement I will be forever grateful, as my experiences during those three months changed my perspective on both research and life in general.

I would like to thank my committee members, Dr. Haskell Beckham, Dr. Yulin Deng, and Dr. Peter Ludovice, for their support during my time here and for making themselves available to answer any of my questions.

I would like to thank Dr. Paul Wissmann for being such a good listener and a good friend. I would also like to thank him for being on vacation when we moved out of the window-less office, so that I could get the best spot in the new office. I owe thanks to Dr. Cihan Oguz and Dr. Rentian Xiong for being such tireless researchers and inspiring me to be the same. I thank Aparna Boddapati for being a good office mate while we both worked to conclude our studies, and Andres Felipe Hernandez Moreno for his willing input on programming issues.

Last but not least, I would like to thank my parents and my grandparents for their continued support during my time in graduate school and for always believing in me. Their desire for me to succeed has been a tremendous positive reinforcement.

TABLE OF CONTENTS

ACKNOWLEDGEMENTS	iii
LIST OF TABLES	vii
LIST OF FIGURES	viii
SUMMARY	xiv
I INTRODUCTION	1
1.1 Scope	4
1.2 Summary	6
II LITERATURE REVIEW	10
2.1 Polymerization Systems	10
2.1.1 Solution Polymerization	10
2.1.2 Emulsion Polymerization	10
2.1.3 Miniemulsion Polymerization	12
2.2 Spatial Modeling of Polymer Chains	19
2.3 Key Aspects of Polymer Modeling	21
2.3.1 Molecular Weight Distribution	21
2.3.2 Particle Morphology	22
2.3.3 Branching Models	24
2.4 Branching in Butyl Acrylate	25
III SPATIALLY-RESOLVED MODEL	29
3.1 Introduction	29
3.2 Modeling Approach	29
3.2.1 Model Arrays and Algorithm	30
3.2.2 Polymer Diffusion	32
3.2.3 Reactions	37
3.3 Combined Reaction and Diffusion Modeling	40
3.4 Cumulative Distribution Function for Backbiting	41

IV	WELL-MIXED MODELS	45
4.1	Well-Mixed Discrete Model	45
4.1.1	Introduction	45
4.1.2	Modeling Approach	45
4.1.3	Viscosity	54
4.2	Well-Mixed Rate-Equation Model	56
4.2.1	Introduction	56
4.2.2	Rate Equations	57
4.2.3	Branch Length	60
V	EXAMINATION OF THE NUCLEATION MECHANISMS OF OIL-SOLUBLE INITIATORS	63
5.1	Background	63
5.1.1	Motivation	63
5.1.2	Well-Mixed Assumption	65
5.2	Rate Constants	66
5.3	Chain-Stopping Mechanisms	70
5.4	Experimental Procedure	73
5.5	Experimental Results	74
5.6	Simulation Results	78
5.7	Conclusions	87
VI	EXAMINATION OF THE BRANCH-LENGTH DISTRIBUTION IN BUTYL ACRYLATE USING THE RATE-EQUATION MODEL	89
6.1	Rate Constants	90
6.2	Comparison to Experimental Data	93
6.3	Branching Predictions	96
6.4	Viscosity Predictions	107
6.5	Conclusions	110
VII	EXAMINATION OF THE BRANCH-LENGTH DISTRIBUTION IN BUTYL ACRYLATE USING THE WELL-MIXED DISCRETE MODEL	112

7.1	Rate Constants	112
7.2	Comparison to Experimental Data	116
7.3	Branching Predictions	122
7.4	Viscosity Predictions	130
7.5	Conclusions	134
VIII	CONCLUSIONS AND FUTURE DIRECTIONS	135
8.1	Conclusions	135
8.2	Future Directions	137
	REFERENCES	141

LIST OF TABLES

1	Macroscopic and molecular rate equations for spatially-resolved model.	38
2	Macroscopic and molecular rate equations for well-mixed models. . .	48
3	Macroscopic and molecular rate constants for styrene at 75 °C and 0% conversion for a particle diameter of 100 nm.	66
4	Recipe information for miniemulsion polymerizations.	74
5	Macroscopic rate constants for butyl acrylate at 70 °C, taken primarily from Nikitin et al. [79]	90
6	Initial conditions for rate-equation model [79].	91
7	Molecular rate constants for butyl acrylate at 70 °C and a system radius of 100 nm, calculated from macroscopic values taken primarily from Nikitin et al. [79]	113

LIST OF FIGURES

1	Stochastic modeling provides a way to improve existing theories in free-radical polymerization kinetics.	2
2	Stochastic models provide a higher resolution of detail than is achievable with deterministic models but are also more computationally intensive.	3
3	Comparison of macroemulsion and miniemulsion polymerization systems [105]. In both systems, monomer droplets are stabilized by a surfactant, but miniemulsion polymerization also employs a costabilizer, contained within the monomer droplets, to prevent droplet decay.	11
4	Possible particle nucleation mechanisms in miniemulsion polymerization based on the zero-one assumption, including (a) nucleation with a water-soluble initiator radical, (b) nucleation with oil-soluble initiator where the initiator in the particle is dominant and desorption is required, and (c) nucleation with oil-soluble initiator where the small amount of initiator partitioned in the aqueous phase is dominant. Filled circles represent radicals, x's represent initiator end-groups, and a pair of x's represents an oil-soluble initiator molecule.	13
5	Chemical structure of styrene.	15
6	Chemical structure of 2,2'-azobis(isobutyronitrile).	15
7	Chemical structure of potassium persulfate.	17
8	Chemical structure of butyl acrylate.	24
9	Chemical structure of 2,2'-azo(2,4-dimethylvaleronitrile).	27
10	Example of a particle from the spatially-resolved model, where the blue lattice sites represent monomers, the yellow lattice sites represent mers bonded in polymer chains, the turquoise lattice sites represent undissociated oil-soluble initiator molecules, and the red sites represent radicals.	30
11	Two-dimensional representation of the minimum bond angle between mers overlaid on the carbon backbone of a polymer chain, with the bonded mers shown in checkerboard red, the radical shown in diagonal green, and the bonds between mers represented by dashed lines. This figure also depicts a backbiting event according to the traditional definition of backbiting, a topic which will be addressed later in this chapter.	33

12	Two-dimensional representation of a chain on the FCC lattice, illustrating (a) bond fluctuation and (b) reptation, with monomers in solid blue, bonded mers in checkerboard red, and radicals in diagonal green.	34
13	Diffusivity vs. oligomer length, up to a length of 10 mers, using bond fluctuation only (triangle) and reptation only (circle), compared with Griffith's scaling law (line) [51].	36
14	End-to-end distance of polymer chains vs. chain length, with a power-law exponent of 0.6 representing good solvents (dotted line), an exponent of 0.5 representing theta solvents (dash-dot line), and simulation data from the spatially-resolved model (diamond) fit with a power-law equation (solid line), giving an exponent of 0.53.	42
15	Cumulative distribution function of backbiting rate constant, obtained from the KMC lattice simulations using chains of length 10 to 2000 mers (solid line), and calculated using the scaling $1/(L_{bb} + 1)^2$ (dashed line) [121].	43
16	Three possible mechanisms for the formation of branches: (a) intermolecular chain transfer to polymer, (b) backbiting to produce a short-chain branch, and (c) backbiting to produce a long-chain branch. L_{back} is the backbone length, L_{cut} is the branch cutoff length, and L_{bb} is the backbiting distance.	51
17	Two possible structures resulting from formation of a branch point via backbiting, where after branching a radical may (a) propagate for a length greater than L_{cut} or (b) react in a branch-stopping event before it propagates to a length of L_{cut}	62
18	Possible chain-stopping mechanisms: (i) simple termination, (ii) termination by initiator dissociation, (iii) chain transfer to monomer, and (iv) termination by absorption.	71
19	Experimental conversion vs. time for miniemulsions of styrene and AIBN both with (diamond) and without (square) NaNO_2 at 50 °C and for miniemulsions of butyl acrylate and KPS both with (circle) and without (triangle) NaNO_2 at 40 °C.	75
20	Normalized density of molecular weight distribution from KMC simulations, for a particle diameter of 109 nm at 50 °C and 30% particle conversion, using $k_{t,m} = 158 \text{ s}^{-1}$, $f = 0.6$, and desorption rates of $2.0k_{p,m}N_{m,0}$ (triangle)(dashed line); $3.5k_{p,m}N_{m,0}$ (diamond) (dash-dot line); $5.0k_{p,m}N_{m,0}$ (circle)(dotted line), compared to normalized density of experiment (A) at final conversion of 92%.	77

21	Conversion vs. time from KMC simulations, for a particle diameter of 109 nm at 50 °C, using $k_{t,m} = 158 \text{ s}^{-1}$, $f = 0.6$, and desorption rates of $2.0k_{p,m}N_{m,0}$ (triangle); $3.5k_{p,m}N_{m,0}$ (diamond); $5.0k_{p,m}N_{m,0}$ (circle), with the new data from experiment (A) (square).	80
22	Normalized density of molecular weight distributions from KMC simulations using styrene at 75 °C, at 19% particle conversion and various particle sizes, with zero desorption, $k_p = 5.65 \times 10^2 \text{ L/mol/s}$, $k_t = 4.21 \times 10^7 \text{ L/mol/s}$, $k_d = 9.24 \times 10^{-5} \text{ s}^{-1}$, $f = 0.4$. Particle diameters of 100 nm (triangle)(dashed line); 170 nm (diamond)(dash-dot line); 240 nm (circle)(dotted line).	81
23	Normalized density of molecular weight distributions from KMC simulations using styrene at 75 °C, at 30% particle conversion and a particle diameter of 170 nm, with $k_{t,m} = 54.3 \text{ s}^{-1}$ and initiator efficiencies of 0.45 (triangle)(dashed line); 0.6 (diamond)(dash-dot line); 0.75 (circle)(dotted line), with Asua's molecular weight distribution [6] at 30% conversion (square).	82
24	Conversion vs. time from KMC simulations using styrene at 75 °C and a particle diameter of 170 nm, with $k_{t,m} = 54.3 \text{ s}^{-1}$ and initiator efficiencies of 0.45 (triangle); 0.6 (diamond) ; 0.75 (circle), with Asua's conversion vs. time data [6] (square).	82
25	Normalized density of molecular weight distributions from KMC simulations using styrene at 75 °C, at 30% particle conversion and a particle diameter of 170 nm, with $k_{t,m} = 54.3 \text{ s}^{-1}$, $f = 0.6$, and desorption rates of 0.0 (triangle)(dashed line); $0.05k_{p,m}N_{m,0}$ (diamond)(dash-dot line); $3.0k_{p,m}N_{m,0}$ (circle)(dotted line), with Asua's molecular weight distribution data [6] at 30% conversion (square).	85
26	Conversion vs. time from KMC simulations using styrene at 75 °C and a particle diameter of 170 nm, with $k_{t,m} = 54.3 \text{ s}^{-1}$, $f = 0.6$, and desorption rates of 0.0 (triangle); $0.05k_{p,m}N_{m,0}$ (diamond); $3.0k_{p,m}N_{m,0}$ (circle), with Asua's conversion vs. time data [6] (square).	86
27	Monomer conversion from rate-equation simulation compared to the experimental data from Nikitin et al. (+) [79].	94
28	Number-average molecular weight from rate-equation simulation (line) and steady-state model of Nikitin et al. (circle) [79] compared to experimental data point from Nikitin et al. (+).	94
29	Degree of branching from rate-equation simulation (line) and steady-state model of Nikitin et al. (circle) [79] compared to experimental data point from Nikitin et al. (+).	95

30	Concentration of branches produced by (a) backbiting and (b) intermolecular chain transfer to polymer, including branches produced by termination of mid-chain radicals.	97
31	Concentration of (a) short-chain and (b) long-chain branches at $L_{cut} = 10$ (solid line), $L_{cut} = 25$ (dashed line), and $L_{cut} = 40$ (dotted line), including branches produced by termination of mid-chain radicals. . .	98
32	Concentration of polymer repeat units predicted by rate-equation model (solid line) compared to critical concentration c^* (dashed line) necessary for polymer coil overlap, calculated from Equation (55).	101
33	(a) Long-chain branch concentration at $L_{cut} = 10$ both with (solid line) and without (dashed line) backbiting as a branch-stopping event; (b) $z_{p/bb}$, the number of propagation events per backbiting event, calculated from Equation (56).	102
34	(a) Long-chain branch concentration at $L_{cut} = 25$ both with (solid line) and without (dashed line) backbiting as a branch-stopping event; (b) $z_{p/bb}$, the number of propagation events per backbiting event, calculated from Equation (56).	103
35	(a) Long-chain branch concentration at $L_{cut} = 40$ both with (solid line) and without (dashed line) backbiting as a branch-stopping event; (b) $z_{p/bb}$, the number of propagation events per backbiting event, calculated from Equation (56).	104
36	Concentration of short-chain branches vs. concentration of backbiting events, using cutoff lengths of 9 mers (dashed line), 24 mers (dash-dot line), and 39 mers (dotted line). The solid line has a slope of one, which is the limit where all backbiting events produce a short-chain branch.	106
37	Intrinsic viscosity predicted from rate-equation simulation at (a) $L_{cut} = 10$ and (b) $L_{cut} = 25$, showing $[\eta_l]$ (dashed line), $[\eta_b]$ (solid line), and $[\eta_{corr}]$ (dotted line).	108
38	Intrinsic viscosity predicted from rate-equation simulation at $L_{cut} = 40$, showing $[\eta_l]$ (dashed line), $[\eta_b]$ (solid line), and $[\eta_{corr}]$ (dotted line).	109
39	Monomer conversion from KMC simulations with system radii of 100 nm (triangle) and 200 nm (diamond) compared to rate-equation simulation (solid line) and experimental data from Nikitin et al. (+) [79].	116
40	Number-average molecular weight from KMC simulations with system radii of 100 nm (triangle) and 200 nm (diamond) compared to rate-equation simulation (solid line), results from the model of Nikitin et al. (circle) [79] and experimental data point from Nikitin et al. (+).	118

41	Possible chain-stopping events considered for butyl acrylate solution polymerization, including (a) chain transfer to solvent, (b) termination by combination, and (c) intermolecular chain transfer to polymer. . .	119
42	Degree of branching from rate-equation model (solid line) and KMC simulations for system radii of 100 nm (triangle) and 200 nm (diamond) compared to the results from the model of Nikitin et al. (circle) [79] and the experimental data point from Nikitin et al. (+).	122
43	Concentration of branches produced by (a) backbiting and (b) intermolecular chain transfer to polymer, including branches produced by termination of mid-chain radicals, from rate-equation model (solid line) and KMC simulations for system radii of 100 nm (triangle) and 200 nm (diamond).	123
44	Concentration of polymer repeat units predicted by rate-equation model (solid line) and KMC simulations for system radii of 100 nm (triangle) and 200 nm (diamond), compared to critical concentration c^* calculated from Equation (55) for rate-equation model (dashed line) and KMC simulations for system radii of 100 nm (dash-dot line) and 200 nm (dotted line).	124
45	Concentration of short-chain branches at $L_{cut} = 10$, including branches produced by termination of mid-chain radicals, from rate-equation model (solid line) and KMC simulations for system radii of 100 nm (triangle) and 200 nm (diamond).	125
46	Concentration of short-chain branches at $L_{cut} = 25$, including branches produced by termination of mid-chain radicals, from rate-equation model (solid line) and KMC simulations for system radii of 100 nm (triangle) and 200 nm (diamond).	126
47	Concentration of short-chain branches at $L_{cut} = 40$, including branches produced by termination of mid-chain radicals, from rate-equation model (solid line) and KMC simulations for system radii of 100 nm (triangle) and 200 nm (diamond).	126
48	(a) Long-chain branch concentrations at $L_{cut} = 10$, from KMC simulations for system radii of 100 nm (triangle) and 200 nm (diamond) and from rate-equation model, determined both with (solid line) and without (dashed line) backbiting as a branch-stopping event; (b) $z_{p/bb}$, the number of propagation events per backbiting event, calculated from Equation (56).	127

49	(a) Long-chain branch concentrations at $L_{cut} = 25$, from KMC simulations for system radii of 100 nm (triangle) and 200 nm (diamond) and from rate-equation model, determined both with (solid line) and without (dashed line) backbiting as a branch-stopping event; (b) $z_{p/bb}$, the number of propagation events per backbiting event, calculated from Equation (56).	128
50	(a) Long-chain branch concentrations at $L_{cut} = 40$, from KMC simulations for system radii of 100 nm (triangle) and 200 nm (diamond) and from rate-equation model, determined both with (solid line) and without (dashed line) backbiting as a branch-stopping event; (b) $z_{p/bb}$, the number of propagation events per backbiting event, calculated from Equation (56).	129
51	Intrinsic viscosity predicted from simulations at (a) $L_{cut} = 10$ and (b) $L_{cut} = 25$, showing predictions of rate-equation model as $[\eta_l]$ (dashed line), $[\eta_b]$ (solid line), and $[\eta_{corr}]$ (dotted line); predictions of 100-nm radius KMC simulations as $[\eta_l]$ (filled triangle), $[\eta_b]$ (filled circle), and $[\eta_{corr}]$ (filled diamond); and predictions of 200-nm radius KMC simulations as $[\eta_l]$ (open triangle), $[\eta_b]$ (open circle), and $[\eta_{corr}]$ (open diamond).	131
52	Intrinsic viscosity predicted from simulations at $L_{cut} = 40$, showing predictions of rate-equation model as $[\eta_l]$ (dashed line), $[\eta_b]$ (solid line), and $[\eta_{corr}]$ (dotted line); predictions of 100-nm radius KMC simulations as $[\eta_l]$ (filled triangle), $[\eta_b]$ (filled circle), and $[\eta_{corr}]$ (filled diamond); and predictions of 200-nm radius KMC simulations as $[\eta_l]$ (open triangle), $[\eta_b]$ (open circle), and $[\eta_{corr}]$ (open diamond).	132
53	Linear-chain intrinsic viscosity from KMC simulations using system radii of 100 nm (filled triangle) and 200 nm (open triangle) compared to intrinsic viscosity obtained from rate-equation model with molecular weight scaled by the polydispersity from 200-nm radius KMC simulations.	132
54	Polydispersity index obtained from KMC simulations using system radius of 200 nm (circle) and corresponding linear fit, $3.2 \times 10^{-4}t + 1.90$ with $R^2 = 0.997$	133
55	Possible core-shell particle structures using monomers of types A and B (a) with separate polymer chains in the core and shell and (b) using a combination of surface-active initiator and RAFT agent to grow triblock copolymer chains through three layers, followed by annealing.	138

SUMMARY

Polymer chain microstructure, including characteristics such as molecular weight and branch length, can impact the end-use properties of the polymer. The assumptions contained in deterministic models prevent examination of the structure of individual polymer chains, so removal of these assumptions is necessary to gain insight into molecular-level mechanisms that determine chain microstructure. The work presented here uses a combination of stochastic and deterministic models to examine two significant mechanistic issues in free radical polymerization.

The zero-one assumption concerning the number of radicals is often made for miniemulsion polymerization using oil-soluble initiators because of accelerated termination due to radical confinement. Although most of the initiator is present inside the particles, opposing viewpoints exist as to whether the locus of radical generation is the particle phase or the aqueous phase. A well-mixed kinetic Monte Carlo (KMC) model is used to simulate the molecular weight distribution and the results are compared to estimated molecular weights for several chain-stopping events, with the finding that the dominant nucleation mechanism varies with reaction temperature and particle size.

Intramolecular chain transfer to polymer, or backbiting, is often assumed to produce only short-chain branches. Using a lattice KMC model, a cumulative distribution function (CDF) is obtained for branch lengths produced by backbiting. Implementation of the CDF in both a rate-equation model and the well-mixed KMC model shows that, for the butyl acrylate solution polymerization system used for comparison, backbiting is responsible for most of the branches, including long-chain branches, even though overlap of the polymer coils in the solution is predicted, a condition

which would normally be expected to lead to significant intermolecular chain transfer to polymer. The well-mixed KMC model provides a more thorough analysis of chain microstructure while the rate-equation model is more computationally efficient.

CHAPTER I

INTRODUCTION

Free-radical polymerizations represent the largest segment of commercial polymer production. One of the earliest examples is the production of styrene–butadiene synthetic rubber, which is produced via emulsion polymerization. Extensive research efforts undertaken to examine this system by researchers such as Smith and Ewart [108] led to the earliest classical theories concerning the intervals of emulsion polymerization [112]. Carothers was one of the earliest authors to consider the implications of multifunctional monomers, applying these concepts to predict the limiting conversions in condensation polymerizations according to monomer functionality [33]. The branching coefficient derived by Flory [45] represented a significant leap in the understanding of polymer networks, allowing prediction of the gel point for condensation polymerizations of multifunctional monomers based on the ratio of the two species in the reaction mixture. Stockmayer extended Flory’s ideas to calculate the molecular weight distribution of branched polymers [111] and along with Zimm [126] developed a method for estimating the radii of gyration of branched polymers. At that stage, the theories surrounding branched polymers had extended far beyond the experimental techniques of the time, so further development of the theory was limited until better measurements of molecular weight and intrinsic viscosity became available.

Advancement in the technology of free-radical polymerization has been driven by the desire for improved product quality through finer control of the polymerization, requiring improvements in experimental techniques as well as theory. The technologies and theories of free-radical polymerization are now at a crossroads. Miniemulsion polymerization allows tight control of the particle-size distribution, essential in

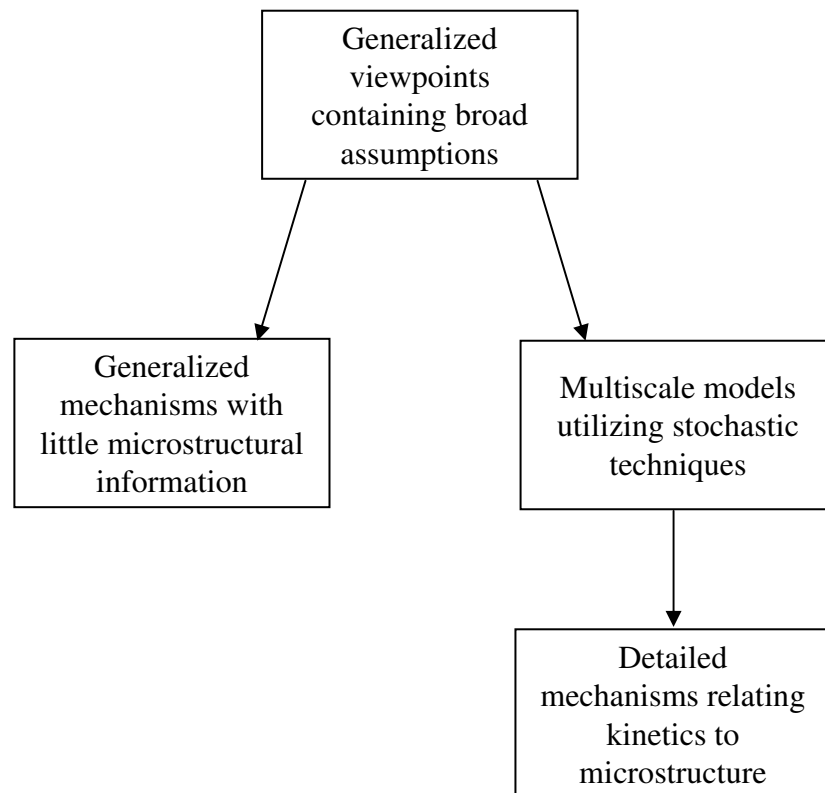


Figure 1: Stochastic modeling provides a way to improve existing theories in free-radical polymerization kinetics.

applications including the encapsulation of pharmaceuticals for controlled release. Controlled-radical polymerizations have enabled the production of polymer with uniform molecular weight and the design of polymer molecules with detailed architectures, such as block copolymers of uniform segment length. The degree of detail achievable in these processes requires further revision of the theories describing such processes. The systems which must now be considered consist of individual miniemulsion particles, which range in diameter from 50 – 200 nm, or even individual polymer chains. Continuum models alone are generally incapable of describing systems where the number of polymer chains or monomers becomes countable. Refinement of the existing theories for these nanoscale systems requires different modeling approaches, as shown in Figure 1.

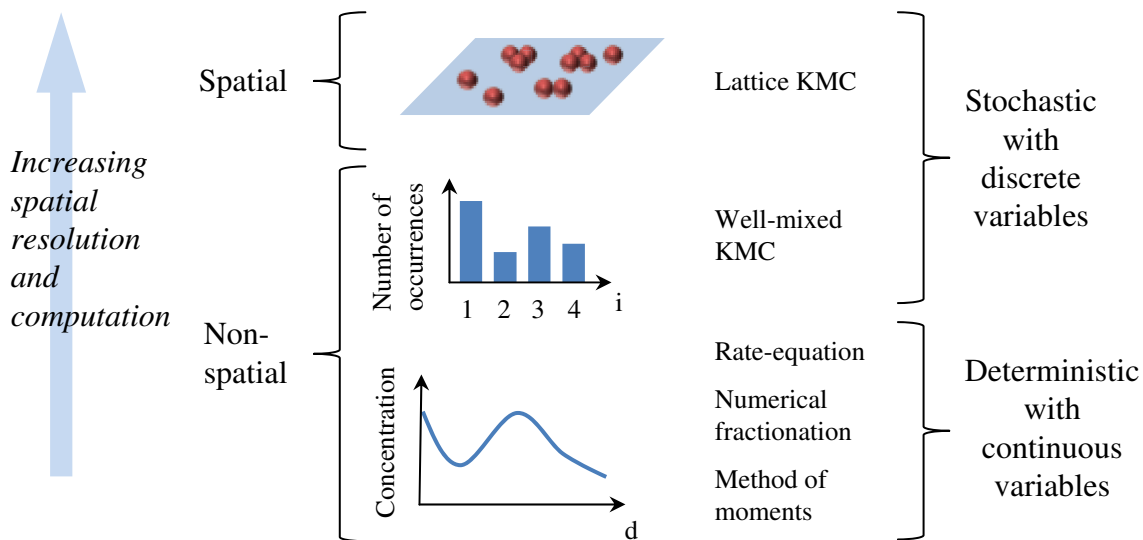


Figure 2: Stochastic models provide a higher resolution of detail than is achievable with deterministic models but are also more computationally intensive.

The kinetic Monte Carlo (KMC) algorithm provides an ideal framework for examining the growth of individual polymer molecules and their resulting topologies, as compared to deterministic models that only calculate macroscopic observables such as concentrations, an aspect illustrated in Figure 2. The KMC methodology has been applied to study the importance of chain-length-dependent termination

in controlled-radical polymerizations using reversible addition–fragmentation chain transfer (RAFT) [94] and to examine the influence of mid-chain radicals on the molecular weight distribution in the semicontinuous emulsion polymerization of butyl acrylate [9], among other things. Long-chain branching in vinyl acetate has been investigated using Monte Carlo techniques to sample chains from molecular weight and branching-density distributions [116]. Simulation of single reactions, such as propagation, chain transfer to monomer, and termination for individual radicals provides a detailed record of the events which lead to the final topology and molecular weight of a chain. The ability to investigate the specific mechanisms leading to any feature in the chain structure provides nearly boundless opportunities to improve the knowledge of a given reaction or set of reactions and how these reactions contribute to the chain topology. Computational capacity, availability of experimental data for key model parameters, and the degree of detail attained by current experimental techniques, however, all remain limitations to the modeling of chain microstructure.

1.1 Scope

This thesis provides some clarification on two significant issues in free-radical polymerization through the use of combined stochastic and continuum modeling techniques to unmask the central mechanisms governing chain microstructure, which are typically hidden behind overarching assumptions. The first issue considered is the dominant locus of radical generation for particle nucleation using oil-soluble initiators. Asua has posed that the radicals generated in the particle are dominant [13], while Nomura has theorized that the small fraction of radicals generated in the aqueous phase around a particle are dominant [81]. Both of these ideas are centered around the zero–one assumption, which suggests that multiple radicals cannot exist inside a particle for a duration sufficient for chain growth, due to the high rate of termination expected from

radical confinement inside miniemulsion particles. By simulating the kinetics of individual radicals, including radical absorption and desorption, the zero–one assumption is removed and replaced with a set of less severe assumptions about the individual reactions. As particle nucleation occurs quickly in miniemulsion polymerizations, the earlier stages of the polymerization at low conversion are most significant in the examination of this phenomenon; therefore, the simulations performed concerning this issue ignore the gel effect, whereby the termination rate decreases at higher conversion due to impaired mobility of radicals. Also, chain-length–dependent termination, which accounts for the differing diffusivities of radical-containing chains of varied length, is excluded from these simulations. These simplifications of the termination reaction draw from the assumption that the miniemulsion particle is well-mixed, such that the concentration of polymer chains throughout the particle is uniform. Justification of this assumption is provided later, based on the small size of miniemulsion particles relative to the diffusivity of a polymer chain. Radical absorption and desorption are other events that involve a number of assumptions. Radical-containing chains at or beyond a certain critical length are assumed to enter the particle instantaneously once they reach that length, and only unitary radicals or chains below the critical length are allowed to desorb from the particle [40]. Monomer concentration in the aqueous phase is assumed to remain constant throughout the polymerization, and propagation is the only aqueous-phase reaction considered in the simulations. These assumptions regarding radical absorption may have a small effect on the molecular weight for certain chain-stopping events but are unlikely to change the conclusions regarding the most significant chain-stopping events.

The second significant issue considered in this work is the branch-length distribution of polymers in which intramolecular chain transfer of radicals may occur. The term “backbiting” commonly refers to intramolecular chain transfer to a mer twice-separated from the radical [77]. Intermolecular chain transfer, between polymer

chains, is thought to be responsible for producing long-chain branches, and backbiting is assumed to only produce short-chain branches [48, 62, 77]. Unraveling the assumption that backbiting produces only short-chain branches requires investigation into the locations where a radical may come in contact with other mers in its own chain. For the work presented herein, this investigation is accomplished using spatially-resolved simulations of a chain on a face-centered cubic (FCC) lattice, where the lattice sites represent individual monomers or bonded mers, and bond length and bond angle constraints are enforced between mers. Each time the radical chain-end comes in contact with another mer in its chain, the distance in mers from the radical recorded, eventually producing a probability distribution based on the distance from the radical. In generating this probability distribution, the simulations are assumed to provide reasonable chain conformations and to sufficiently explore the range of all possible conformations. Physical reasonableness of the chain conformations on the lattice is shown through calculation of the end-to-end distance and its power-law scaling with chain length. The probability distribution is incorporated into both rate-equation and KMC models investigating the branch-length distribution in butyl acrylate solution polymerization. Exactly what number of mers constitutes a long-chain or short-chain branch is not well articulated. The rate-equation and KMC simulations use a series of cutoff lengths to differentiate between short-chain and long-chain branches, but more broadly this study highlights the need to better understand and quantify the relationship between chain topology and viscosity.

1.2 Summary

Chapter 2 provides a review of relevant literature regarding the systems examined in this work and the modeling techniques used in the literature to study these systems. Miniemulsion polymerization is discussed, and a detailed description is given of the issues surrounding particle nucleation with oil-soluble initiators. Past experimental

studies and modeling efforts pertaining to branching in butyl acrylate are discussed, as well as the experimental system that is the basis for the branching studies presented here [79]. An overview is presented for spatial modeling techniques used for polymer chains, and the topics of bond fluctuation and reptation are discussed, as these methodologies for simulating polymer diffusion are applied in the spatially-resolved lattice model.

Chapter 3 describes the spatially-resolved model developed to study miniemulsion polymer particles with concurrent simulation of reactions and diffusion of polymer chains. An account is given of the efforts to model center-of-mass motion of polymer chains using both bond fluctuation and reptation. The implementation of reactions within the FCC lattice is described, with details provided for reactions such as propagation and termination. The development and justification of the backbiting cumulative distribution function (CDF) are also provided in this chapter.

Chapter 4 provides a thorough description of the well-mixed models used in the simulation studies. The well-mixed KMC model is discussed, and a detailed list of corresponding macroscopic and molecular rate equations is given. Discussion is provided for all of the reactions, including the conversion of macroscopic rate constants to the molecular scale. The rate-equation model is presented, with particular attention given to the ordinary differential equations used to model the concentration of short-chain and long-chain branches. The methods used to predict the linear and branched intrinsic viscosities are described.

In Chapter 5, the results are presented for the study of the nucleation mechanisms using oil-soluble initiators in the miniemulsion polymerization of styrene. The four chain-stopping mechanisms considered in the study are described, and the resulting molecular weight is predicted for each chain-stopping event. Two sets of experimental data for styrene miniemulsion polymerization are examined: one new set of data taken at 50 °C with a particle diameter of 109 nm [99], and another set of data from the

literature taken at 75 °C with a particle diameter of 170 nm [6]. Agreement is achieved between KMC simulations and each set of experimental data. Desorption of radicals is found to be significant for the newer data set, with a lower temperature and smaller particle size, while termination by combination is shown to dominate the molecular weight distribution when both the temperature and particle size are increased.

The simulation results from the rate-equation model compared to experimental data for butyl acrylate solution polymerization [79] are presented in Chapter 6. The nominal rate constants are shown to produce good agreement with the experimental data [79] for monomer conversion, number-average molecular weight, and degree of branching. Backbiting is found to be responsible for producing the majority of branches, including most long-chain branches, contradicting the common assumption that backbiting only produces short-chain branches. The dominance of backbiting is especially significant since the polymer coils in solution are predicted to overlap, a condition which would often be assumed to result in a noticeable amount of intermolecular chain transfer to polymer. A majority of the branches, about 92%, are expected to be less than 10 mers in length. The predicted long-chain branched intrinsic viscosity grows closer to the linear-chain intrinsic viscosity as the cutoff length for long-chain branches is increased. The total branched viscosity, accounting for both long-chain and short-chain branching, is found to be insensitive to the cutoff length between long-chain and short-chain branches.

Chapter 7 presents the results from the well-mixed KMC simulations of butyl acrylate solution polymerization, comparing these results to both the experimental data [79] and the results of the rate-equation simulations. The necessary requirement of a finite system size in the KMC simulations results in an artificial confinement of radicals, increasing the termination rate when two radicals are confined within the system, and reducing both the rate of conversion and the amount of branching as the radical lifetime is shortened. As the system boundary is only artificial, absorption and

desorption of radicals through the system boundary are not allowed, so the generation of geminate radicals from each initiator dissociation dictates that either zero or two radicals are present at any time. A noticeable difference exists between the two models in the predicted amounts of long-chain branching, but this difference diminishes as the cutoff length separating short-chain and long-chain branches is increased. The lack of information concerning branching topology in the rate-equation model results in a higher amount of long-chain branching, while the explicit counting of long-chain branches in the KMC simulation causes the amount of long-chain branching to plateau at a lower value.

CHAPTER II

LITERATURE REVIEW

2.1 Polymerization Systems

2.1.1 Solution Polymerization

This examination of free-radical polymerization kinetics encompasses several different polymerization systems. The simplest of these systems is solution polymerization, where monomer is diluted with an organic solvent. As compared to bulk polymerizations, the use of a solvent allows for better temperature control through improved heat transfer, an important characteristic as most free-radical polymerizations are highly exothermic [105]. The low monomer concentration not only makes the mixture less viscous but also results in a slow rate of polymerization [105]. A significant downside to solution polymerization is the potential environmental impact of many organic solvents, which may increase the cost through additional separation processes to recycle the solvent [105]. Another potential issue is contamination of the polymer if removal of the solvent is difficult [82]. One of the major commercial uses of solution polymerization is in the production of polystyrene, for applications such as expandable polystyrene and injection molding to produce items ranging from household products to medical lab equipment [82]. Polyacrylonitrile, the primary component of most acrylic fibers, is another important commercial polymer that is often produced by solution polymerization [82].

2.1.2 Emulsion Polymerization

In conventional emulsion polymerizations, referred to here as macroemulsions, a surfactant is used to stabilize monomer droplets dispersed in water. Macroemulsion polymerization has several advantages over solution polymerization. First, the use

of water, rather than an organic solvent, greatly reduces the environmental impact as compared to solution polymerization, and the high thermal conductivity of water makes removal of heat even easier. Second, the high concentration of monomer inside droplets significantly increases the rate of polymerization over that achievable in solution polymerization [105]. As with solution polymerization, the viscosity of emulsions remains low throughout the polymerization, making the mixture easier to pump and improving heat transfer [105]. One of the largest commercial applications of macroemulsion polymerization is in the production of styrene–butadiene synthetic rubber used in tires [82]. Poly(vinyl acetate) is normally produced via macroemulsion polymerization for use in applications such as adhesives and paints [82].

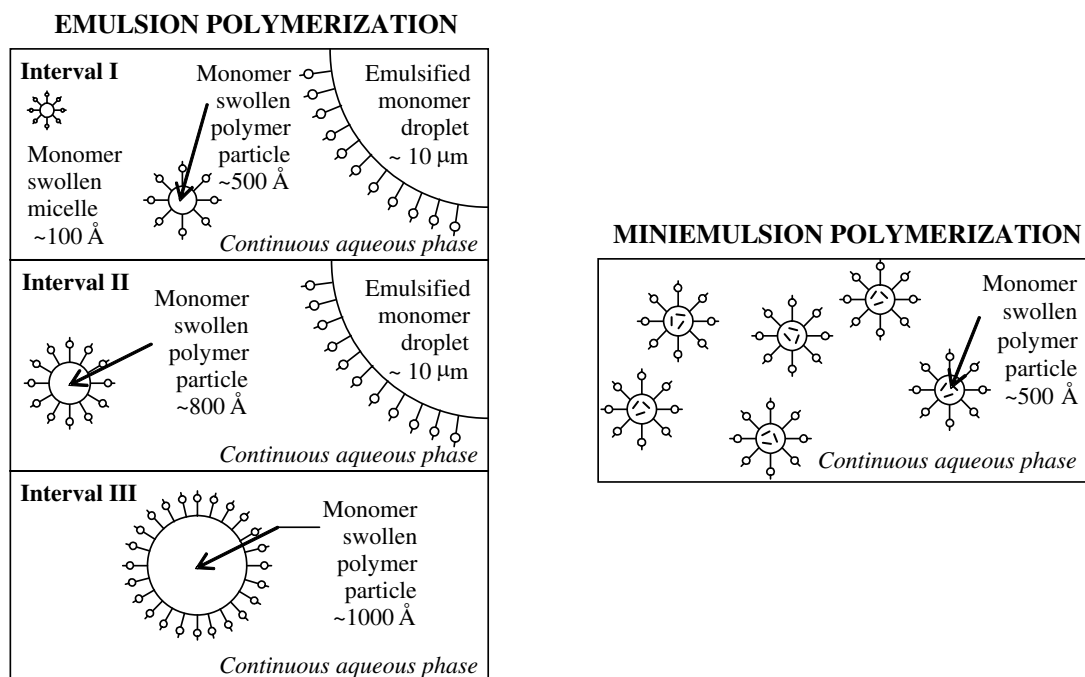


Figure 3: Comparison of macroemulsion and miniemulsion polymerization systems [105]. In both systems, monomer droplets are stabilized by a surfactant, but miniemulsion polymerization also employs a costabilizer, contained within the monomer droplets, to prevent droplet decay.

An unseeded, batch macroemulsion polymerization reaction may be divided into three intervals, as shown in Figure 3. Particle nucleation occurs during Interval I as

radicals generated in the aqueous phase propagate and then either enter monomer-swollen micelles or precipitate from the aqueous phase and nucleate new particles. Interval I is usually completed within 2 – 10% monomer conversion, with most of the monomer remaining in the droplets [105]. During Interval II, polymerization occurs in the monomer-swollen particles, while the monomer concentration within the particles remains constant due to diffusion of monomer from droplets. When the monomer droplets have disappeared, Interval III commences, and during this interval the reaction continues until the monomer in the particles is depleted.

2.1.3 Miniemulsion Polymerization

Unpredictable particle nucleation in macroemulsions, along with the swelling of particles during Interval II, complicates control of the final particle size. Miniemulsion polymerizations overcome these issues by employing a costabilizer in addition to the surfactant, preserving the particle size from the initial dispersion by preventing decay of the monomer droplets [105]. The droplets produced in miniemulsions are very small, on the order of 50 – 200 nm, so the surface area of the droplets is quite high. Diffusion of monomer from these small droplets into larger droplets is thermodynamically favorable due to the resulting decrease in interfacial free energy, leading to the decay of smaller droplets in macroemulsions. Costabilizers employed in miniemulsions are highly water-insoluble, compared to the monomer, and so remain inside the monomer droplets or nucleated particles, as shown in Figure 3. Loss of monomer from miniemulsion droplets increases the concentration of costabilizer in the droplets, resulting in a thermodynamically unfavorable increase in the free energy of mixing which balances the decrease in interfacial free energy [105]. Most of the surfactant is adsorbed to the droplet surfaces, rather than being free to form micelles or stabilize additional particles nucleated from the aqueous phase. Radical entry into monomer droplets, rather than micelles, is then the primary mechanism of particle nucleation

when water-soluble initiators are used [105]. Droplet nucleation was first reported by Ugelstad et al. [117], and since that time a number of important applications have been developed, including encapsulation of inorganic solids [41, 42, 43] and reversible addition–fragmentation chain-transfer (RAFT) polymerization in dispersed systems [29, 104]. Encapsulation of a substance in polymer is only achievable when droplet nucleation occurs, allowing polymerization in monomer surrounding the encapsulated substance, since micellar nucleation would result in diffusion of monomer away from the substance that is to be encapsulated. RAFT polymerization is only possible when RAFT agent is present at the locus of polymerization, the monomer droplets [11]. Neither of these applications are feasible for macroemulsion polymerization, where the locus of polymerization is in the micelles, and monomer must diffuse through the aqueous phase to the micelles. Because monomer does not need to diffuse through the aqueous phase in miniemulsion polymerization, water-insoluble monomers may also be used.

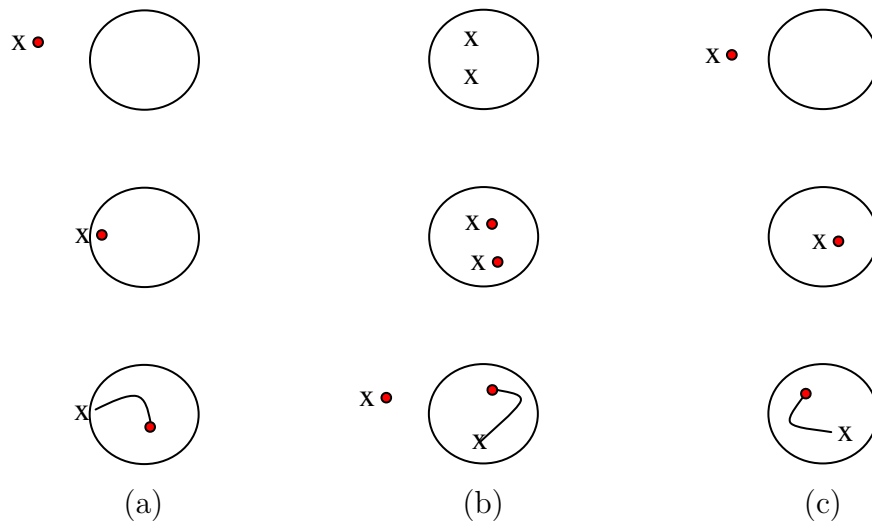


Figure 4: Possible particle nucleation mechanisms in miniemulsion polymerization based on the zero–one assumption, including (a) nucleation with a water-soluble initiator radical, (b) nucleation with oil-soluble initiator where the initiator in the particle is dominant and desorption is required, and (c) nucleation with oil-soluble initiator where the small amount of initiator partitioned in the aqueous phase is dominant. Filled circles represent radicals, x’s represent initiator end-groups, and a pair of x’s represents an oil-soluble initiator molecule.

While water-soluble initiators are more commonly used in miniemulsion polymerizations due to a higher rate of polymerization, the use of oil-soluble initiators has increased in recent years [11, 105]. Water-soluble initiators dissociate into radical pairs in the aqueous phase and single radicals then enter the particles, as shown in Figure 4(a). When attempting to achieve a uniform particle-size distribution, as is the case in miniemulsions, water-soluble initiators present the issue of secondary nucleation, whereby additional particles may be formed from radicals in the aqueous phase. Oil-soluble initiators circumvent this obstacle by generating radicals primarily within monomer droplets, significantly decreasing the probability for secondary nucleation. A second advantage of oil-soluble initiators is greater mobility of chain ends within the particle, as the hydrophilic end-groups from water-soluble initiators are thought to remain anchored to the particle surface [36, 65]. Greater mobility of the radicals allows for more complete polymerization of the particle interior, enabling the production of a uniform particle morphology. The slower rates of polymerization observed for oil-soluble initiators have been attributed to a significant fraction of radical pairs recombining within the particle immediately after dissociation. This “cage” effect may be due to the higher viscosity of the particle as compared to the aqueous phase. The fraction of initiator radicals that escape this “cage” after generation is commonly referred to as the initiator efficiency.

Even when two radicals are able to separate sufficiently within a miniemulsion particle, they are still confined to the small volume of the particle, increasing the probability of termination when two or more radicals are present inside a particle, as compared to bulk polymerizations. This confinement is thought by some authors to accelerate termination of the radicals, thereby making the existence of multiple radicals inside a particle unlikely. Therefore, the assumption is often made that either one or zero radicals are present inside a particle during the polymerization [105]. Under the zero–one assumption, termination of radicals inside the particle

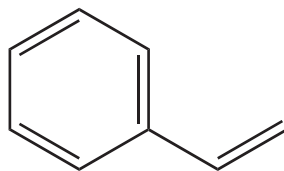


Figure 5: Chemical structure of styrene.

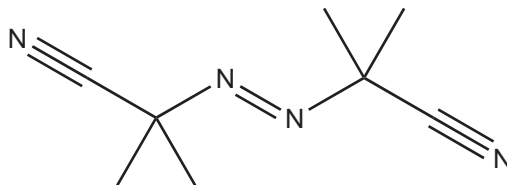


Figure 6: Chemical structure of 2,2'-azobis(isobutyronitrile).

is possible only when new radicals are introduced to the particle by such means as dissociation of oil-soluble initiator or absorption of radicals from the aqueous phase.

As oil-soluble initiators have gained a greater foothold in miniemulsion polymerization, a debate has grown concerning the primary locus of radical generation for particle nucleation. The zero-one assumption implies that the aqueous phase must be of some significance, since radicals are formed in pairs and thus should not be able to grow to a meaningful chain length without some mechanism for achieving a single radical within the particle. A small fraction of oil-soluble initiator is partitioned in the aqueous phase. Two primary schools of thought exist regarding this mechanism: one, made popular by Asua [13], poses that the locus of radical generation is within the particle, and that desorption of at least one radical must occur after initiator dissociation, as shown in Figure 4(b); the other, postulated by Nomura [81], suggests that termination of radical pairs inside a particle is so overwhelming that the locus of radical generation must be the aqueous phase, and that such radicals are subsequently absorbed into the particle, as shown in Figure 4(c).

For the desorption-dominated mechanism to be considered, radicals must first diffuse apart after generation before recombining or terminating. Radicals are unlikely to desorb from a particle after propagating several times due to a decrease in the

water-solubility of the radical, which is low from the beginning for an oil-soluble initiator radical. Asua suggests that chain transfer to monomer must occur to produce a significant number of monomeric radicals that would desorb from a particle [13]. Desorption from a particle with a diameter of 100 – 200 nm is then plausible, as the growing radicals are likely to encounter the particle surface numerous times due to their high diffusivity. In one of the early studies presenting his theory, Asua uses a population-balance model [13] to calculate the fraction of particles containing n radicals, where the maximum value of n is varied, so the zero–one assumption is not implied. Rates are calculated for radical desorption and absorption, where multiple redesorption and reabsorption steps may occur for a radical; both termination and radical generation occur in both phases. The desorption rate is calculated from the probabilities of absorption and redesorption, which are determined by the rates of propagation and termination in both phases. The absorption rate is determined by the diffusivity of the radicals in the aqueous phase and a “radical-capture efficiency.” To solve the population balance, the number of particles containing n radicals is assumed to be at steady state. As a test system for the model, Asua performs simulations for the seeded emulsion polymerization of styrene using 2,2'-azobis(isobutyronitrile) (AIBN) as the oil-soluble initiator at particle diameters of both 122 and 644 nm [13]. The structures of styrene and AIBN are shown in Figure 5 and 6. For the 122-nm particle diameter, >99% of the particles have zero or one radical, and \bar{n} is calculated to be approximately 0.5. For the 644-nm particle diameter, about 24% of the particles have two radicals, showing that zero–one kinetics are not dominant at this larger system size. This shift in the distribution of radicals seems to indicate that radicals survive longer in a larger particle due to decreased confinement effects, and provides evidence that desorption of radicals is substantially more significant at smaller particle sizes. Asua varies the concentration of initiator in the aqueous phase, with the model results showing that this variation has no effect on \bar{n} , and he therefore

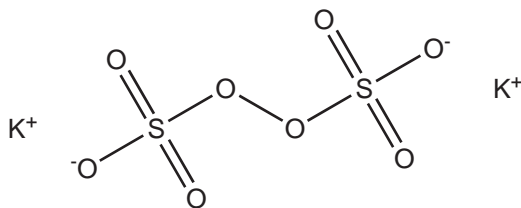


Figure 7: Chemical structure of potassium persulfate.

concludes that the locus of radical generation must be inside the particle [13].

The absorption-dominated mechanism, posed by Nomura, requires the assumption of instantaneous termination for radical pairs produced within the particle. Oil-soluble initiators such as AIBN are sufficiently soluble in water to produce a substantial number of radicals in the aqueous phase at reasonable reaction temperatures. These radicals then diffuse toward particles, where they are absorbed due to their greater solubility in the particles. Nomura investigates this absorption-dominated mechanism via microemulsion polymerization of styrene using both AIBN and the water-soluble initiator potassium persulfate (KPS) [81], the structure of which is shown in Figure 7. Microemulsion polymerization results when either the surfactant concentration is greatly increased or the monomer concentration is greatly decreased, as compared to a macroemulsion polymerization system, producing droplets of diameter 10 – 100 nm. Due to the difference in particle size between microemulsions and miniemulsions, a direct comparison of the particle nucleation mechanisms in microemulsions and miniemulsions is not possible. The microemulsion studies show that the rate of conversion increases with AIBN concentration, but the rate of conversion using the oil-soluble initiator is much lower than that achieved using KPS. For the microemulsions, the average molecular weight is not affected by changing the initiator concentration [81]. The findings for the conversion rate show that radical generation is the rate-limiting step in the polymerization using oil-soluble initiators, and that oil-soluble initiators exhibit lower efficiencies than water-soluble initiators. The high

molecular weights observed, $6 - 8 \times 10^6$ g/mol, are consistent with reduced termination due to the presence of only a single radical per particle. The independence of molecular weight from the rate of radical generation when using AIBN indicates that most of the oil-soluble initiator radicals are quickly terminated after generation, providing further evidence of zero-one kinetics in microemulsion polymerization. For the macroemulsion study, increasing the initiator concentration is found to increase particle nucleation at similar rates for both AIBN and KPS [81]. This shows that AIBN radicals are present in the aqueous phase and are capable of nucleating new particles from the existing micelles, since aqueous-phase radical generation is the only source of radicals in macroemulsion polymerization. In order for the absorption-dominated mechanism to be reasonable, however, almost all of the radicals generated in the aqueous phase must enter monomer-swollen micelles rather than nucleated particles, due to the relatively small number of AIBN radicals generated in the aqueous phase. Nomura concludes that the locus of radical generation for particle nucleation in microemulsions is the aqueous phase.

The differing results obtained by Asua and Nomura may be caused by the different systems they examined. In the seeded emulsion polymerizations modeled by Asua, the oil-soluble initiator would be more soluble in the seed particles, thus generating a large number of radicals in the particles. Asua's model shows that radical confinement inside smaller particles should have a significant role in the polymerization kinetics of oil-soluble initiators, but that increasing particle size lessens the effect of confinement. According to the results of Asua, both termination by combination and radical desorption may be relevant, depending on the system size. The experiments performed by Nomura for microemulsion polymerization further substantiate the idea of radical confinement, as the smaller size of these particles should accelerate termination between radical pairs generated inside a particle. In macroemulsion polymerization, the aqueous phase is essentially the only source of radicals, so absorption of radicals

should be the primary mechanism for nucleation, in this case micellar nucleation. The work presented in Chapter 5 provides some resolution between the conclusions of Asua and Nomura.

2.2 Spatial Modeling of Polymer Chains

To understand the development of the particle morphology in macroemulsions and miniemulsions, the motion of polymer chains must be simulated. Molecular dynamics simulations apply Newton's equations of motion to groups of atoms or molecules with interaction potentials, such as Lennard–Jones, specified for the atoms or molecules [7]. One such type of simulation used for polymers is the bead–spring model, which requires the excluded-volume constraint so that the monomers cannot overlap, includes an attractive potential between monomers, and allows bond length to vary [64]. Bead–spring models have been used to examine cases such as the glass transition of polymer melts [22], the interaction of polymer melts with nanoparticles [109], and polymer in good solvent [93]. Equilibration of polymer chains at theta conditions has been examined using a bead–spring model with a Link-Cell Monte Carlo method, which specifies the particular monomers which may interact with one another [73]. Further coarse-graining, to incorporate multiple monomers in a single bead, has been employed to examine systems including polymer melts confined between two surfaces [23] and to examine entanglements in polymer melts [95]. In addition to the bead–spring model, the rotational isomeric states (RIS) model is another coarse-grained model applying potential energies to simulate polymer chain conformations. The RIS model incorporates configurations for each pair of consecutive carbon–carbon bonds from all accessible regions of the potential energy surface obtained through exploration of the full range of torsional angles for the two bonds [47]. Such configurations as used in the RIS model may correspond to local minima of the potential energy

surface, but this is not a necessary condition [47]. RIS theory has been used for applications such as the investigation of chain packing and thermodynamic properties in polyethylene and polypropylene melts [106], the examination of the orientation of liquid crystals [1], and the prediction of stiffness of ionic polymers [122].

In spite of the reduction in computational time afforded from the coarse-graining of polymer chains, off-lattice molecular dynamics models are still better suited to studying chain equilibration or diffusion in systems with few polymer chains, due to the continuous spatial resolution. To simulate larger systems, such as entire macroemulsion or miniemulsion particles, spatial discretization, using some type of lattice, becomes necessary to reduce the computational time. RIS theory has been applied to coarse-grained simulations of polymer chains on a diamond lattice, where each site has 12 nearest-neighbors, but this requires knowledge of the torsional potential energies and tracking of the rotational state of each bond between backbone carbon atoms [37, 97, 98]. The method of bond fluctuation allows the motion of monomers or larger chain segments to be simulated on a lattice without any potential energy calculations, but this method does allow chains to obey Rouse dynamics [32], so that the motion of monomers or chain segments tends to be coordinated through modes of relaxation, bringing the chain conformation towards equilibrium [102]. Entanglements in polymer melts [107] and chain dynamics in good and theta solvents [103] have been studied using bond fluctuation lattice models. Recently, bond fluctuation has been used to examine the compressibility of dense polymer melts where the excluded-volume constraint is replaced by an overlap penalty [123].

The Rouse model provides a good description of polymer chain motion at dilute concentrations, but, as the concentration of polymer increases, chains become confined by neighboring chains, and the Brownian motions of individual monomers no longer bring the chain towards equilibrium, instead cascading along the length of the chain, bounded by the existing topology. This produces a serpentine movement of the chain

which shifts its center of mass, a mechanism commonly referred to as reptation [39]. This theory may be expanded to account for variation in the tube diameter as well as the interaction between tubes, and the longitudinal and transverse motions of the polymer may be separately considered [60]. Simulations on a simple cubic lattice using bond fluctuation reproduced the transition from Rouse dynamics to reptation, where the chain relaxation time ceases to be dependent on the radius of gyration [84]. The self-diffusion coefficients for polymers at the transition from Rouse to reptation behavior may be described as a function of the degree of entanglement between chains, based on the interaction between segments in a chain [53, 54]. Shorter chains tend to exhibit only Rouse behavior, but increasing the molecular weight beyond a critical value produces an increasing amount of reptation [53]. The predictions of this theory are in good agreement with experimental measurements of diffusivity and viscosity versus molecular weight [38, 101].

2.3 Key Aspects of Polymer Modeling

2.3.1 Molecular Weight Distribution

Models of free-radical polymerization kinetics generally are used to predict various characteristics of the polymer, such as the molecular weight distribution or the level of branching, and often to gain insight into the mechanisms which lead to these characteristics. Molecular weight distributions are often calculated using the method of moments [15] with assumed distribution functions such as the Schultz–Flory distribution, which allows for chain-stopping via chain transfer and termination by disproportionation only [75]. The method of moments has been applied to predict molecular weight distributions in systems such as the emulsion polymerization of vinyl acetate [49], the continuous polymerization of vinyl acetate in bulk or solution [56], and to examine the variation of polydispersity between bulk, mixed-continuous, and

segregated-continuous polymerizations of vinyl acetate [113]. For systems with significant branching, the resulting increase in polydispersity renders direct reconstruction of the distribution from moments less suitable [31]. Numerical fractionation, an extension of the method of moments, has been used for highly branched systems, separating chains into successive generations according to the level of branching [114]. Monte Carlo sampling techniques have also been applied to examine the molecular weight distribution in highly branched systems [57, 115]. Termination by combination in emulsion polymerization may be accounted for using discretized population-balance equations to account for live chains of different lengths within a particle [30, 31]. Particles may be singly distinguished, where any and all radicals are generated or absorbed at the same time, or doubly distinguished, where radicals are generated or absorbed at different times, resulting in live chains of differing length. This method divides the chain length domain into a series of bins, with the mid-point of each bin representing all chains in the bin, so a new chain resulting from termination by combination is split into bins above and below its length according to the distance from each mid-point [30, 31].

2.3.2 Particle Morphology

Past approaches to the modeling of miniemulsion particles required some level of the continuum assumption. Karlsson et al. [58] use an approach where the particles are divided into concentric shells, and the distribution of radicals is then modeled using a probability density function based on the time of entry and fractional penetration into the particle. Other concentration variables, however, require the continuum assumption within each shell. Similarly, Asua's model [13] uses the continuum assumption for the concentration variables, but includes an integer number of radicals. Due to the submicron size of miniemulsion particles, concentration variables are not adequate to describe the amounts of different species within a particle. Using a kinetic Monte

Carlo (KMC) approach to model a miniemulsion particle allows for the removal of continuum variables from the simulation. Prescott uses a KMC approach to simulate chain-length-dependent termination in free-radical polymerization using RAFT [94]. Luo and Yu apply the KMC methodology to study droplet nucleation in miniemulsion polymerization using RAFT [69].

Attempts have been made to model radial non-uniformities in emulsion particles. Krywko et al. [65] used an ordinary differential equation model with concentric shells, but this still required the assumption that each shell is well-mixed. For KPS initiator, they concluded that radial gradients exist in the radical concentration, and that most radicals remain near the particle surface [65]. Mills et al. [74] developed a model of partial differential equations and examined particle non-uniformities, finding that the extent of radical penetration largely determines the morphology. In spite of the improvements, both of these models still require the use of concentration variables, potentially introducing larger errors due to discontinuities.

Several decades ago, Chern and Poehlein [36] applied Monte Carlo techniques to study emulsion particles. This approach requires no continuum assumptions, allowing monomers to be individually projected onto a lattice grid, with events such as propagation or diffusion occurring between two adjacent lattice sites. The execution of events is determined through probabilistic sampling based on the relative rates of the various events. Instead of using a bulk propagation rate, for instance, a rate is determined for an individual radical to propagate to a single monomer. Observed rates of reaction inherently decrease as the concentration of polymer increases within the particle, since a radical will have, on average, fewer adjacent monomers with which to react. Chain motion likewise becomes more constrained as monomer conversion increases, reducing the observed diffusion rates. At the time of Chern and Poehlein's study, computational capacity limited both the size and scope of their study. Recent

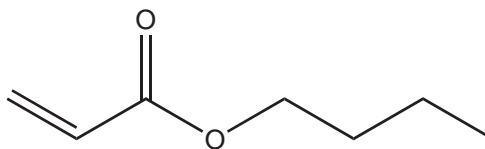


Figure 8: Chemical structure of butyl acrylate.

increases in both memory and processor speed allow full resolution of a miniemulsion particle, at length scales from the monomer radius of gyration up to the particle diameter.

2.3.3 Branching Models

The rate-equation models often used to study free-radical polymerization are not well-suited to capture molecular-level details, such as branch length and distance between branches, which may affect bulk properties like viscosity. To gain a more detailed understanding of the branching structure in polymers such as poly(butyl acrylate), for which the monomer structure is shown in Figure 8, a number of modeling approaches have been developed. The “numerical fractionation” model of Teymour and Campbell [114] divides the polymer into branching generations, where the zeroth generation is linear and the first generation has branches added to linear chains. Pladis and Kiparissides [88] extend this numerical fractionation model to include intermolecular chain transfer to polymer and terminal-double bond reactions, where the branching generations do not follow the geometric sequence resulting from termination by combination. They use this model to examine the joint molecular weight–long-chain branching distribution of polyethylene produced in a continuous stirred-tank reactor [88]. While Pladis and Kiparissides include backbiting, they assume that it only produces short-chain branches, and do not consider the effects of short-chain branching on the polymer properties.

Krallis and Kiparissides [62] employ the fixed-pivot technique to model the bivariate molecular weight–long-chain branching distribution, using population-balance

equations for both live and dead chains. In this algorithm, the domains of chain length and branching level are discretized using a two-dimensional grid, and the population-balance equations are solved at specific grid points. The bivariate molecular weight–long-chain branching distribution is calculated by Iedema et al. [56] by solving the population-balance equations for live and dead chains using the method of moments. They employ a version of numerical fractionation to the branches produced by terminal-double bond polymerization and then take the moments of the branching distribution, reducing the problem from 2-D to 1-D [56]. Kim and Iedema [61] include the effect of chain scission in their simulation of the long-chain branching distribution in low-density polyethylene. None of these authors consider short-chain branching, instead making the assumption that long-chain branching, readily quantifiable through intrinsic viscosity measurements, is dominant in determining the end-use properties of the polymer. These authors also assume that all long-chain branches are formed via intermolecular chain transfer to polymer or terminal-double bond polymerization [56, 61, 62].

2.4 Branching in Butyl Acrylate

In the free-radical polymerization of monosubstituted vinyl monomers, including butyl acrylate, chain transfer to polymer via hydrogen abstraction often leads to substantial levels of branching. The level of branching in the polymer may have a significant effect on its end-use properties. Plessis et al. [91] observed that the adhesive properties of a butyl acrylate–styrene copolymer vary with the level of branching. Branches formed by chain transfer to polymer increase the gel content, increasing both the resistance to shear and the tack, or tendency to flow, at gel fractions up to 32%. Rheological properties of poly(butyl acrylate) have been shown to change with the level of branching [5]. The number of entanglements in poly(butyl acrylate) increases with the level of branching, significantly increasing the loss modulus, or

dissipation of energy due to viscous flow, at higher rotational frequencies where the entanglements begin to break [4, 48].

^{13}C nuclear magnetic resonance (NMR) spectroscopy provides a way to measure the total branching content, independent of the mechanical properties of the polymer. Solution-state NMR [4, 48] and swollen-state NMR [90, 91] are techniques commonly used to measure branching content in alkyl acrylates. Liu et al. [67] examined polymer diffusion as a function of branch content in butyl methacrylate, measuring the amount of branching using solution-state NMR. Solution-state ^{13}C NMR has been used to characterize the structure of butyl acrylate chains formed in high-temperature solution polymerization [96]. Recently, Castignolles et al. [34] compared several different NMR techniques used to measure degree of branching and concluded that melt-state NMR is the most efficient method for alkyl acrylates. Long-chain branching may be examined qualitatively using intrinsic viscosity measurements but cannot currently be quantified experimentally for polyacrylates due to the small amount of long-chain branching present in these polymers and the competing effects of short-chain and long-chain branching on the rheological properties [34]. Castignolles et al. measured the intrinsic viscosity of a branched butyl acrylate polymer and compared the measured value to a calculated linear viscosity for a polymer of equivalent molecular weight. Based partly on the similarity between the branched and linear viscosities, they concluded that no long-chain branches were formed in their solution polymerization of butyl acrylate [34].

The branching characteristics of butyl acrylate polymerized in a seeded, semibatch emulsion have been studied by Plessis et al. [90], with one conclusion being the dominance of backbiting in the formation of branch points. In further work, Plessis et al. [89] added a chain transfer agent (CTA) to the butyl acrylate polymerization. They developed a numerical fractionation model which predicts that most of the branches should be short and formed by backbiting [89]. Former et al. [48] and

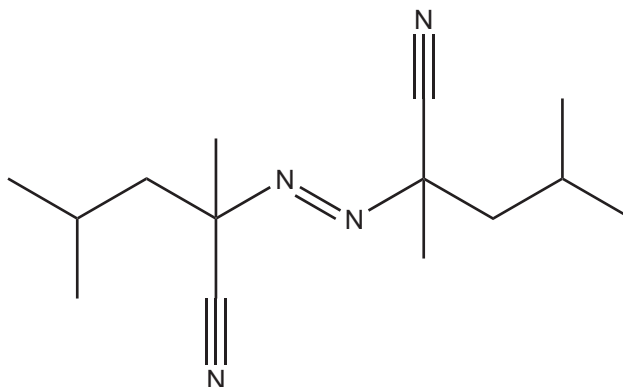


Figure 9: Chemical structure of 2,2'-azo(2,4-dimethylvaleronitrile).

Ahmad et al. [5] have used dynamic viscosity measurements to examine the effects of branching in butyl acrylate on its viscoelastic properties. The observations of Former et al. are consistent with significant short-chain branching and minimal long-chain branching [48].

Solution polymerization of butyl acrylate was performed by Nikitin et al. [79] using the oil-soluble initiator 2,2'-azo(2,4-dimethylvaleronitrile) (AVN), the structure of which is shown in Figure 9. Nikitin et al. derive steady-state equations using reaction-rate expressions to predict the impact of both inter- and intramolecular chain transfer to polymer on the rate of polymerization, number-average chain length, and branching level. The authors present results from their steady-state model in comparison to experimental data, examining the reduction in the polymerization rate due to mid-chain radicals formed from either backbiting or intermolecular chain transfer to polymer, as mid-chain radicals are much less reactive than secondary radicals [79]. Their simulation results show that the exclusion of backbiting leads to significant deviation of the simulated polymerization rate from the trend of the experimental data, while the exclusion of intermolecular chain transfer does not prevent the simulation from reproducing the experimental trend. Based on the level of branching measured by NMR, the authors then estimate the backbiting rate at each of the experimental temperatures and show that their Arrhenius fit is in good agreement with existing

data for the backbiting rate of butyl acrylate [79].

CHAPTER III

SPATIALLY-RESOLVED MODEL

3.1 Introduction

For both emulsion and miniemulsion polymerization, many significant end-use applications involve varying the particle morphology and composition to obtain a specific set of properties. Emulsion polymerization may be used to produce core-shell particles using multiple monomers, imparting the combined properties of the polymers to products such as impact modifiers [52] or pressure-sensitive adhesives [14]. Core-shell morphologies are useful in applications involving encapsulation, ranging from drug delivery to the safe handling of toxic substances [120]. Drug release profile and encapsulation efficiency may be affected by both molecular weight and particle morphology [17, 124]. Understanding the development of particle morphology as a function of both polymerization kinetics and polymer diffusion may reduce the number of bench experiments required before the desired properties are achieved, resulting in more efficient process development, and also might enable finding a solution closer to optimal.

3.2 Modeling Approach

The spatially-resolved model developed for this work superimposes a monomer droplet onto a face-centered cubic (FCC) lattice, allowing each lattice site to have a maximum coordination number of 12. Sites at the particle surface have fewer than 12 nearest-neighbors. The primary index for each site is the site number, ranging from one to the total number of lattice sites. Each lattice site represents a single substituent molecule, including monomers, bonded mers, and radicals, as observable in Figure 10.

Oil-soluble initiator molecules, which typically dissociate to form two radicals, occupy two adjacent lattice sites. Each site type is assigned a reference number. The state of each lattice site is given by the site type and the chain number. A chain number of zero is assigned to monomers and initiator molecules. A non-zero chain number is assigned to each radical upon its appearance in the particle, whether the radical is formed through oil-soluble initiator dissociation or is absorbed into the particle.

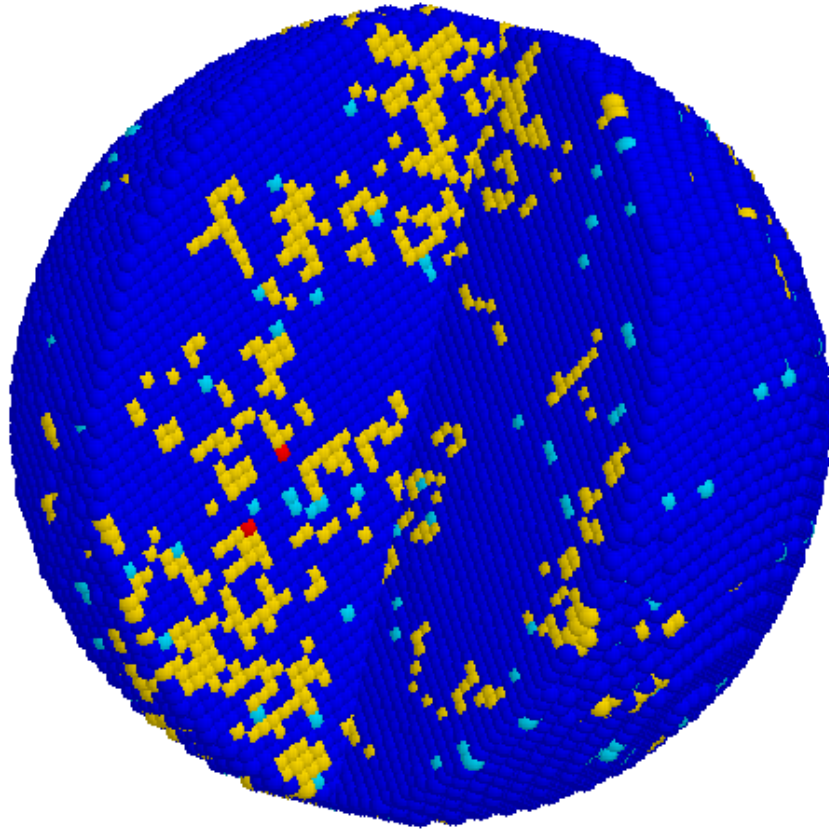


Figure 10: Example of a particle from the spatially-resolved model, where the blue lattice sites represent monomers, the yellow lattice sites represent monomers bonded in polymer chains, the turquoise lattice sites represent undissociated oil-soluble initiator molecules, and the red sites represent radicals.

3.2.1 Model Arrays and Algorithm

Events within the particle, including both reactive and diffusive events, are selected randomly according to the kinetic Monte Carlo (KMC) algorithm [35, 44], depending

upon the number of radicals and chains within the particle. The total sum of rates for all possible events is calculated by:

$$K_{sum} = \sum_{i=1}^N E_i K_i, \quad (1)$$

where E_i is the number of possible events of type i for the current population of chains and K_i is the molecular rate constant for each event of type i . Each product $E_i K_i$ represents a bin for event i relative to the total K_{sum} . A uniformly distributed random number is selected using the Mersenne Twister random number generator [72], and the bin in which the random number is located determines the event to be executed. The time step for each event is determined by:

$$\tau = \frac{-\ln(x_r)}{K_{sum}}, \quad (2)$$

where x_r is a uniformly distributed random number in the interval $(0, 1]$. After each event is executed, the arrays describing the lengths of all live and dead chains are updated, and E_i is recomputed — K_i remains constant throughout.

In KMC simulations, one possible implementation of the algorithm is to first select a potential event, involving processes such as reaction or diffusion, and then determine if the event is possible [35]. This approach may result in a significant number of events being rejected as physically impossible, substantially increasing the computational time required for the simulation. The spatially-resolved model uses the converse approach, where all possible events are stored using a combination of several arrays, eliminating the need to reject any selected events. Although this method reduces the computational time, the memory requirements are substantially increased, requiring in excess of 4 gigabytes for a particle with a diameter greater than 100 nm. For each possible event, the main event array contains the site numbers of the two lattice sites whose states will be modified upon execution of the event, sorted by event type. The other event arrays store the row number where each event is located within the main event array, indexed by both the primary site number for the

event and the event type. After each event is executed, the event arrays are updated for any sites whose states changed during the execution of the event.

3.2.2 Polymer Diffusion

3.2.2.1 Model Details

Diffusion of the polymer chains in the spatially-resolved model is achieved through both bond fluctuation and reptation, and is only possible where a bonded mer or unit radical may move to an adjacent lattice site occupied by a monomer. A polymer site is not allowed to displace another polymer site, and since this model does not include vacant lattice sites, monomers are the only molecules considered mobile enough to concede a lattice site to a bonded mer. Furthermore, a minimum bond angle between mers is enforced for all events, including reactive events, so that chain conformations remain physically plausible. A maximum Euclidean bond length between mers of 1.5 is always enforced, as this only allows bonds between nearest-neighbor sites on the lattice, between which the distance is $\sqrt{2}$, or approximately 1.41. Unless otherwise noted, a minimum bond angle between mers of 60° is used to approximate a real chain, as this is the smallest bond angle achievable in the lattice using the maximum bond length of 1.5, where the calculated bond angle between mers for a real, off-lattice chain is 39° , as shown in Figure 11. The angle of 39° assumes a uniform tetrahedral angle of 109.5° between the backbone carbon atoms, as this bond angle minimizes the repulsion of the substituents bonded to a carbon atom whenever all of the substituents are identical. This calculation assumes that the differences between the substituent groups on each backbone carbon atom in a polymer chain do not cause a significant variation from the tetrahedral bond angle.

Bond fluctuation is accomplished through the swapping of a bonded mer with a monomer occupying an adjacent lattice site, as shown in Figure 12(a). For such an event to be added to the event list, all of the resulting bond angles and bond lengths are checked to ensure that they are within the specified constraints. Unitary

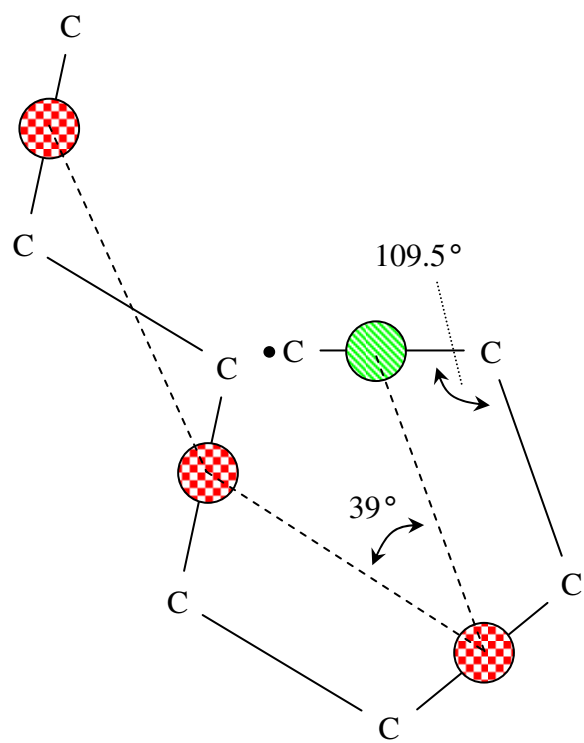


Figure 11: Two-dimensional representation of the minimum bond angle between mers overlaid on the carbon backbone of a polymer chain, with the bonded mers shown in checkerboard red, the radical shown in diagonal green, and the bonds between mers represented by dashed lines. This figure also depicts a backbiting event according to the traditional definition of backbiting, a topic which will be addressed later in this chapter.

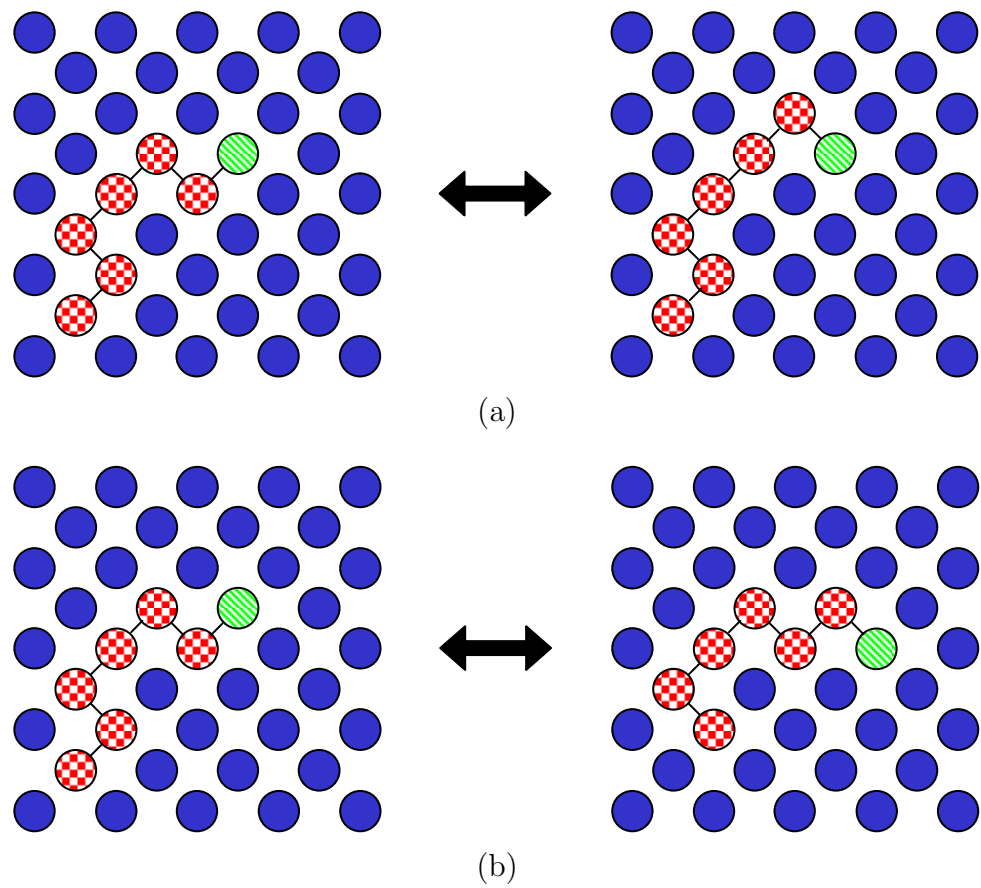


Figure 12: Two-dimensional representation of a chain on the FCC lattice, illustrating (a) bond fluctuation and (b) reptation, with monomers in solid blue, bonded mers in checkerboard red, and radicals in diagonal green.

radicals may move from site to site without any restrictions, save that a monomer is displaced. Execution of a bond fluctuation event is straightforward, primarily requiring modification of site numbers in the arrays that track connectivity between mers. Reptation, as defined for the model, involves shifting the chain along its existing conformation by one lattice site, as shown in Figure 12(b). As the chain may move toward either of its ends, reptation events are added to event list for both ends of a chain, where such events must satisfy the bond angle and bond length constraints. To execute a reptation event, a mer is removed from one end of the chain and placed at the other end of the chain at the desired lattice site, and the site types are updated appropriately. The displaced monomer is moved to the opposite end of the chain, where the bonded mer was removed.

3.2.2.2 Oligomer Diffusion

Initially, bond fluctuation was the only diffusive event included in the model. The rate constant for bond fluctuation f was set according to the following equation:

$$D = \frac{1}{6}fL^2 \quad (3)$$

where the diffusivity D is taken to be the monomer diffusivity and L is the the distance between nearest-neighbor lattice sites. For a monomer, f is the rate of hopping to an adjacent lattice site, and the value of f is determined using values of monomer diffusivity obtained from the literature; L is the distance of each hop. The factor of $1/6$ comes from the fact that a monomer can move in either a positive or negative direction relative to x, y, and z axes. Hopping of bonded mers via bond fluctuation is assumed to occur at the same rate of hopping f calculated for a monomer. The value of L is calculated as

$$L = \frac{d_p\sqrt{2}}{S_{max} - S_{min} + 1} \quad (4)$$

where d_p is the particle diameter and S_{max} and S_{min} are the maximum and minimum x, y, or z coordinate values of FCC lattice sites in the particle, so the term $S_{max} - S_{min} + 1$

represents the distance in x, y, or z coordinates spanning the particle. The particle volume V_p is calculated as

$$V_p = \frac{N_{sites} MW_{mon}}{\rho_m N_A} \quad (5)$$

where N_{sites} is the total number of occupied lattice sites, MW_{mon} is the monomer molecular weight in g/mol, ρ_m is the monomer density in g/cm³, and N_A is Avogadro's number. The particle radius is calculated as

$$r_p = \left(\frac{3V_p}{4\pi} \right)^{\frac{1}{3}}. \quad (6)$$

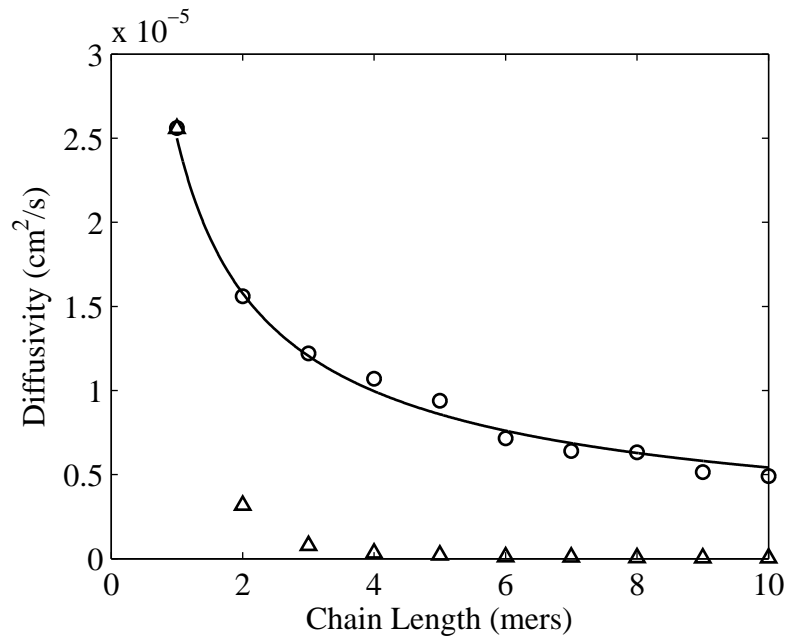


Figure 13: Diffusivity vs. oligomer length, up to a length of 10 mers, using bond fluctuation only (triangle) and reptation only (circle), compared with Griffith's scaling law (line) [51].

The next step was to achieve agreement of the lattice model with published data for the center-of-mass diffusivity of polymer chains. The correlation of Griffiths et al. [51], which was fit to diffusivity data for methyl methacrylate and butyl methacrylate, provides a good benchmark for the center-of-mass diffusion of oligomers:

$$\frac{D_i(w_p)}{D_{mon}(w_p)} = i^{-(0.664+2.02w_p)} \quad (7)$$

where D_i is the diffusivity of an oligomer of length i , D_{mon} is the monomer diffusivity, and w_p is the weight fraction of polymer. A value of 2.08×10^{-5} cm²/s is used for D_{mon} , measured by Griffiths et al. for methyl methacrylate [51]. Figure 13 shows the comparison between Equation (7) and the simulated diffusivity from the lattice model when using only bond fluctuation. Bond fluctuation allows individual mers to move, but this motion is uncoordinated and fails to achieve the center-of-mass motion of chains predicted by Equation (7).

At this point in the development of the model, other approaches were examined for simulating the diffusion of polymer chains. The most prevalent approach discussed in literature is the reptation of chains through a tube defined by the existing chain conformation. The implementation of reptation in the model was straightforward, as this required only a fixed rate for reptation, independent of chain length, to give a scaling of diffusivity with oligomer length that is in good agreement with Griffiths' scaling law [51]. Figure 13 shows the oligomer diffusivity from the model using either reptation or bond fluctuation compared to Equation (7). Reptation produces a coordinated movement of the mers in a chain, thus providing significant center-of-mass motion. Reptation and bond fluctuation may be used simultaneously in the model, but only reptation is necessary to achieve agreement with the diffusivities predicted by Equation (7). The center-of-mass motion resulting from bond fluctuation is so insignificant for oligomers longer than two mers that bond fluctuation may be ignored when examining the center-of-mass motion of polymer chains. Since the rate of bond fluctuation is set according to the monomer diffusivity, it cannot be arbitrarily increased.

3.2.3 Reactions

3.2.3.1 Initiator Dissociation

Within the model, initiator dissociation may occur in either the aqueous phase or the monomer (oil) phase. Water-soluble initiator is present only in the aqueous phase,

Table 1: Macroscopic and molecular rate equations for spatially-resolved model.

Rate	Macroscopic	Units	Molecular	Units
r_p	$k_p[R][M]$	mol/L/s	$k_{p,m}N_{m,0}n_p$	s^{-1}
r_d	$k_d[I]$	s^{-1}	$k_{d,m}N_I$	s^{-1}
r_t	$k_t[R]^2$	mol/L/s	$k_{t,m}N_{pairs}$	s^{-1}

where it dissociates to form radicals. These radicals are placed in empty lattice sites on the surface of the particle according to an adsorption rate. Oil-soluble initiator may be present in both the monomer and aqueous phases, distributed according to a partition coefficient. Only a small fraction of the oil-soluble initiator is present in the aqueous phase. Each oil-soluble initiator molecule within the particle occupies two adjacent lattice sites. Upon dissociation, two oil-soluble initiator radicals are produced. The rate constants for initiator dissociation have natural units of s^{-1} , so no modification is necessary to apply them in the model.

3.2.3.2 Propagation

The rate constant for propagation, k_p , must likewise be converted to units of s^{-1} to be used in the model, as all rates must apply to individual events. This rate constant is scaled from macroscopic units of L/mol/s by multiplying by the initial monomer concentration in the particle, $[M]_0 = N_{m,0}/V_pN_A$, where $N_{m,0}$ is the initial number of monomers in the particle. The molecular rate constant for propagation is calculated as $k_{p,m} = k_p / (11V_pN_A)$. Table 1 shows the macroscopic and microscopic propagation rates, where n_p is the number of propagation events in the particle. Propagation requires a scaling factor of 11 as this is the number of monomers accessible to a radical greater than unit length at zero conversion, using a minimum bond angle between mers of 60° . Radicals of unit length require a separate propagation rate

constant using a scaling factor of 12, as they can react with monomers in any of the 12 nearest-neighbor sites at zero conversion.

3.2.3.3 Termination

The simulation of termination in this model requires more forethought than the simulation of the other reactions, due to the diffusion-dependence of termination. Diffusion and reaction must occur in series for two radicals to terminate, with the combined termination rate constant given by [58]

$$\frac{1}{k_{t,ij}} = \frac{1}{k_t^{chem}} + \frac{1}{k_{t,ij}^{diff} + k_t^{res}} \quad (8)$$

where k_t^{chem} is the rate constant for the chemical reaction of termination between two radicals and

$$k_{t,ij}^{diff} = \pi (D_i + D_j) N_A r_T \quad (9)$$

and

$$k_t^{res} = \frac{4}{3} \pi k_p [M^p] a^2 \delta \quad (10)$$

where i and j are the lengths of the two chains containing the radicals, D_i and D_j are the diffusion coefficients of the two chains, r_T is the maximum distance between radicals for termination to occur, $[M^p]$ is the monomer concentration in the particle, a^2 is the mean-squared end-to-end distance of the chain per monomer, and δ is the Lennard–Jones diameter of a monomer [58]. Based on the concept of the maximum termination distance, the algorithm for termination in the spatially-resolved model checks to see if any radicals are within a specified number of lattice sites of each other, a variable that is generally set to five lattice sites. If a pair of radicals is found to be within this proximity of each other, the algorithm attempts to move the radicals to adjacent lattice sites. If the algorithm can locate a path to move the radicals to adjacent lattice sites, a termination event is added to the event list. The rate for this termination event, given in s^{-1} as with all of the KMC rates, is set high enough

that termination of the two radicals will almost inevitably be the next event that is executed within the simulation.

The termination radius in the model also allows for inclusion of the “cage effect,” the idea that newly-generated oil-soluble initiator radicals will sometimes terminate before they have time to diffuse sufficiently apart from each other [2]. Initiator efficiency, which describes the fraction of radicals that do not escape the cage, may be introduced into the model using the termination radius. However, the typical setup in the model is to force one of the initiator radicals to propagate before termination can occur, as the propagation rate is approximately 10^6 less than the diffusion rates, generally allowing radicals to escape the termination radius after initiator dissociation rather than immediately terminate. Initiator efficiency is then introduced into the model through a separate event, recombination of radicals.

3.3 Combined Reaction and Diffusion Modeling

As previously stated, the primary goal in developing the spatially-resolved model was to examine the evolution of particle morphology during emulsion or miniemulsion polymerization. Once all of the diffusive and reactive events were incorporated into the spatially-resolved model, one issue became abundantly clear: the time scale on which the diffusive events occur, about 10^6 faster than that of the reactive events, makes the concurrent simulation of these events prohibitively slow for any system of a size relevant to examine particle morphology. Concurrent simulation of diffusion and reaction is possible if the difference in time scales can be lessened. The “tau-leaping” algorithm is used for such a purpose by Gillespie [50] to simulate chemical reactions on different time scales, but may be applied to any combination of events, such as reaction and diffusion, as long as two conditions are met. First, a significant number of events of one type must occur between events of another type. With diffusion occurring 10^6 times faster than any chemical reactions in the model, this

condition is clearly met. Second, the change in the state of the system must be negligible. To illustrate the negligible change in the particle between diffusive events, the scaling law for styrene oligomers derived by Piton et al. [87] is used, with a monomer diffusivity of $2.81 \times 10^{-5} \text{ cm}^2/\text{s}$ at $50 \text{ }^\circ\text{C}$. At these conditions, a chain of 1000 mers would have a diffusivity of $9.53 \times 10^{-7} \text{ cm}^2/\text{s}$. Using a propagation rate constant of 1999 s^{-1} , a chain of 1000 mers could achieve center-of-mass movement of 218 nm between propagation events at 0% monomer conversion. A chain length of 1000 requires extrapolation of the diffusivity relation, but for shorter chains, the diffusion distance is even longer. Clearly, both conditions required for tau-leaping are met by the spatially-resolved model given that a chain length of 1000 mers is long for the monomers considered here, including both styrene and butyl acrylate, and that the maximum particle diameter simulated using the spatially-resolved model is around 100 nm.

3.4 Cumulative Distribution Function for Backbiting

In addition to simulating the development of particle morphology in emulsion or miniemulsion particles, the spatially-resolved model also lends itself to examination of mechanisms involving chain diffusion or configuration at scales less than that of the full particle. One such mechanism is intramolecular chain transfer to polymer, referred to here as backbiting. While the traditional definition of backbiting only describes chain transfer to a carbon five-removed from the radical, as shown in Figure 11, this model is used to quantify the probability of backbiting at any distance from the radical, thus allowing examination of the distribution of branch lengths resulting from backbiting. Chain conformation in various acrylates and methacrylates has been studied using rotational isomeric states-Metropolis Monte Carlo, giving good agreement with experimentally measured values for properties such as radius of gyration [24, 59]. The KMC lattice model requires fewer inputs and is less computationally

intensive, but it also requires the assumption that the polymer is in a good solvent.

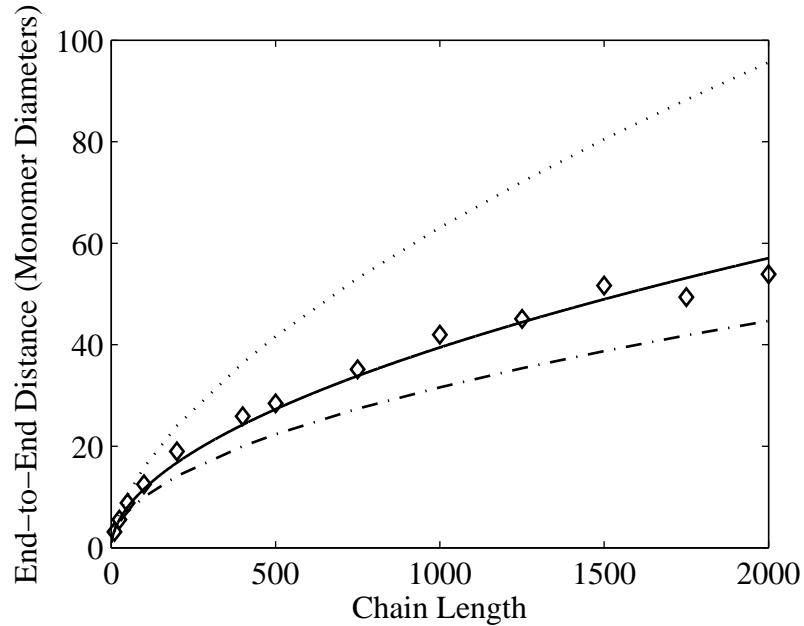


Figure 14: End-to-end distance of polymer chains vs. chain length, with a power-law exponent of 0.6 representing good solvents (dotted line), an exponent of 0.5 representing theta solvents (dash-dot line), and simulation data from the spatially-resolved model (diamond) fit with a power-law equation (solid line), giving an exponent of 0.53.

The system under consideration here is a butyl acrylate solution polymerization using a solvent consisting primarily of xylene isomers [79]. All of the xylene isomers are known to be good solvents for butyl acrylate [85], so the power-law scaling of end-to-end distance with chain length should approach an exponent of 0.6 [46]. When using the lattice KMC model to simulate chain conformation, the end-to-end distance scales with an exponent of 0.53, according to the least-squares fit. From a physical standpoint, the chain conformation is reasonable, as the exponent in a theta solvent would be 0.5, but the chains are somewhat more constrained than would be expected in a good solvent. The constraints applied in superimposing a chain on the FCC lattice are probably responsible for the deviation of the chain conformation from that expected in a good solvent.

The backbiting simulations are begun by growing a single, linear polymer chain of

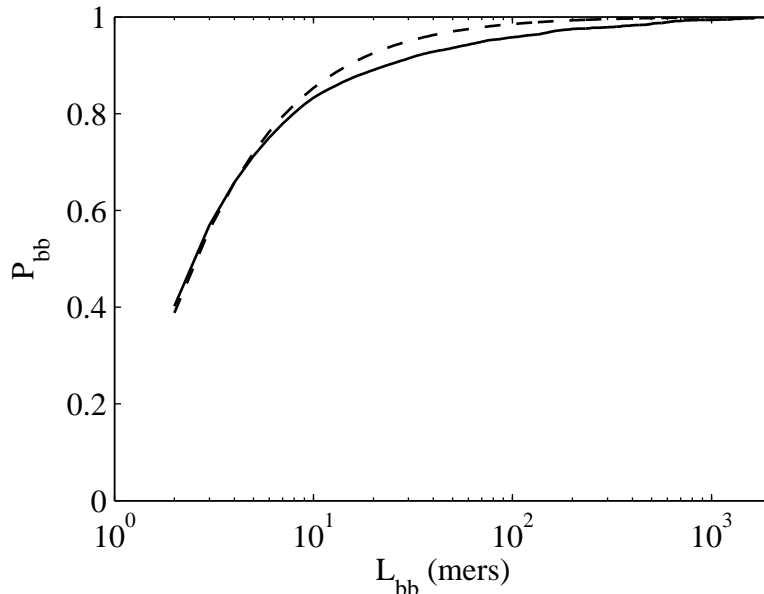


Figure 15: Cumulative distribution function of backbiting rate constant, obtained from the KMC lattice simulations using chains of length 10 to 2000 mers (solid line), and calculated using the scaling $1/(L_{bb} + 1)^2$ (dashed line) [121].

a fixed length, up to 2000 mers, on the FCC lattice, using a spherical system boundary of radius 58 nm. Once the chain has reached the desired length, propagation is halted and the chain is “equilibrated” using a total of 1000 bond fluctuations per mer. Lastly, the chain is allowed to diffuse via bond fluctuation for 100 additional bond fluctuations per mer, and each time the radical occupies a lattice site adjacent to another mer in the chain, the distance along the chain of this mer from the radical is recorded. This process is repeated 100 times each for chains of length ranging from 10 to 2000 mers, and the cumulative distribution function for backbiting probability, shown in Figure 15, is calculated by averaging over the contact probabilities for all simulated chain lengths. As is evident from Figure 15, the majority of backbiting events occur near the radical, with more than 80% of the resulting branches being 9 mers or less in length. Using a branch cutoff length, or minimum long-chain branch length, of 10 mers, a noticeable amount of long-chain branches should be present.

While the backbiting CDF obtained from the KMC lattice simulations is used

in the work presented in this thesis, an alternative view of the backbiting reaction could be to consider it as the formation of a ring in a polymer chain. Wall et al. [121] showed that the probability of ring formation, for polymer chains on a simple cubic lattice, scales with chain length as $1/(L_{bb} + 1)^2$, where L_{bb} is the backbiting distance from the radical, corresponding to Figure 15, and an additional mer is added to give the total ring size, since the value of L_{bb} excludes the radical. Both the CDF calculated from this inverse-squared scaling and the CDF obtained from the lattice KMC simulations are plotted in Figure 15. The two CDFs compare well at short distances from the radical, but the CDF obtained from the KMC simulations underpredicts the probability of branch formation at longer distances. The work presented in this thesis makes only qualitative predictions regarding branch length and the mechanisms of branch formation, so the discrepancy between the CDFs should be insignificant in terms of the conclusions of this work.

CHAPTER IV

WELL-MIXED MODELS

4.1 Well-Mixed Discrete Model

4.1.1 Introduction

In the previous chapter, the simulation of chain diffusion in combination with reactions was shown to significantly increase the run time for simulating polymerization in an emulsion or miniemulsion particle. The analysis of diffusion distances for chains within the spatially-resolved model shows that chains of high molecular weight may transverse a particle of significant diameter within a time span between occurrences of the fastest reactive event, which is propagation for the systems with which the modeling studies presented here are concerned. Based on this analysis, the hypothesis is formed that the reaction kinetics within a particle may be simulated off-lattice using a population-balance kinetic Monte Carlo (KMC) approach, giving acceptable agreement with experimental data taken from the literature at low to moderate values of monomer conversion while neglecting the effects of diffusion on both termination and propagation at higher conversions. Such a model should substantially decrease the required simulation time but still provide significant insight into the effects of the reaction kinetics on observed variables that define both the particle properties and the chain microstructure.

4.1.2 Modeling Approach

4.1.2.1 Primary Arrays

While the array structure for the well-mixed KMC model is much more compact than that of the spatially-resolved KMC model, a substantial level of detail is still required to track the specific state of each polymer chain. The general state of each chain

is described by the number of mers, radicals, branches, and terminal double bonds. The state of each radical is described by the chain on which it is located and the location of the radical on the chain. Radicals may be secondary, bonded to only one mer, or mid-chain, bonded to two mers. Mid-chain radicals are formed through either backbiting or intermolecular chain transfer to polymer. After initiation, a chain starts as a single, linear segment, denoted as the primary segment for the chain. A secondary radical may be located at either end of the primary segment. When branching occurs, a secondary radical may be located at the end of a branch. The type of molecule at the end of each primary segment or branch, in addition to being a secondary radical, may also be an initiator fragment, regular mer, or terminal double bond. Since such a level of detail is possible in this model, knowledge of the end group is retained for use in the backbiting algorithm, as only regular mers are allowed to receive a radical through chain transfer.

Each branch is assigned an identification number when it is generated. To provide a detailed record of the architecture of each polymer molecule, the state of each branch is given by the number of the chain, the number of the “parent” branch off of which it grows, the number of the mer, or position, on the parent branch, and the branch length. The primary segment in each chain is denoted by a “branch” number of zero. The branching structure as stored in these arrays is fixed, such that the primary segment is not normally the longest continuous string of segments in a chain, since continuously updating the branching arrays would require significant computational time. Knowledge of the branching structure is necessary for constructing the backbiting arrays, which track the number of mers at a given distance from the radical to a maximum distance of 5000 mers, far exceeding the limit of 2000 mers in the current backbiting cumulative distribution function (CDF). Since there may be multiple mers at the same distance from a radical, where these mers are located on different branches, another array tracks the branch number of each mer at the given

distance.

4.1.2.2 Reactions

All of the models incorporate a general set of reactions for free-radical polymerization. The following set of reactions is comprehensive, but not every reaction is used in each model, and the text in this chapter will primarily refer to the macroscopic rate equations given in Table 2, with the remaining terms discussed in later chapters. The majority of the reactions are taken from Nikitin et al. [79], except that termination is assumed to occur by combination only, as termination in both butyl acrylate and styrene, the monomers of concern in this work, has been shown to occur predominantly by combination [16, 75]. Neither absorption nor desorption of radicals are included in Nikitin’s model [79], as his experiments with butyl acrylate were conducted using solution polymerization. Oil-soluble initiators dissociate to form two initiator radicals:



where I is an initiator molecule and R_0 is an initiator radical, with the reaction rate shown as r_d in Table 2. Either water-soluble or oil-soluble initiators may be defined for the well-mixed KMC model. The number of initiator molecules in both the aqueous and monomer phases may be given as inputs, so a water-soluble initiator may be used by setting the value for the monomer phase to zero, and an oil-soluble initiator may be partitioned between the aqueous and monomer phases. Radicals in the aqueous phase are absorbed into the particle, with the rate of absorption based on the time for a radical in the aqueous phase to reach a critical entry length where the live chain is no longer sufficiently soluble in the aqueous phase. The molecular rate constant for absorption is calculated as:

$$k_{abs,m} = \frac{k_p [M]_{aq}}{j_{crit} - 1} \quad (12)$$

Table 2: Macroscopic and molecular rate equations for well-mixed models.

Rate	Macroscopic	Units	Molecular	Units
r_d	$k_d[I]$	s^{-1}	$k_{d,m}N_I$	s^{-1}
r_p	$k_p[M][R]$	mol/L/s	$k_{p,m}N_m n$	s^{-1}
$r_{tr,m}$	$k_{tr,m}[M][R]$	mol/L/s	$k_{tr,m,m}N_m n$	s^{-1}
$r_{tr,s}$	$k_{tr,s}[S][R]$	mol/L/s	$k_{tr,s,m}N_s n$	s^{-1}
$r_{tr,p}$	$k_{tr,p}[R][P]\mu_n$	mol/L/s	$k_{tr,p,m} \sum_{i=1}^n \left(\sum_{j=1}^{N_c} M_j - M_i \right)$	s^{-1}
r_{bb}	$k_{bb}^*[R]$	mol/L/s	$\sum_{i=1}^n \sum_{j=2}^{1999} k_{bb}(j) m_{i,j}$	s^{-1}
$r_{p,tdb}$	$k_p[P^=][R]$	mol/L/s	$k_{p,m}N_{tdb}n$	s^{-1}
$r_{p,mcr}$	$k_{p,mcr}[M][MCR_{tot}]$	mol/L/s	$k_{p,mcr,m}N_m n_{mcr}$	s^{-1}
$r_{p,tdb,mcr}$	$k_{p,mcr}[P^=][MCR_{tot}]$	mol/L/s	$k_{p,mcr,m}N_{tdb}n_{mcr}$	s^{-1}
$r_{tr,m,mcr}$	$k_{tr,m,mcr}[M][MCR_{tot}]$	mol/L/s	$k_{tr,m,mcr,m}N_m n_{mcr}$	s^{-1}
r_t	$k_t[R]^2$	mol/L/s	$k_{t,m}N_{pairs}$	s^{-1}
$r_{t,mcr}$	$k_{t,mcr}[MCR_{tot}]^2$	mol/L/s	$k_{t,mcr,m}N_{pairs,mcr}$	s^{-1}
$r_{t,h}$	$k_{t,h}[R][MCR_{tot}]$	mol/L/s	$k_{t,h,m}N_{pairs,hyb}$	s^{-1}
r_{abs}	—	—	$k_{abs,m}n_{aq}$	s^{-1}
r_{des}	—	—	$k_{des,m}n$	s^{-1}

where $[M]_{aq}$ is the monomer concentration in the aqueous phase and j_{crit} is the critical entry length. The molecular rate equation for absorption is given as r_{abs} in Table 2, where n_{aq} is the number of aqueous-phase radicals. Live chains may desorb from the particle if their length is less than j_{crit} , so in the molecular rate equation for

desorption, shown as r_{des} in Table 2, the value of n , the number of secondary radicals, is limited to radicals in chains of length less than j_{crit} . For all other molecular rate equations given in Table 2, n represents the total number of secondary radicals in a particle. Initiator radicals are numbered as the first mer, since the KMC model is not set up to handle radicals of zero length, an artifact of the spatially-resolved model, where all radicals are placed in individual lattice sites, so both initiator radicals and monomeric radicals are considered to be unit length and contribute equally towards a chain reaching j_{crit} . The rate constant for desorption is a variable in the KMC model and is varied as multiples of the propagation rate constant, a point which will be addressed in the next chapter. Absorption and desorption are not included for the simulations using butyl acrylate, as these simulations are for solution polymerization, and the finite system size necessary for these simulations is artificial for the case of solution polymerization. Propagation of a secondary radical on a polymer of size i mers produces a radical of size $i + 1$ mers:



where R_i and R_{i+1} are radicals, and the rate equation is given as r_p in Table 2.

Chain transfer to monomer from a secondary radical produces a dead chain of length i :



where P_i is a dead chain and R_1^- is a monomeric radical, with the rate equation given as $r_{tr,m}$ in Table 2.

The R_1^- radical is unique in that it has an unreacted double bond. When this radical propagates, a terminal double bond is left in the end group:



where R_2^- is a chain of length 2 containing a radical and a terminal double bond. This terminal double bond may react with another radical, forming a branch point. Terminal double bond polymerization is included in the well-mixed kinetic Monte Carlo (KMC) model for the butyl acrylate simulations only, and its rate constant is set equal to k_p , the rate constant for propagation:



where P_i^- may be a live or dead chain, and R_{i+j} is a chain with one or more radicals and one additional branch point. The rate equations for terminal double bond polymerization are given for secondary and mid-chain radicals as $r_{p,tdb}$ and $r_{p,tdb,mcr}$, respectively, in Table 2, where n_{mcr} is the number of mid-chain radicals in the particle. Due to a lack of available data in literature regarding the propagation rate to terminal double bonds in butyl acrylate, this propagation rate constant is assumed to be equal to the general propagation rate constant k_p [96]. Within the KMC model, the number of terminal double bonds is an additional state that is tracked for each chain, with the total number of terminal double bonds in the particle given as N_{tdb} in Table 2. A radical is not allowed to propagate to a terminal double bond on its own chain, as this would form a ring, and we choose to exclude such a structure from the simulation, an assumption justifiable by the low probability of forming such a structure, given that the number of terminal double bonds in the system is insignificant compared to the number of monomers at low to moderate monomer conversion.

Chain transfer to solvent produces a dead chain and a primary radical:



where S is a solvent molecule and P_i is a dead chain, with the rate equation given as $r_{tr,s}$ in Table 2. The rate constant for chain transfer to solvent, $k_{tr,s}$, is calculated from the number-average chain length, accounting for the effects of termination and chain

transfer to monomer [79]. Within the KMC simulation, a solvent radical is assigned a length of 1, as the simulation is not set up to handle radicals of zero length.

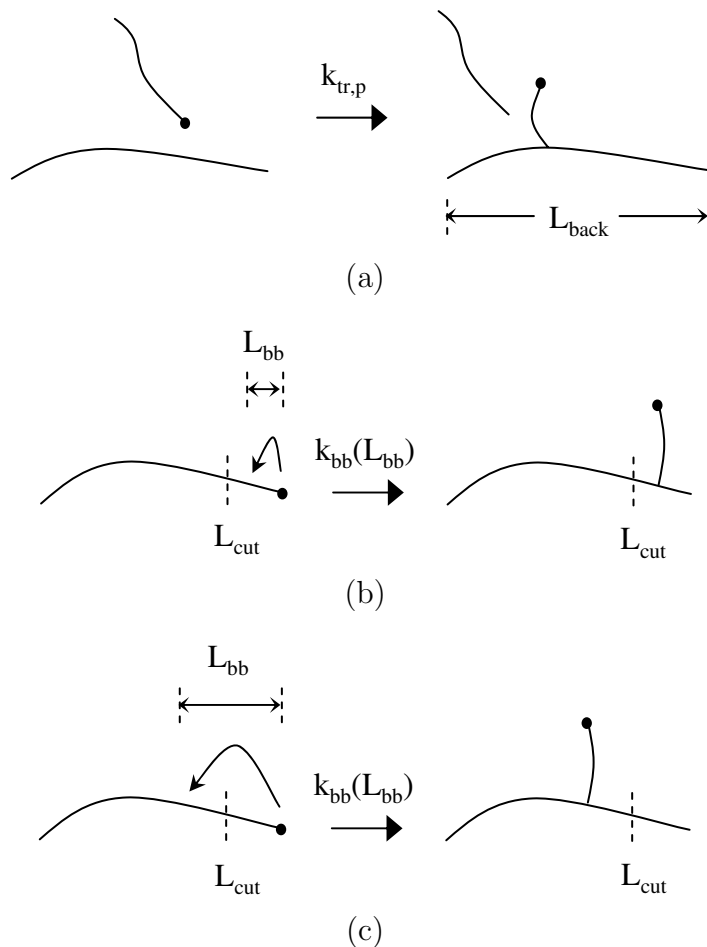


Figure 16: Three possible mechanisms for the formation of branches: (a) intermolecular chain transfer to polymer, (b) backbiting to produce a short-chain branch, and (c) backbiting to produce a long-chain branch. L_{back} is the backbone length, L_{cut} is the branch cutoff length, and L_{bb} is the backbiting distance.

Previous authors have defined short-chain branches as being generated exclusively by backbiting and long-chain branches as being exclusively generated by intermolecular chain transfer to polymer. This model makes no such assumptions about the origin of branches. The term “backbiting,” which often refers to only intramolecular chain transfer involving a six-carbon ring, refers in this work to all intramolecular chain transfer. Figure 16 illustrates the possible mechanisms for the formation of

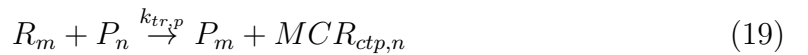
short-chain and long-chain branches from both intermolecular chain transfer to polymer and backbiting, where L_{bb} is the backbiting distance from the radical. Using the backbiting CDF, backbiting is allowed to produce long-chain branches, as illustrated in Figure 16(c). Intermolecular chain transfer to polymer, shown in Figure 16(a), is allowed to produce short-chain branches, as the probability of this reaction is assumed to be equal for all mers along a polymer chain. The maximum cutoff length for short-chain branches, labeled as L_{cut} in Figure 16, is varied to examine its effect on predicted properties such as intrinsic viscosity.

Backbiting by a radical of length i produces a mid-chain radical:



where $MCR_{bb,i}$ is the corresponding mid-chain radical. The backbiting rate constant k_{bb} is variable, based on the backbiting distance L_{bb} , as noted in Figure 16.

Intermolecular chain transfer to polymer produces a dead chain and a mid-chain radical:



where P_n and P_m are dead chains and $MCR_{ctp,n}$ is the mid-chain radical corresponding to P_n . The origin of individual mid-chain radicals in the KMC model is indistinguishable in the final results, whether they are formed through backbiting or intermolecular chain transfer to polymer, as the capability to track the origin of branches is not included in the model. Furthermore, such tracking of branch origin events would become somewhat irrelevant when the structure of each polymer chain is reconfigured in the final calculations to determine the longest continuous string of segments. The mid-chain radicals are labeled separately here according to their event of origin since this set of reactions will also be utilized in the rate-equation model.

Propagation of a mid-chain radical to a monomer yields a secondary radical:



where the mid-chain radical may be formed through either backbiting or intermolecular chain transfer to polymer, and the combined concentration of both these species is denoted as $[MCR_{tot}]$ in Table 2. In the well-mixed KMC model, a secondary radical formed through propagation of a mid-chain radical is treated no differently than any other secondary radical, meaning that such a secondary radical can backbite.

Chain transfer to monomer from a mid-chain radical produces a dead polymer chain and a radical of length one:



Termination by combination of two secondary radicals produces a dead chain, with a rate constant of k_t :



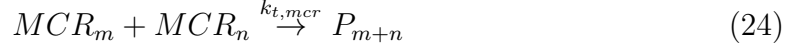
When any termination event occurs in the well-mixed KMC model, the branching structure must be combined into a single chain, so the longest primary segment is located and the branches in the combined chain are updated accordingly. A termination reaction is the only time outside of the final calculations where the description of the branching topology of a chain is reconfigured.

Hybrid termination of a secondary radical R_m and a mid-chain radical MCR_n produces a dead chain, with a rate constant of $k_{t,h}$:



Hybrid termination produces one additional branch, resulting from the single mid-chain radical.

Termination of two mid-chain radicals produces a dead chain, with a rate constant of $k_{t,mcr}$:



Termination between two mid-chain radicals produces two additional branches.

4.1.3 Viscosity

For the simulation of butyl acrylate solution polymerization, the intrinsic viscosity is calculated using an algorithm outlined by Bovey, et al. [25] While this algorithm is typically employed to calculate the number of long-chain branches per molecule using measurements of linear-chain and branched-chain viscosity, the algorithm is used in reverse here to calculate the intrinsic viscosity of the branched chains given the predetermined branch structure. The average concentrations mentioned in the following discussion of the algorithm apply only to the rate-equation model. To apply this algorithm to the well-mixed KMC model, each polymer chain must be examined to locate the longest continuous string of segments, as this is the standard method for defining the structure of polymer chains. This process is repeated for each polymer chain in the simulation, and then the weight-average intrinsic viscosity is calculated. First, the ratio of the branched-chain to the linear-chain mean-squared radius of gyration is calculated from Equation (25), derived by Zimm and Stockmayer [126]:

$$g_f(n) = \frac{3}{(f-1)n_{lcb} + 3} \left[1 + \sum_{j=1}^{n_{lcb}} (f-1)^j \prod_{i=0}^j \frac{n_{lcb} - i}{(f-1)n_{lcb} + 2 - i} \right] \quad (25)$$

where f is the total number of bonds a monomer can form, which is 3 for butyl acrylate, and n_{lcb} is the number of long-chain branches on a chain. The number of long-chain branches per chain is determined from the following equation:

$$n_{lcb} = \frac{[B_{lcb}]}{[P_{tot}]} \quad (26)$$

Knowing the value of g_f from Equation (25), the ratio of the branched-chain to the linear-chain intrinsic viscosity is calculated:

$$G_{lcb} = \sqrt{g_f} = \sqrt{\frac{s_{br}}{s_l}} \quad (27)$$

where s_{br} is the radius of gyration of the branched molecule, and s_l is the radius of gyration of a linear molecule of the same molecular weight. The linear-chain intrinsic viscosity is calculated from the Mark-Houwink-Sakurada equation [21]:

$$[\eta_l] = K (M_v)^a \quad (28)$$

where $K = 6.85 \times 10^{-3}$ and $a = 0.75$ [26], $[\eta_l]$ is in units of mL/g, and M_v is the viscosity-average molecular weight, calculated as [21]

$$M_v = \left(\sum_{i=1}^{\infty} w_i M_i^a \right)^{(1/a)} \quad (29)$$

where w_i is the weight fraction of chains of molecular weight M_i . In the well-mixed KMC model, M_v may be determined explicitly based on the molecular weight of each chain, but in the rate-equation model only M_n may be calculated, based on the concentration of chains and the monomer consumed, so M_n must be substituted for M_v in Equation (28) in the rate-equation model. At this point, the long-chain-branched intrinsic viscosity $[\eta_b]$ may be determined, using the following equation:

$$G_{lcb} = \frac{[\eta_b]}{[\eta_l]}. \quad (30)$$

The value $[\eta_b]$ does not account for the effect of short-chain branches, which may also reduce the mean-squared radius of gyration. The effect of short-chain branching is estimated using the following correlation [63]:

$$G_{scb} = 1.0 - 1.56w_{scb} \quad (31)$$

where w_{scb} is the weight fraction of short-chain branches. The value of w_{scb} is calculated from the rate-equation model results according to

$$w_{scb} = L_{scb} \frac{[B_{scb}]}{[P_{tot}]} \frac{1}{\mu_n} \quad (32)$$

where L_{scb} , the average length of a short-chain branch, is determined using the backbiting CDF. The corrected value of the branched intrinsic viscosity is calculated as

$$[\eta_{corr}] = G_{lcb} G_{scb} [\eta_l]. \quad (33)$$

4.2 *Well-Mixed Rate-Equation Model*

4.2.1 Introduction

The advent of nuclear magnetic resonance (NMR) spectroscopy techniques to measure branching levels has raised the possibility of quantifying and modeling short-chain and long-chain branching by combination of NMR and intrinsic viscosity data. As the amount of long-chain branching in butyl acrylate is undetectable through intrinsic viscosity measurements [34], a thorough examination of branching kinetics is necessary to obtain at least a qualitative understanding of these long-chain branches. The rate-equation model presented here [100] provides a method to examine the levels of short-chain and long-chain branching and also discriminates between mid-chain radicals produced by backbiting or intermolecular chain transfer to polymer. Although details regarding the microstructure of individual chains are not accessible through the rate-equation model, as they are through the well-mixed discrete model, the rate-equation model is much less computationally intensive than the discrete model. If the branching predictions obtained from the discrete model are taken to be more accurate than those of the rate-equation model, according to the higher level of detail, then comparison of the branching predictions between the rate-equation and discrete models may lead to further refinement of the branching calculations in the rate-equation

model.

4.2.2 Rate Equations

Having specified all chemical reactions to be included in the model, we now define the corresponding ordinary differential equations. The first equation accounts for the dissociation of the initiator:

$$\frac{d[I]}{dt} = -k_d [I] \quad (34)$$

Secondary radicals are formed through initiator dissociation and propagation of mid-chain radicals, and are lost through termination, backbiting, and intermolecular chain transfer to polymer:

$$\begin{aligned} \frac{d[R_{tot}]}{dt} = & 2fk_d [I] - 2k_t [R_{tot}]^2 - k_{t,h} [R_{tot}] [MCR_{ctp}] \\ & - k_{t,h} [R_{tot}] [MCR_{bb}] + k_{p,mcr} [M] [MCR_{ctp}] \\ & + k_{p,mcr} [M] [MCR_{bb}] - k_{tr,p} [P] [R_{tot}] \mu_n - k_{bb} [R_{tot}] \end{aligned} \quad (35)$$

where f is the initiator efficiency, $[R_{tot}]$ is the sum of all secondary radical species, including initiator radicals, and μ_n is the number-average degree of polymerization, given by

$$\mu_n = \frac{[M]_0 - [M]}{[P]} \quad (36)$$

where $[M]_0$ is the initial concentration of monomer and $[P]$ is the concentration of dead chains, since the assumption is made that each chain will contain no more than a single radical at a given time. This assumption has been validated for the simulation results. Monomer $[M]$ is consumed through both propagation and chain transfer to monomer of both secondary and mid-chain radicals:

$$\begin{aligned} \frac{d[M]}{dt} = & -k_p [M] [R_{tot}] - k_{p,mcr} [M] [MCR_{ctp}] - k_{p,mcr} [M] [MCR_{bb}] \\ & - k_{tr,m} [M] [R_{tot}] - k_{tr,m,mcr} [M] [MCR_{ctp}] - k_{tr,m,mcr} [M] [MCR_{bb}] \end{aligned} \quad (37)$$

The combined concentration of live and dead chains is represented by $[P_{tot}]$, where all radicals, including initiator and solvent radicals, are included as live chains. Polymer chains are formed by initiator dissociation, chain transfer to monomer, and chain transfer to solvent. Termination between any two radicals, assumed to be only by combination, eliminates one polymer chain.

$$\begin{aligned} \frac{d[P_{tot}]}{dt} = & 2fk_d [I] - k_t [R_{tot}]^2 - k_{t,h} [R_{tot}] [MCR_{ctp}] - k_{t,h} [R_{tot}] [MCR_{bb}] \\ & - k_{t,mcr} [MCR_{ctp}]^2 - 2k_{t,mcr} [MCR_{ctp}] [MCR_{bb}] - k_{t,mcr} [MCR_{bb}]^2 \\ & + k_{tr,m} [M] [R_{tot}] + k_{tr,m,mcr} [M] [MCR_{ctp}] + k_{tr,m,mcr} [M] [MCR_{bb}] \\ & + k_{tr,s} [S] [R_{tot}] + k_{tr,s,mcr} [S] [MCR_{ctp}] + k_{tr,s,mcr} [S] [MCR_{bb}] \end{aligned} \quad (38)$$

Only branches resulting from propagation of a mid-chain radical are observable in the NMR spectrum of poly(butyl acrylate) [68]:

$$\frac{d[B_{bb,NMR}]}{dt} = k_{p,mcr} [M] [MCR_{bb}] \quad (39)$$

$$\frac{d[B_{ctp,NMR}]}{dt} = k_{p,mcr} [M] [MCR_{ctp}] \quad (40)$$

where $[B_{bb,NMR}]$ and $[B_{ctp,NMR}]$ are the concentrations of NMR-observable branches produced by backbiting and intermolecular chain transfer to polymer, respectively. Mid-chain radicals are produced through either backbiting or intermolecular chain transfer to polymer, and are lost through propagation, chain transfer to monomer, chain transfer to solvent, or termination:

$$\begin{aligned}
\frac{d[MCR_{bb}]}{dt} = & k_{bb} [R_{tot}] - k_{p,mcr} [M] [MCR_{bb}] - k_{t,h} [R_{tot}] [MCR_{bb}] \\
& - 2k_{t,mcr} [MCR_{bb}]^2 - 2k_{t,mcr} [MCR_{bb}] [MCR_{ctp}] \\
& - k_{tr,m,mcr} [M] [MCR_{bb}] - k_{tr,s,mcr} [S] [MCR_{bb}] \quad (41)
\end{aligned}$$

$$\begin{aligned}
\frac{d[MCR_{ctp}]}{dt} = & k_{tr,p} [P] [R_{tot}] \mu_n - k_{p,mcr} [M] [MCR_{ctp}] - k_{t,h} [R_{tot}] [MCR_{ctp}] \\
& - 2k_{t,mcr} [MCR_{ctp}]^2 - 2k_{t,mcr} [MCR_{bb}] [MCR_{ctp}] \\
& - k_{tr,m,mcr} [M] [MCR_{ctp}] - k_{tr,s,mcr} [S] [MCR_{ctp}] \quad (42)
\end{aligned}$$

where $[MCR_{bb}]$ and $[MCR_{ctp}]$ are the concentrations of mid-chain radicals resulting from backbiting and intermolecular chain transfer to polymer, respectively. The last two terms in Equation (41) and (42) result from the substitution of the term $[MCR] = [MCR_{bb}] + [MCR_{ctp}]$ into the term $2k_{t,mcr} [MCR]^2$. The total number of branches formed by both backbiting and intermolecular chain transfer to polymer is necessary to examine the effects of branching on viscosity:

$$\begin{aligned}
\frac{d[B_{bb,tot}]}{dt} = & k_{p,mcr} [M] [MCR_{bb}] + k_{t,h} [R_{tot}] [MCR_{bb}] + 2k_{t,mcr} [MCR_{bb}]^2 \\
& + 2k_{t,mcr} [MCR_{bb}] [MCR_{ctp}] \quad (43)
\end{aligned}$$

$$\begin{aligned}
\frac{d[B_{ctp,tot}]}{dt} = & k_{p,mcr} [M] [MCR_{ctp}] + k_{t,h} [R_{tot}] [MCR_{ctp}] + 2k_{t,mcr} [MCR_{ctp}]^2 \\
& + 2k_{t,mcr} [MCR_{bb}] [MCR_{ctp}] \quad (44)
\end{aligned}$$

where $[B_{bb,tot}]$ and $[B_{ctp,tot}]$ are the concentrations of total branches produced by backbiting and intermolecular chain transfer to polymer, respectively. Hybrid termination between a secondary radical and a mid-chain radical produces a single branch, while termination between two mid-chain radicals produces two branches.

4.2.3 Branch Length

Branch length may now be examined using the CDF for backbiting distance. Both backbiting and intermolecular chain transfer to polymer are only accounted for along the backbone of a chain, a reasonable assumption if most of the mers in the chain are contained in the backbone, which is the case in this study. Here the backbone is assumed to be the longest end-to-end combination of segments within a chain. The average backbone length, L_{back} , is calculated as

$$L_{back} = \frac{\mu_n}{2}. \quad (45)$$

μ_n accounts for both live and dead chains, but the number of live chains is very small compared to the number of dead chains. The average length of a live chain, over its entire lifetime, is equal to half its dead length, thus giving Equation (45). Next, the backbiting CDF is normalized so that $p_{bb}^*(L_{back}) = 1$, where $p_{bb}^*(L_{back})$ is the cumulative probability that a radical will backbite along the backbone of a chain. The amount of short-chain branches produced at a given branch cutoff length L_{cut} is described by Equation (46), and the corresponding amount of long-chain branches is given by Equation (47).

$$\begin{aligned} \frac{d[B_{scb}]}{dt} = & \frac{d[B_{bb,tot}]}{dt} p_{bb}^*(L_{cut} - 1) + \frac{d[B_{bb,tot}]}{dt} \left(p_{bb}^*(L_{back} - 1) \right. \\ & \left. - p_{bb}^*(L_{back} - L_{cut}) \right) + \frac{d[B_{ctp,tot}]}{dt} \frac{2(L_{cut} - 1)}{\mu_n} \\ & + (1 - p_l) \left[\frac{d[B_{bb,tot}]}{dt} \left(p_{bb}^*(L_{back} - L_{cut}) - p_{bb}^*(L_{cut} - 1) \right) \right. \\ & \left. + \frac{d[B_{ctp,tot}]}{dt} \left(\frac{L_{back} - 2L_{cut}}{\mu_n} \right) \right] \end{aligned} \quad (46)$$

$$\frac{d[B_{lcb}]}{dt} = \frac{d[B_{ctp,tot}]}{dt} + \frac{d[B_{bb,tot}]}{dt} - \frac{d[B_{scb}]}{dt} \quad (47)$$

The first term in Equation (46) accounts for short-chain branches produced by backbiting near the radical, where $p_{bb}^*(L_{cut} - 1)$ is the cumulative probability that a radical will backbite at a distance less than L_{cut} . The second term in Equation (46) accounts for short-chain branches produced by backbiting at the end of the backbone opposite the radical, where $p_{bb}^*(L_{back} - 1)$ is the cumulative probability of backbiting over the entire backbone length, excluding the last mer at the other end of the backbone, and $p_{bb}^*(L_{back} - L_{cut})$ is the cumulative probability of backbiting along the entire backbone, excluding only the mers that are within the distance L_{cut} of the end of the chain opposite the radical. The third term in Equation (46) accounts for intermolecular chain transfer to polymer that occurs within the distance L_{cut} from each end of the backbone. The final, longest term in Equation (46) contains the factor $(1 - p_l)$. p_l , calculated as

$$p_l = \frac{\frac{k_p[M]}{L_{cut}}}{\frac{k_p[M]}{L_{cut}} + k_t [R_{tot}] + k_{t,h} [MCR_{tot}] + k_{tr,m} [M] + k_{tr,p} [P] \mu_n + k_{tr,s} [S] + k_{bb}} \quad (48)$$

is the probability that a radical transfers to a position on the backbone where a long-chain branch could form, and that the radical adds a number of mers, through propagation, greater than or equal to L_{cut} without reacting in a branch-stopping event, thus ensuring that a long-chain branch is actually produced. Thus, $(1 - p_l)$ gives the probability that a radical propagates for fewer steps than L_{cut} , producing a short-chain branch. A branch-stopping event may be either a chain-stopping event or backbiting, which halts the growth of a branch but does not stop the growth of a chain. Figure 17(a) illustrates the former case where a long-chain branch is produced with a probability of p_l , while Figure 17(b) illustrates the latter case where a short-chain branch is instead produced with a probability of $(1 - p_l)$. In Equation (46), the factor $(1 - p_l)$ is multiplied by the concentration of long-chain branches that should be formed through either backbiting or intermolecular chain transfer to polymer, at a distance greater than L_{cut} from either end of the backbone, as shown in Figure 17.

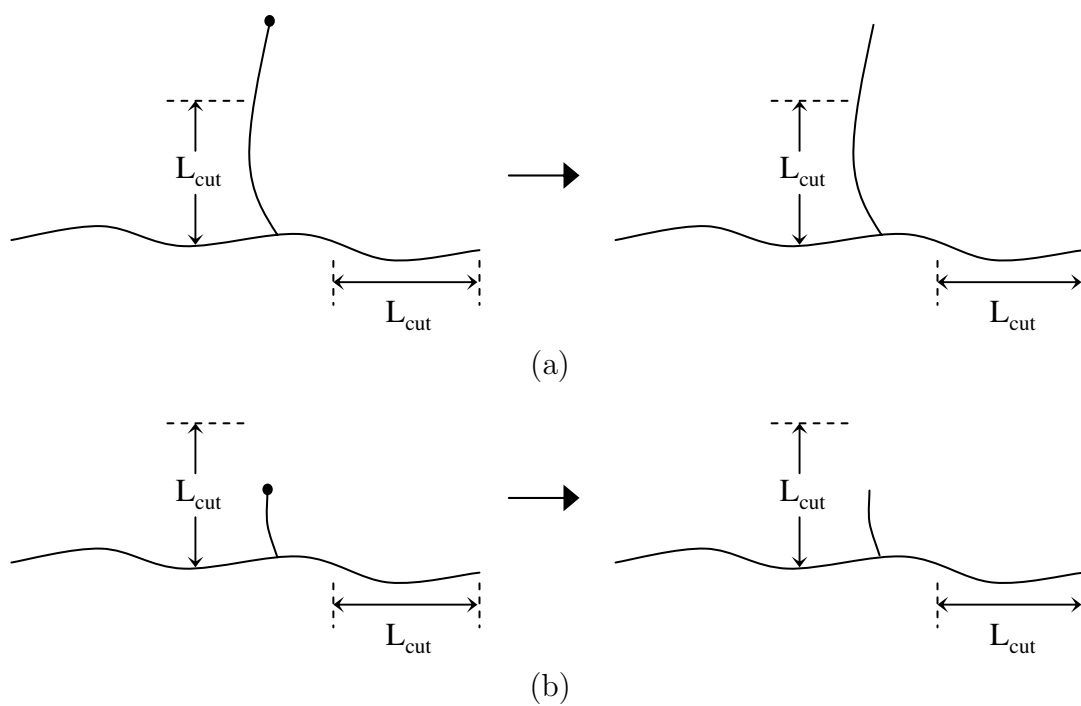


Figure 17: Two possible structures resulting from formation of a branch point via backbiting, where after branching a radical may (a) propagate for a length greater than L_{cut} or (b) react in a branch-stopping event before it propagates to a length of L_{cut} .

CHAPTER V

EXAMINATION OF THE NUCLEATION MECHANISMS OF OIL-SOLUBLE INITIATORS

This chapter presents a comparison between experimental data for the miniemulsion polymerization of styrene and the kinetic Monte Carlo (KMC) simulations performed at the same experimental conditions to study the nucleation mechanisms of oil-soluble initiators in styrene miniemulsion polymerization. The work presented in this chapter has also been published in Reference [99]. Aqueous-phase radicals are thought to play a significant role in miniemulsion polymerization, according to the zero-one assumption, which requires that radical pairs inside a particle terminate quickly without substantial propagation. Four chain-stopping events are considered, accounting for the effects of radical pairs inside a particle as well as aqueous phase radicals on the molecular weight distribution, thus eliminating the zero-one assumption. The two sets of experimental data are at different temperatures and have different particle sizes, allowing consideration of the effects these variables have in determining the dominant chain-stopping event and therefore the importance of aqueous-phase radicals.

5.1 Background

5.1.1 Motivation

The KMC approach used here simulates individual events, such as propagation, initiator dissociation, and termination, using a resolution down to the individual radical and monomer. The molecular rates for these events are either scaled directly from

macroscopic rates, as for propagation and chain transfer to monomer, or else are estimated directly from experimental data, as is the case for termination. This approach allows for a detailed examination of molecular-level mechanisms within the particle while tracking macroscopic observables, such as conversion and molecular weight distribution, which can be measured experimentally. Using a population-balance model such as Asua's [13] with the kinetics used in this work would allow the simulation of particle conversion, but would not describe the molecular weight distribution. The solution algorithm Asua uses to solve the population-balance model does not allow prediction of the molecular weight distribution [13]. Simulation of the molecular weight distribution is essential to gain insight into the molecular-level mechanisms that affect particle nucleation. Having simulation data for both conversion rate and molecular weight allows for better discrimination between the chain-stopping mechanisms.

The concept of singly- and doubly-distinguished particles could be applied here to simulate the molecular weight distribution using population-balance equations (PBEs). Such a methodology has been developed by Butte et al. [30, 31], where PBEs are written for the number of singly- and doubly-distinguished particles, which contain at a minimum one or two radicals, respectively. This classification of particles is subdivided further based on the time of radical generation or entry into the particle, to account for multiple radicals on chains of differing length inside the same particle, which may combine in a short-long termination event. The molecular weight distribution is subdivided into bins via the use of pivot, or average, values of chain length, around which the PBEs are rewritten to compute the fraction of particles in each molecular weight bin [30, 31]. Subdividing the molecular weight distribution permits the simulation of broad or multimodal distributions not readily accessible through techniques such as numerical fractionation [30, 31]. The primary issue in applying the algorithm of Butte et al. [30, 31] to the issue at hand, however, is that

their model does not include radical desorption. While rederivation of their PBEs to include radical desorption should be possible, the use of pivot chain lengths in the solution algorithm, a key feature of the model, significantly increases the complexity of the derivation. As such, the KMC approach applied in this work provides a solution algorithm that, while more computationally intensive, is more straightforward to implement and may be easily adapted to study other aspects of free-radical polymerization kinetics.

5.1.2 Well-Mixed Assumption

The simulation considered here assumes that the particle is well-mixed, or of uniform consistency. This assumption is based on the center-of-mass diffusion of polymer chains being high relative to the typical particle diameter of 100-200 nm, so that a chain could traverse the particle diameter between reactive events such as propagation. Invoking the scaling law for styrene oligomers derived by Piton et al. [87] and using a monomer diffusivity of $2.81 \times 10^{-5} \text{ cm}^2/\text{s}$ at 50 °C, a chain of 1000 mers would have a diffusivity of $9.53 \times 10^{-7} \text{ cm}^2/\text{s}$. The styrene monomer diffusivity at 50 °C is determined by taking the diffusivity at 25 °C [8] and scaling it with an Arrhenius law, where the activation energy used is for the diffusivity of toluene in polystyrene [86]. Using a propagation rate constant of 1999 s^{-1} , a chain of 1000 mers could achieve center-of-mass movement of 535 nm between propagation events at 0% monomer conversion. A chain length of 1000 requires extrapolation of the diffusivity relation, but for shorter chains, the diffusion distance is even longer. The gel effect for styrene is shown by both the new data and Alduncin and Asua's data [6] to be negligible, as the acceleration in the conversion rate that is characteristic of the gel effect is not observed in these conversion vs. time data. This lack of a gel effect in styrene shows that a significant decrease in radical diffusivity does not occur until >90% monomer conversion, when the glass effect is observed, as reactive diffusion of

the radicals is slowed. Thus, the assumption of a well-mixed particle is justified in this study. The simulations discussed here are for a single particle, which is possible because miniemulsion particles are generally decoupled from each other, due to the presence of the costabilizer.

5.2 Rate Constants

For these simulations using styrene, the rate constants for propagation [28], chain transfer to monomer [125], and initiator dissociation [27] are calculated, respectively, according to:

$$k_p = 4.27 \times 10^7 \exp\left(\frac{-32.51}{RT}\right), \quad (49)$$

$$k_{tr,m} = 2.0 \times 10^7 \exp\left(\frac{-56.7}{RT}\right), \quad (50)$$

$$k_d = 1.29 \times 10^{15} \exp\left(\frac{-127.6}{RT}\right), \quad (51)$$

where k_p and $k_{tr,m}$ are in L/mol/s, k_d is in s^{-1} , and the activation energies are in kJ/mol. The macroscopic and molecular rate equations for these events are shown in Table 2, where n and N_I are the number of radicals and initiator molecules in the particle, respectively.

Table 3: Macroscopic and molecular rate constants for styrene at 75 °C and 0% conversion for a particle diameter of 100 nm.

Mechanism	Macroscopic	Units	Molecular	Units
initiator dissociation	9.24×10^{-5}	s^{-1}	9.24×10^{-5}	s^{-1}
propagation	5.65×10^2	L/mol/s	3.65×10^{-4}	s^{-1}
termination	4.21×10^7	L/mol/s	2.67×10^2	s^{-1}
chain transfer to monomer	6.22×10^{-2}	L/mol/s	4.01×10^{-8}	s^{-1}
absorption	–	–	3.07	s^{-1}
desorption	–	–	–	s^{-1}

The rate constants for the reactions that are first-order in radical concentration are scaled down to the molecular level by dividing by the factor $V_p N_A$, where V_p is the particle volume and N_A is Avogadro's number. The molecular rate constant for propagation is calculated as $k_{p,m} = k_p / (V_p N_A)$, and the molecular rate constant for chain transfer to monomer is likewise calculated as $k_{tr,m,m} = k_{tr,m} / (V_p N_A)$. As the number of monomers in the particle decreases, the rates of propagation and chain transfer to monomer decrease. The initial concentration of styrene $[M]_0$ in the particle is determined from the density and molecular weight of styrene monomer. The molecular weight of styrene is 104.15 g/mol, and the density at 75 °C is 855.2 g/L [83], giving an initial monomer concentration of 8.21 mol/L. The molecular initiator dissociation rate constant $k_{d,m}$ is equal to the macroscopic rate constant k_d . The macroscopic and molecular rate constants at 75 °C and a particle diameter of 100 nm are shown in Table 3.

The macroscopic termination reaction is second-order in the concentration of radicals within a particle, as shown in Table 2. The macroscopic termination rate constant is calculated according to:

$$k_t = 1.3 \times 10^9 \exp\left(\frac{-9.92}{RT}\right), \quad (52)$$

where k_t is in L/mol/s and the activation energy is in kJ/mol [71]. The macroscopic termination rate constant at 75 °C is given in Table 3. For the purposes of the KMC simulations, at least two radicals must be present inside a particle for termination to occur. The molecular termination rate is calculated as shown in Table 2, where N_{pairs} is the number of possible radical pairs, and therefore possible termination events, within the particle, and the molecular termination rate constant is

$$k_{t,m} = k_t [R^*], \quad (53)$$

where the value for $[R^*]$ is the concentration of two radicals in a particle, $2 / (V_p N_A)$. Two radicals are equal to 3.32×10^{-24} moles, and assuming a particle diameter of

100 nm gives a particle volume of 5.24×10^{-19} L, so the concentration corresponding to two radicals in a 100 nm particle is 6.34×10^{-6} mol/L. The molecular termination rate constant $k_{t,m}$ is then 267 s^{-1} . If the particle diameter is increased to 170 nm, the concentration for two radicals drops to 1.29×10^{-6} mol/L, giving a molecular termination rate constant of 54.3 s^{-1} . The value of the molecular rate constant $k_{t,m}$ given in Table 3 is for a particle diameter of 100 nm. For styrene, termination occurs by combination of the radicals — not disproportionation — and this will be implied throughout the remainder of the discussion.

Direct calculation of a macroscopic absorption rate constant is not straightforward, so no macroscopic value is given in Table 3, but the molecular value is estimated here. The concentration of styrene in the aqueous phase is calculated to be 0.0566 g sty/100 mL H₂O, based on a fit to literature data [66]. The concentration of styrene in the aqueous phase is then calculated as $(0.0566 \times 10) / MW_{sty} = 5.44 \times 10^{-3}$ mol/L. For styrene, the critical length for radical entry is 2 mers [40], and when using 2,2'-azobis(isobutyronitrile) (AIBN), the initiator radical is close in size to a monomer, so an aqueous-phase radical need only propagate once to reach the critical length for entry. The absorption rate constant, shown in Table 3, is then calculated as $k_{p,m}$ times the aqueous-phase styrene concentration. The molecular absorption rate is calculated as shown in Table 2. However, since AIBN is oil-soluble, it may adsorb even sooner, so this absorption rate is considered to be a lower bound on the actual value. Both this effect and this assumption are investigated and evaluated both in the simulation study and in comparison with the experiments.

From the recipe information for the two experimental data sets used for comparison, the concentrations of AIBN in the particle are 0.127 mol/L for Asua's data set [6] and 6.10×10^{-2} mol/L for the new data set. Using a partition coefficient of 115, the value for AIBN at 50 °C [80], the aqueous phase concentrations of AIBN are, respectively, 1.10×10^{-3} mol/L and 5.30×10^{-4} mol/L. Using a particle diameter of

100 nm for Asua’s data set [6], the number of AIBN molecules per particle is calculated to be 40068. Based on Asua’s recipe information [6], the volume of water per particle is calculated to be 1.45×10^{-18} L, so the number of AIBN molecules in the aqueous phase per particle is 962. The initial rates of dissociation for this system are therefore 3.7 s^{-1} in the particle and $8.9 \times 10^{-2} \text{ s}^{-1}$ in the aqueous phase. Taking the same approach for a particle diameter of 109 nm and the corresponding new recipe, the initial rates of AIBN dissociation are $7.6 \times 10^{-2} \text{ s}^{-1}$ in the particle and $3.2 \times 10^{-3} \text{ s}^{-1}$ in the aqueous phase. Comparison of the aqueous-phase dissociation rate to the absorption rate shows that in both cases absorption is much faster than initiator dissociation, such that generation of aqueous-phase radicals would be the rate-limiting step. For Asua’s recipe [6] using a particle diameter of 170 nm, two radicals in the corresponding aqueous-phase volume of 7.10×10^{-18} L per particle give a radical concentration of $4.67 \times 10^{-7} \text{ mol/L}$. This gives a molecular termination rate of 19.7 s^{-1} , so the termination rate is sufficiently small to neglect termination in the aqueous phase, a common assumption due to the low concentration of radicals in the aqueous phase. While radicals generated in the aqueous phase are allowed to adsorb, the overall fraction of these radicals is much smaller than the number of radicals generated in the particle.

To examine the two competing mechanisms for particle nucleation, the simulation of desorption and absorption events must be carefully considered to require as few assumptions as possible, while ensuring that any remaining assumptions are justified. As previously stated, at the particle diameters considered here, both monomeric and initiator radicals diffuse at high enough rates to encounter the particle surface multiple times before propagating. Desorption may therefore be allowed for both such types of radicals, but it is not allowed for radicals of length greater than one, since these radicals will be either at or beyond the critical chain length for radical entry [40]. Rate constants for radical desorption in the literature generally incorporate the chain

transfer to monomer rate, since many authors assume that monomeric radicals, rather than initiator radicals, are the primary desorbing species [13, 81]. The molecular desorption rate, as shown in Table 2, is only dependent on n , the number of radicals in the particle. Within the KMC model, k_{des} is estimated using multiples of $k_{p,m}N_{m,0}$, to vary the fraction of radicals that desorb, so no value for k_{des} is given in Table 3. For radicals that are generated in the aqueous phase, absorption is the only event allowed in the simulation, where the rate of absorption, as previously explained, is determined by the time to reach the critical chain length for radical entry. Thus, the time for a radical to reach the critical length for entry is dependent on the rate of propagation in the aqueous phase. Except where otherwise noted, absorption of aqueous-phase radicals is excluded from the data shown in this work.

5.3 *Chain-Stopping Mechanisms*

To form an initial hypothesis regarding the nucleation mechanism, a number of possible chain-stopping mechanisms are considered, using the molecular rate constants to predict the molecular weight produced from each chain-stopping event. By comparing these predicted molecular weights to those observed in the experimental data sets, insight is gained into the more plausible chain-stopping mechanisms. These mechanisms are illustrated in Figure 18. Simple termination (i) involves the simultaneous propagation of a pair of radicals, followed by termination between the pair. For termination by initiator dissociation (ii), one dissociation event occurs, which could be followed by desorption of one of the radicals. The remaining radical propagates, until the next dissociation occurs and the growing chain is terminated by a newly generated radical. As more initiator molecules dissociate, the time between dissociations increases, not only making this mechanism less likely, but also increasing the chain lengths for radicals terminated in such a manner. Chain-stopping via chain transfer to monomer (iii) would most likely occur after desorption of one radical of

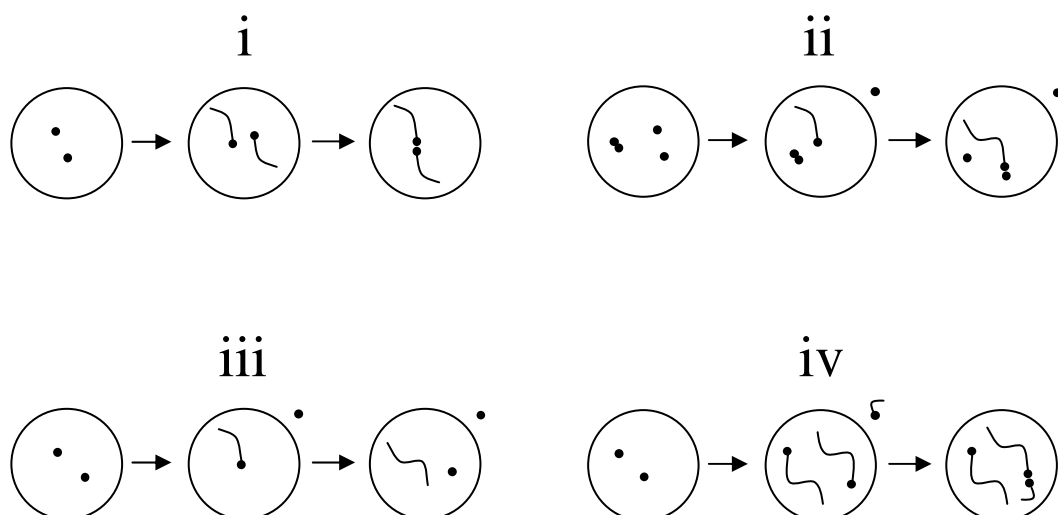


Figure 18: Possible chain-stopping mechanisms: (i) simple termination, (ii) termination by initiator dissociation, (iii) chain transfer to monomer, and (iv) termination by absorption.

a pair, followed by growth of the remaining radical until chain transfer to monomer occurs, producing a dead chain. The length of this chain depends on the ratio of the propagation rate to the chain transfer to monomer rate, $k_p/k_{tr,m}$. For termination by absorption (iv), a radical enters the particle from the aqueous phase and terminates the radical on a live polymer chain. This mechanism is commonly referred to as short-long termination.

For Asua's styrene miniemulsion polymerization at 75 °C, the peak of the molecular weight probability-density distribution is approximately 1.26×10^4 g/mol at 30% particle conversion, giving a chain length of 121 mers. Based on Asua's measurements of particle size [6], comparison to this case will be made using a particle diameter of 170 nm. For mechanism (i), simple termination, the initial degree of polymerization is predicted as $2k_{p,m}N_{m,0}/k_{t,m}$, where $k_{p,m}$ and $k_{t,m}$ are the molecular propagation and termination rates, respectively. This gives a chain length of 171 mers for mechanism (i), which is larger than the experimental chain length of 121 mers, but in the same order of magnitude, so this mechanism cannot be eliminated. To predict the chain length for mechanism (ii), the initial time between initiator dissociations is

used. There are 1.97×10^5 AIBN molecules in a 170-nm particle, so the initial time between dissociations is 5.50×10^{-2} s. Multiplying this time by $k_{p,m}N_{m,0}$ gives an initial estimate for the expected chain length for mechanism (ii) of 255 mers. This is larger than the experimental chain length, but again in the same order of magnitude, so this mechanism also could be significant. For mechanism (iii), the chain length is the ratio $k_{p,m}N_{m,0}/k_{tr,m}$, or 9.09×10^3 mers. This chain length is much higher than the experimental data, so it seems unlikely that mechanism (iii) is significant in the polymerization. Due to this relatively low value of $k_{tr,m}$ compared to the other rates, chain transfer to monomer is usually considered to be insignificant for styrene. For mechanism (iv), the lifetime of the growing radical is determined from the absorption rate, given in Table 3, to be 0.325 s. This gives a chain length for mechanism (iv) of 1.51×10^3 , much higher than that observed experimentally, so mechanism (iv) is unlikely to contribute significantly, unless reabsorption is actually occurring at a substantially higher rate. The two most plausible chain-stopping mechanisms are clearly mechanisms (i) and (ii), although (iv) cannot be ruled out without considering further information on the absorption rate. By comparing the molecular rate of termination with the initial time between initiator dissociations, the observation is made that dissociation occurs faster than termination, so desorption of a radical may not be necessary for mechanism (ii) to occur. Based on these predictions of degree of polymerization, the hypothesis is formed that aqueous-phase radicals are likely insignificant in the miniemulsion polymerization of styrene, and that multiple radicals may coexist inside a particle to propagate chains of a statistically significant length. These arguments will be investigated and quantified using the KMC simulations and experimental data.

5.4 *Experimental Procedure*

To test the hypothesis that aqueous-phase radicals are insignificant in the miniemulsion polymerization of styrene, new experiments were conducted to determine the effect of such radicals on both the rate of conversion and the molecular weight distribution. This confirmation is needed to more conclusively eliminate mechanism (iv), since the rates of radical desorption and adsorption are not well known. The recipes for these experiments are shown in Table 4, and the following standard procedure is used. Styrene and butyl acrylate were purchased from Sigma-Aldrich, and the inhibitors in styrene and butyl acrylate were removed by the inhibitor-remover column, which was obtained from Sigma-Aldrich, before use. Sodium dodecyl sulfate (SDS), potassium persulfate (KPS), AIBN, sodium nitrite (NaNO_2), hydroquinone, and hexadecane were all purchased from Sigma-Aldrich and used as received. The costabilizer, which is hexadecane, and oil-soluble free-radical initiator, which is AIBN, are dissolved in the monomer mix. The surfactant, which is SDS, is dissolved in deionized water. When KPS, the water-soluble initiator, is used, a part of the recipe's total water, 10%, is reserved for preparation of the KPS solution. By dispersing the oil phase into the surfactant aqueous solution with a magnetic stirrer, a coarse emulsion is created, which is then sonicated with an OmniRuptor 250 Ultrasonic Homogenizer for 6 minutes at 20% power output, which is 30 W, to form a miniemulsion. The miniemulsion is then transferred into a standard glass resin kettle equipped with a nitrogen purge, reflux condenser, thermometer and paddle stirrer. Under nitrogen purging to remove oxygen from the miniemulsion and the reactor headspace, the reaction material is heated, using a water bath, to the polymerization temperature, which is 40 °C for KPS initiation and 50 °C for AIBN initiation. For KPS, time zero is the time at which the KPS solution is injected into the reactor. For AIBN, time zero is defined as the time at which the reactor is immersed in the water bath. The polymerization is carried out under nitrogen purging at an impeller speed of 300

rpm. At intervals, samples of the reactor contents are removed by syringe and put in vials containing small quantities of 0.5 wt% hydroquinone solution, which functions to quench the polymerization by scavenging free radicals. Monomer conversion is measured offline by gravimetric analysis of the samples. Following the polymerization experiments, the molecular weight and molecular weight distribution of the samples were measured by gel permeation chromatography (GPC) with a Waters 410 differential refractometer operated at 30 °C. High-performance liquid chromatography–grade chloroform was used as the solvent carrier, at a flow rate of 0.6 ml/min.

Table 4: Recipe information for miniemulsion polymerizations.

	A	B	C	D
Temperature (°C)	50	50	40	40
Water (g)	110	110	110	110
SDS (g)	0.8	0.8	0.8	0.8
Hexadecane (g)	1	1	1	1
NaNO ₂ (g)	–	1.66	–	1.66
Styrene (g)	20	20	–	–
Butyl Acrylate (g)	–	–	25	25
KPS (g)	–	–	0.375	0.375
AIBN (g)	0.228	0.228	–	–

5.5 Experimental Results

In experiments (B) and (D), NaNO₂ was added as an aqueous-phase radical scavenger, to destroy both radicals desorbed from particles and radicals generated in the aqueous phase. The polymerizations using butyl acrylate and KPS were conducted as a control, to show the effectiveness of the NaNO₂ in destroying aqueous-phase radicals. In experiment (B), the ratio of NaNO₂ molecules to AIBN radicals is 8.7, considering that each NaNO₂ molecule can only scavenge one AIBN radical, and each

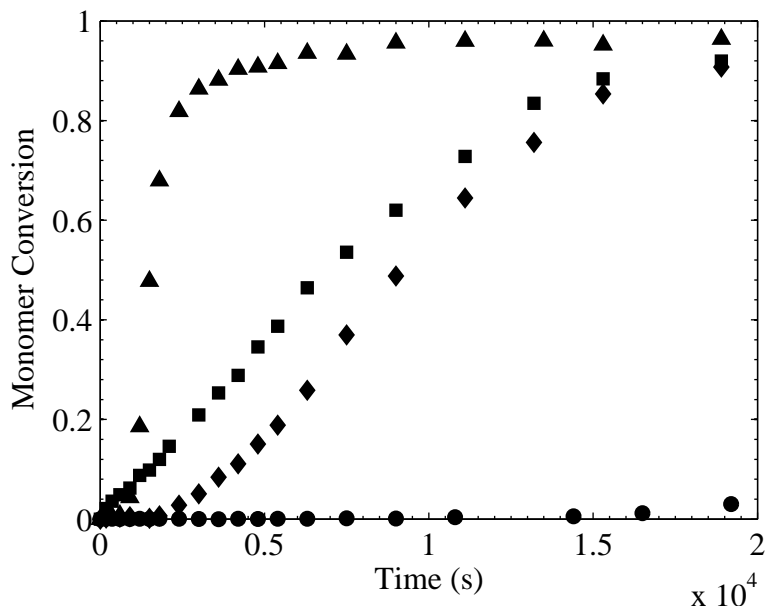


Figure 19: Experimental conversion vs. time for miniemulsions of styrene and AIBN both with (diamond) and without (square) NaNO_2 at 50 °C and for miniemulsions of butyl acrylate and KPS both with (circle) and without (triangle) NaNO_2 at 40 °C.

AIBN molecule produces two radicals. Figure 19 shows that the rate of conversion for styrene using AIBN is similar for the experiments with and without NaNO_2 , indicating that absorption of aqueous-phase radicals is insignificant in the miniemulsion polymerization of styrene. A significantly different conversion rate when using NaNO_2 would indicate that the aqueous-phase radicals contribute to the polymerization, but this is not observed for the two sets of data using styrene in Figure 19. If radicals are present in the aqueous phase due to desorption, then the readsorption of these radicals should be insignificant based on the data in Figure 19. This observation concerning the insignificance of aqueous phase radicals justifies the assumption to neglect aqueous-phase termination, as well as radical adsorption, in the KMC simulations. If these radicals are not significant in the polymerization, then their reactions in the aqueous phase should not significantly affect the polymerization. The initial lag in the conversion curve using NaNO_2 is thought to be due to a small amount of NaNO_2 being present in the particles, where the radical scavenger must be consumed before

propagation can begin. As Figure 19 shows, the polymerization using butyl acrylate and KPS is suppressed almost entirely when using NaNO_2 . The peak of the molecular weight probability-density distribution for experiment (A) is about 5.21×10^5 g/mol, or about 5000 mers, and the particle diameter is measured to be 109 ± 0.4 nm. For experiment (B), the peak molecular weight is about 6.40×10^5 g/mol, or about 6140 mers, and the particle diameter is measured to be 104 ± 0.4 nm. The polydispersity index of the particle size for these experiments is expected to be small, around 1.1 or less.

Considering the peak molecular weight from experiment (A), each of the chain-stopping mechanisms should be examined, to determine which is most consistent with the new data presented in this work. Based on this experimental data and the arguments in Section 3, chain-stopping mechanism (iv) should not be significant for this data, since this requires adsorption of radicals from the aqueous phase. The initial molecular propagation rate for styrene at 50 °C is 1999 s^{-1} per radical, and the molecular termination rate is 158 s^{-1} , for the particle diameter of 109 nm. The predicted molecular weight for mechanism (i), simple termination, is $2k_{p,m}N_{m,0}MW_{sty}/k_{t,m}$, or 2.63×10^3 g/mol, significantly less than the peak molecular weight for experiment (A). From the recipe for experiment (A), the number of AIBN molecules in a 109-nm particle is calculated as 2.49×10^4 molecules. The dissociation rate of AIBN at 50 °C is $3.05 \times 10^{-6} \text{ s}^{-1}$, so the initial time between initiator dissociations, assuming an efficiency of one, is 13.2 s. Thus, the molecular weight predicted for mechanism (ii) is 2.74×10^6 g/mol, and when the efficiency is decreased to a more realistic value of 0.5, the molecular weight doubles to 5.48×10^6 g/mol, much higher than the peak molecular weight for experiment (A). At 50 °C, the chain transfer to monomer rate is 0.115 s^{-1} , so the molecular weight expected for mechanism (iii) is 1.81×10^6 g/mol, closer to the experimental molecular weight than the predictions for both mechanisms (i) and (ii). In other words, chain transfer to monomer should occur for most chains,

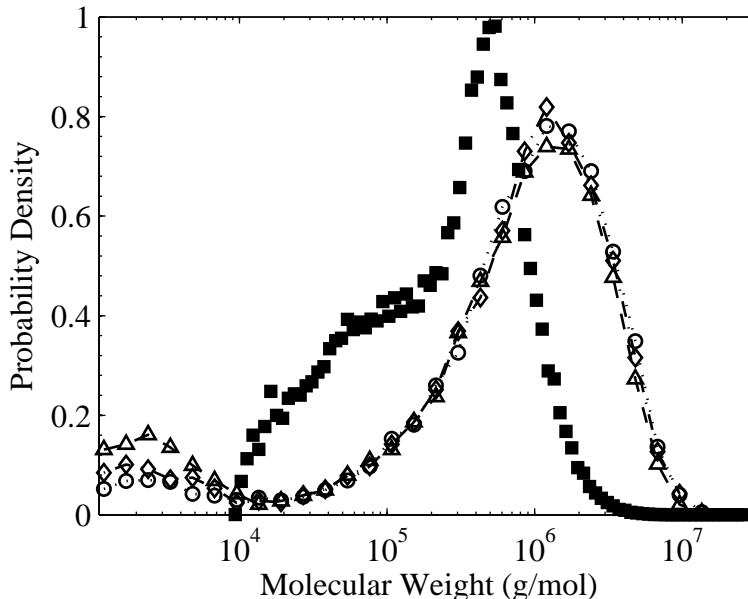


Figure 20: Normalized density of molecular weight distribution from KMC simulations, for a particle diameter of 109 nm at 50 °C and 30% particle conversion, using $k_{t,m} = 158 \text{ s}^{-1}$, $f = 0.6$, and desorption rates of $2.0k_{p,m}N_{m,0}$ (triangle)(dashed line); $3.5k_{p,m}N_{m,0}$ (diamond) (dash-dot line); $5.0k_{p,m}N_{m,0}$ (circle)(dotted line), compared to normalized density of experiment (A) at final conversion of 92%.

prior to dissociation of a new initiator molecule, leading to a molecular weight consistent with experiments (A) and (B). The difference in molecular weight between experiments (A) and (B) is larger than the expected variability between runs, so the residual NaNO_2 seems to have some effect on the molecular weight. Residual NaNO_2 could result in the formation of more single radicals in the particle, thus reducing the effect of mechanism (iii) on the molecular weight, allowing mechanism (ii) to be more significant. The expected dominance of mechanism (iii) implies that radical desorption must be significant, so that mechanism (i) termination will not occur. Chain transfer to monomer should be the dominant chain-stopping mechanism to achieve agreement with the peak molecular weight for experiment (A), with mechanism (ii) possibly playing a secondary role.

5.6 *Simulation Results*

Molecular weight distributions simulated using the conditions of the new experiments are shown in Figure 20 along with the molecular weight data from experiment (A). To calculate each molecular weight distribution, all of the chains of molecular weight greater than 1000 g/mol from 100 individual particle simulations are sorted into bins equally spaced on a log scale, as observed in Figure 20. The weight of the chains in a bin is divided by the weight of all chains included in the distribution, and this weight fraction is then divided by the fractional width of the bin in terms of the true scale, since the bins are equally spaced on a log scale. Chains at lower molecular weights are thus weighted more heavily in the distribution. In the case of the data from experiment (A), the weight fractions are determined from the GPC data, so the weight fractions are already scaled according to the relative bin size on the true scale. The area under the curve is then normalized to one to allow for a better comparison to the experimental data. Given the assumptions of the well-mixed KMC model, the goal is not to achieve perfect agreement between the simulated molecular weight and the experimental molecular weight, but instead to achieve qualitative agreement such as alignment of the peaks of the molecular weight distributions. Simple termination is 10^3 times faster than chain transfer to monomer in a 109-nm particle with two radicals, so single radicals must be present within the particle in order for chain transfer to monomer to dominate the molecular weight. In fact, the secondary peak observed in Figure 20 is near the molecular weight predicted for simple termination, and the height of this secondary peak decreases as the desorption rate is increased, due to the decrease in the number of radical pairs inside the particle. Since, according to the new experiments, adsorption of radicals from the aqueous phase is shown to be insignificant, a single radical must be formed via desorption of the other radical produced by an initiator dissociation in the particle. The peak molecular weights for all of the simulation data in Figure 20 are near 1×10^6 g/mol, which is close to the

predicted molecular weight for mechanism (iii). Minimal variation in the molecular weight peak is observed as the desorption rate is varied, due to the long time between initiator dissociations. The difference in the experimental and simulated molecular weight distributions may be explained by the scatter in the measured chain transfer to monomer rates, which is almost an order of magnitude near the experimental temperature [125]. Also, the experimental and simulated molecular weight distributions shown in Figure 20 are at different conversions, with the experimental molecular weight distribution known only for the final conversion of 92%, while the molecular weight distributions from the simulations are taken at 30% conversion. Due to the dominance of mechanism (iii), the molecular weight peak for the simulation data should broaden toward higher molecular weights as the monomer concentration decreases, but this should not affect the qualitative agreement between the experimental and simulated molecular weight peaks. While the initiator efficiency can also affect the molecular weight distribution, this effect should be minimal if mechanism (iii) is dominant, so the desorption rate is varied at a constant initiator efficiency of 0.6 when comparing the KMC simulations to the new experimental data. Both the initiator efficiency and the desorption rate affect the conversion rate, so these two variables may not be changed independently.

For the molecular weight data from experiment (A) shown in Figure 20, a secondary peak is clearly present in the range from 10^4 to 2×10^5 g/mol, indicating that some chain-stopping mechanism other than mechanism (iii) must have a noticeable effect on the molecular weight distribution. If aqueous-phase radicals are eliminated via the use of NaNO_2 , as in experiment (B), then the secondary peak disappears. Based on these observations, the aqueous-phase radicals do have some impact on the molecular weight distribution, although not on the location of the primary molecular weight peak. To examine the effect of aqueous-phase radicals in further detail, KMC simulations were run with absorption of radicals allowed, where an estimated value

of 1.00 s^{-1} is used for the absorption rate constant, according to the experimental conditions. The primary molecular weight peak for these simulations is at 1.52×10^5 g/mol, a significant shift from the primary peak of 1.81×10^6 g/mol when absorption of radicals is excluded. The molecular weight predicted for mechanism (iv), 2.08×10^5 g/mol, is the closest to the primary peak from the KMC simulations that include absorption, so mechanism (iv) is the most likely source of the secondary peak observed in the data for experiment (A). Mechanism (iii) is still responsible for the primary molecular weight peak in the data from experiment (A).

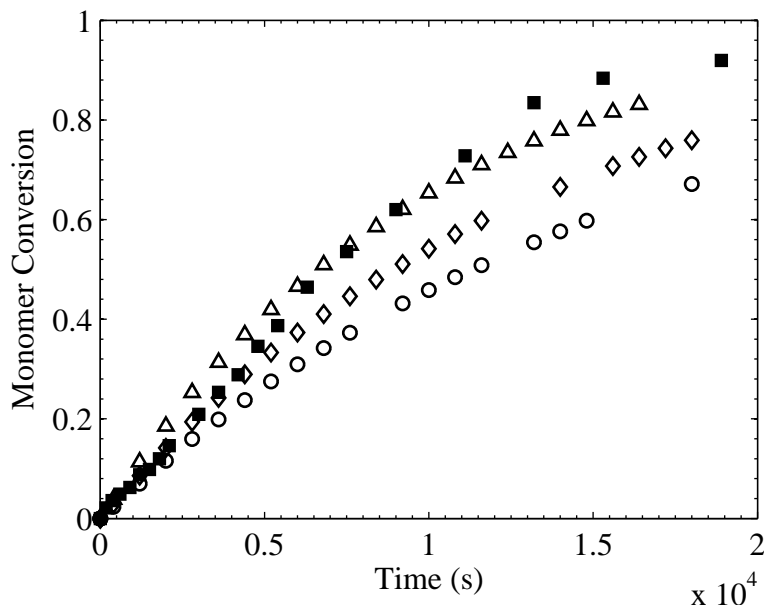


Figure 21: Conversion vs. time from KMC simulations, for a particle diameter of 109 nm at 50 °C, using $k_{t,m} = 158 \text{ s}^{-1}$, $f = 0.6$, and desorption rates of $2.0k_{p,m}N_{m,0}$ (triangle); $3.5k_{p,m}N_{m,0}$ (diamond); $5.0k_{p,m}N_{m,0}$ (circle), with the new data from experiment (A) (square).

When comparing the simulated conversion rate to that of the experimental data, the primary focus is on achieving agreement with the early conversion rate, up to about 30% conversion. The comparisons of the KMC simulations to both the new experimental data and Asua’s are made at particle conversions well below the gel point for styrene, so neither the gel nor the glass effects should be necessary for the simulation to accurately predict the molecular weight distribution at these conversions.

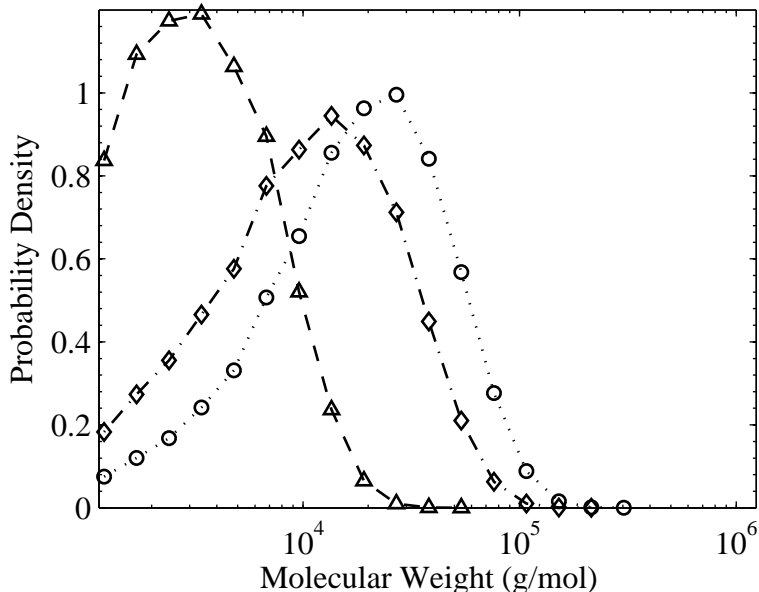


Figure 22: Normalized density of molecular weight distributions from KMC simulations using styrene at 75 °C, at 19% particle conversion and various particle sizes, with zero desorption, $k_p = 5.65 \times 10^2$ L/mol/s, $k_t = 4.21 \times 10^7$ L/mol/s, $k_d = 9.24 \times 10^{-5}$ s $^{-1}$, $f = 0.4$. Particle diameters of 100 nm (triangle)(dashed line); 170 nm (diamond)(dash-dot line); 240 nm (circle)(dotted line).

Figure 21 shows conversion versus time results from the simulations in comparison to the new data from experiment (A). Using a desorption rate around $3.5k_{p,m}$ gives good agreement with the initial conversion rate from experiment (A). Initiator efficiency and desorption rate are somewhat correlated when comparing the simulated and experimental conversion rates. Increasing the desorption rate decreases the rate of conversion, due to the corresponding decrease in the number of radicals in the particle, as radicals are not allowed to re-enter the particle after desorbing. Thus, an increased desorption rate gives the same effect as a decreased initiator efficiency. Conversely, if the initiator efficiency were increased from 0.6, then a desorption rate greater than $3.5k_{p,m}$ would be required to achieve agreement with the early conversion rate.

Simulation results for a particle diameter of 170 nm at a temperature of 75 °C are shown in Figure 22, 23, and 24, where each data set is an average of 100 single

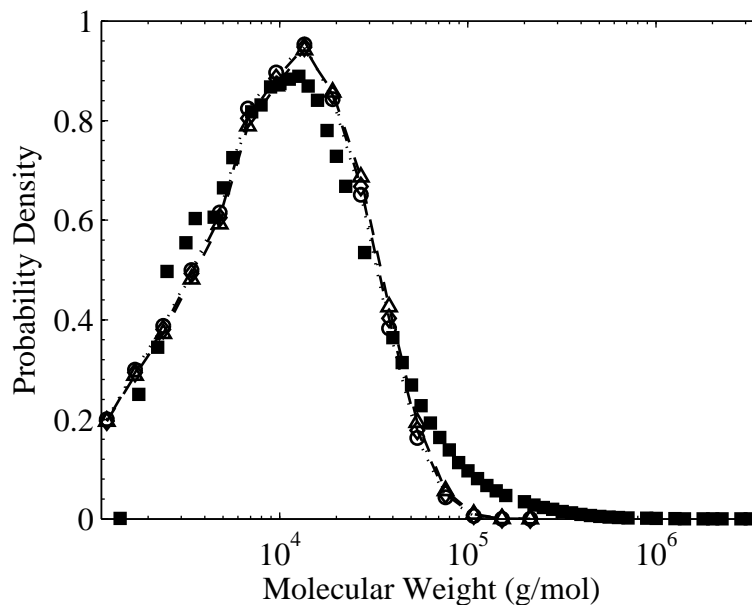


Figure 23: Normalized density of molecular weight distributions from KMC simulations using styrene at 75 °C, at 30% particle conversion and a particle diameter of 170 nm, with $k_{t,m} = 54.3 \text{ s}^{-1}$ and initiator efficiencies of 0.45 (triangle)(dashed line); 0.6 (diamond)(dash-dot line); 0.75 (circle)(dotted line), with Asua's molecular weight distribution [6] at 30% conversion (square).

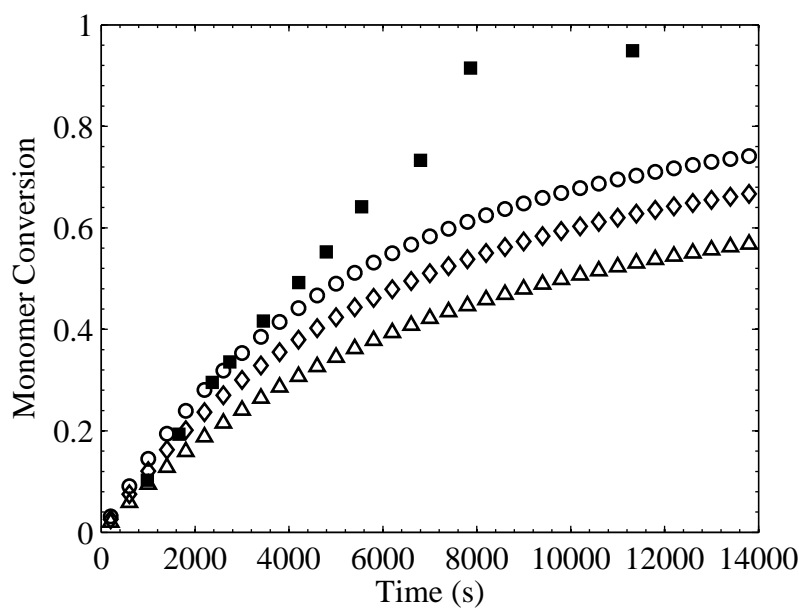


Figure 24: Conversion vs. time from KMC simulations using styrene at 75 °C and a particle diameter of 170 nm, with $k_{t,m} = 54.3 \text{ s}^{-1}$ and initiator efficiencies of 0.45 (triangle); 0.6 (diamond) ; 0.75 (circle), with Asua's conversion vs. time data [6] (square).

particle simulations. This temperature is used to correspond to Asua’s experimental conditions [6]. The particle size distribution for Asua’s data [6] encompasses a significant range of particle sizes. While most of the particles at 30% conversion, where the simulated molecular weight distributions are compared, have diameters of 100–200 nm, a small fraction of the particles may have a diameter greater than 1000 nm [6]. At higher conversion the particle size distribution is even broader, so the molecular weight distributions are compared at 30% conversion, or 19% conversion for Figure 22. The initiator efficiency of 0.6 used in Figure 22 is chosen due to the agreement it produces with Asua’s experimental data [6] for both the peak molecular weight in Figure 23 and the early conversion rate in Figure 24. The data shown in Figure 22 illustrate the importance of particle size on the molecular weight distribution, since a single pair of radicals will take longer to terminate in a larger particle. Increasing the particle diameter from 100 to 170 nm produces nearly an order-of-magnitude increase in the peak molecular weight. The predicted molecular weight for chain-stopping mechanism (i), simple termination, is $2k_{p,m}N_{m,0}MW_{sty}/k_{t,m}$, which is 3.6×10^3 g/mol for a particle diameter of 100 nm, and 1.8×10^4 g/mol for a particle diameter of 170 nm. Both of these molecular weights are consistent with the simulated molecular weight peaks in Figure 22. For the particle diameter of 240 nm, mechanism (i) predicts a molecular weight of 5.0×10^4 g/mol, while mechanism (ii) predicts a molecular weight of 2.4×10^4 g/mol. Figure 22 shows that the molecular weight peak for the 240-nm particle is between the molecular weights predicted by mechanisms (i) and (ii), so the molecular weight distribution shown in Figure 22 appears to be an average of these two mechanisms. For the 170-nm particle, mechanism (ii) predicts a molecular weight of 6.7×10^4 g/mol, so the molecular weight predicted by mechanism (i) for the 170-nm particle is likely more significant for the peak molecular weight shown in Figure 22 for this particle size, although mechanism (ii) may also contribute to the molecular weight. For the 100-nm particle, mechanism (ii) predicts a molecular

weight of 3.3×10^5 g/mol, much higher than that predicted for this particle size by mechanism (i). Although the molecular weight predicted by mechanism (ii) is higher than the secondary peak for the 100-nm particle in Figure 22, mechanism (ii) may be partly responsible for producing this peak, due to the stochastic nature of the simulations. The molecular weight predicted by mechanism (iii), chain transfer to monomer, is 9.46×10^5 g/mol, considerably higher than all of the peaks observed in Figure 22, so mechanism (iii) should not contribute significantly to any of these molecular weight peaks. As particle size increases, the contribution of simple termination to the peak molecular weight decreases, so while simple termination is clearly dominant for a particle diameter of 100 nm, it is not the only significant mechanism for a particle diameter of 170 nm. Increasing the particle size shortens the time between initiator dissociations, so mechanisms (i) and (ii) are equally significant for the 240-nm particle. Initiator efficiency has a small effect on the molecular weight as long as mechanism (i) is dominant. A particle diameter of 170 nm is chosen for Figure 23 and 24 because this gives a value for $k_{t,m}$ of 54.3 s^{-1} , allowing the peak of the simulated molecular weight distribution to agree with the peak of Asua's molecular weight distribution [6], as shown in Figure 23.

In Figure 24, the rate of conversion is shown to increase with initiator efficiency. As effective radicals are produced at a faster rate, the observed rate of polymerization increases. Figure 23 shows that the molecular weight distribution remains nearly unchanged as the initiator efficiency is increased, indicating the dominance of mechanism (i). As effective radicals are produced at a faster rate, mechanism (ii) becomes more dominant compared to mechanism (i), but this effect is reduced at smaller particle sizes due to the smaller amount of initiator initially present. In both Figure 23 and 24, using an initiator efficiency of 0.6 and no desorption provides good agreement with Asua's experimental data, for both early conversion rate and molecular weight. Due to the significant coarsening of the particle size after 30% conversion, achieving

agreement with Asua's experimental data is not attempted beyond $\sim 30\%$ conversion. Initiator efficiency has a significant effect on the rate of conversion, but its effect on the molecular weight is much smaller, provided that mechanism (i) is dominant. Since Figure 23 shows that molecular weight is only slightly affected by changes in initiator efficiency, the conclusion is that mechanism (i) is dominant for the chosen particle diameter of 170 nm. Next, the effects of radical desorption in the KMC simulation are examined in comparison to Asua's experimental data.

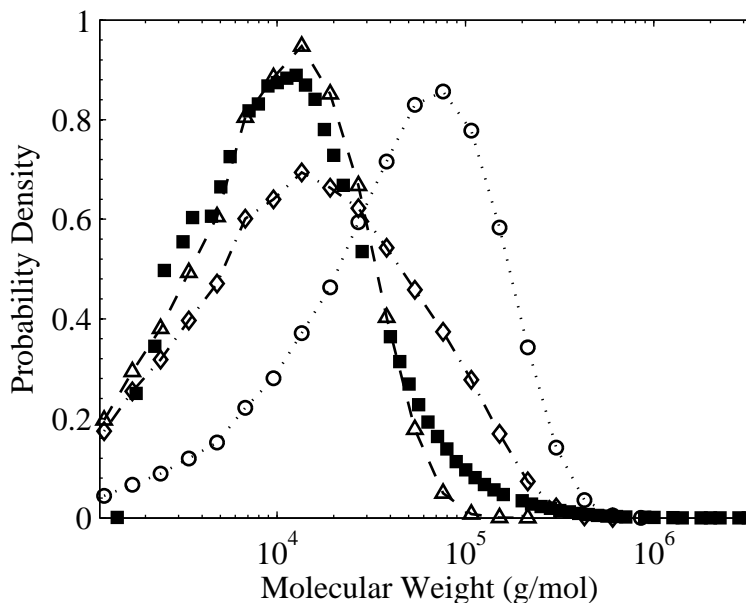


Figure 25: Normalized density of molecular weight distributions from KMC simulations using styrene at 75 °C, at 30% particle conversion and a particle diameter of 170 nm, with $k_{t,m} = 54.3 \text{ s}^{-1}$, $f = 0.6$, and desorption rates of 0.0 (triangle)(dashed line); $0.05k_{p,m}N_{m,0}$ (diamond)(dash-dot line); $3.0k_{p,m}N_{m,0}$ (circle)(dotted line), with Asua's molecular weight distribution data [6] at 30% conversion (square).

Figure 25 and 26 show that a negligible amount of desorption is allowable in order to attain the same early rate of conversion as observed in Asua's experimental data. When desorption is allowed to occur, single radicals formed in the particle grow unchecked until the next initiator dissociation. This produces an increase in the peak molecular weight, as well as an increase in the conversion rate. In comparing the

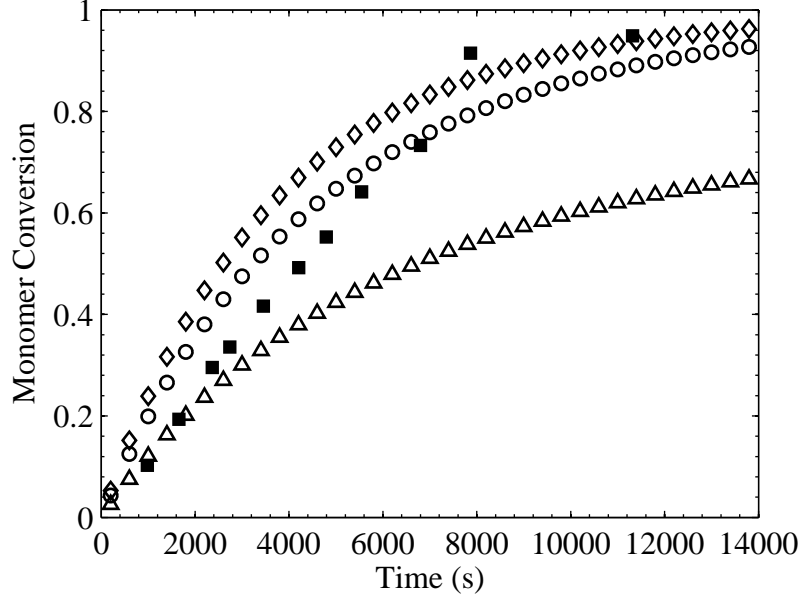


Figure 26: Conversion vs. time from KMC simulations using styrene at 75 °C and a particle diameter of 170 nm, with $k_{t,m} = 54.3 \text{ s}^{-1}$, $f = 0.6$, and desorption rates of 0.0 (triangle); $0.05k_{p,m}N_{m,0}$ (diamond); $3.0k_{p,m}N_{m,0}$ (circle), with Asua's conversion vs. time data [6] (square).

simulations at Asua's experimental conditions to those at the conditions of the new experiments, the two experiments appear to be in different regimes. Simple termination appears to dominate the molecular weight in Asua's experiments, while chain transfer to monomer is shown to dominate the molecular weight in the new experiments. This difference is due to an apparent lack of radical desorption suggested by Asua's experimental data. If desorption does occur in Asua's experimental data, it must be followed quickly by readsorption, with no tangible effect on the polymerization. The probability of a radical escaping the particle before propagating, as required by the KMC model, is affected by both the temperature and the particle size. Since the propagation rate scales faster with temperature than does the diffusivity, the probability of a radical escaping a particle of equal volume should decrease as the temperature increases. Using the previously described method for calculating styrene diffusivity, a monomer diffusivity of $2.81 \times 10^{-5} \text{ cm}^2/\text{s}$ is obtained at 50 °C. The increase in the probability of propagation prior to desorption when increasing the temperature

from 50 to 75 °C is calculated as $(k_{p,m,75^\circ C}N_{m,0}/D_{75^\circ C}) / (k_{p,m,50^\circ C}N_{m,0}/D_{50^\circ C})$, which is $(4641/3.77 \times 10^{-5}) / (1999/2.81 \times 10^{-5}) = 1.73$. Thus, a radical is nearly twice as likely to propagate before desorption when the temperature is increased from 50 to 75 °C. The increase in particle diameter, using a 170-nm particle to compare to Asua’s data and a 109-nm particle for the new data, is by a factor of 1.6, so the combined effect of the propagation rate and particle size shows that a radical should be 3.5 times less likely to desorb from a particle using Asua’s experimental data compared to the new data. Other effects not considered, such as interactions of radicals with the surfactant on the particle surface, may increase with temperature and further reduce the rate of radical desorption or result in fast readsorption.

5.7 Conclusions

Both the experimental and simulation results presented here support the hypothesis that absorption of aqueous-phase radicals is insignificant in the miniemulsion polymerization of styrene, whether such radicals desorb from particles or are generated in the aqueous phase. This conclusion does not wholly contradict the work of Nomura [81], since he examined nucleation in both micro- and macroemulsion polymerization, where nucleation primarily occurs in the smaller micelles. The results of the KMC simulations compared to the new experimental data show that chain transfer to monomer, mechanism (iii), is dominant for this new set of experimental conditions and the corresponding particle diameter. The results of the KMC simulations compared to the data of Alduncin and Asua [6], along with the molecular weights predicted for mechanisms (i) and (ii), show that simple termination, mechanism (i), is dominant at their experimental conditions, with mechanism (ii) also playing a role. Desorption of radicals is affected by both temperature and particle size, increasing with both decreased temperature and decreased particle size. This conclusion substantiates the central idea of Asua’s theory of particle nucleation, under certain

experimental conditions, although chain transfer to monomer is shown here to be unnecessary for radical desorption. Based on this modeling work, it appears that no single mechanism is always dominant in miniemulsions, but that the interplay between mechanisms is significant, and that the significance of each depends on the details of the recipe. The theories of neither Asua nor Nomura are entirely sufficient to describe the varied nucleation mechanisms which may dominate over a range of reaction conditions and particle sizes, as neither of their theories allow for the dominance of simple termination. The KMC simulation of miniemulsion particles is shown to be an effective method for examining the mechanisms involved in particle nucleation using oil-soluble initiators, as it makes no presuppositions about the significance of any potential nucleation mechanism. Unlike most previously used modeling approaches for miniemulsions, it considers stochastic effects due to the small numbers of species in a particle, and it enables the prediction of conversion and molecular weight distribution.

CHAPTER VI

EXAMINATION OF THE BRANCH-LENGTH DISTRIBUTION IN BUTYL ACRYLATE USING THE RATE-EQUATION MODEL

The study presented in this chapter [100] applies the rate-equation model to examine branch length in butyl acrylate solution polymerization, comparing the model results to experimental data from Nikitin et al. [79] Intramolecular chain transfer to polymer, otherwise known as backbiting, is commonly assumed to produce only short-chain branches, while intermolecular chain transfer to polymer is assumed to produce all long-chain branches. Although the branches generated by backbiting, according to its traditional definition, are thought to be two mers in length, the definition of short-chain versus long-chain branches is somewhat ambiguous. A cumulative distribution function (CDF) of branch lengths produced through backbiting has been created using spatially-resolved simulations of individual polymer chains on a face-centered cubic (FCC) lattice, covering a large range of possible chain conformations that could result in a radical coming in contact with mers at varying distances from the radical chain-end. This backbiting CDF is applied in the rate-equation model, in conjunction with intermolecular chain transfer to polymer, to predict the branch-length distribution for the experimental data [79], and to examine the source of long-chain branching in butyl acrylate. Predictions are also made for the effects of short-chain and long-chain branching on the intrinsic viscosity. The purpose of this study is not to construct a model that agrees with experimental results, but rather to formulate a model capable of predicting branch length.

6.1 Rate Constants

The rate constants used in the rate-equation model are taken primarily from the same source as the experimental data [79], so the techniques used to determine each rate constant should be independently examined to account for any significant assumptions contained within the rate constants when interpreting the results of the rate-equation simulations. The propagation rate k_p for butyl acrylate has been measured via pulsed-laser polymerization/size-exclusion chromatography (PLP/SEC), and the value used here [12], given in Table 5, combines PLP/SEC data from multiple authors. Low reactivity of mid-chain radicals had previously limited the PLP/SEC technique to temperatures of 20 °C or less [12], where the backbiting rate is sufficiently low, meaning that the value of k_p at higher temperatures had to be extrapolated. Recent advances in laser frequency allowed measurement of k_p up to 70 °C, confirming that this extrapolation is accurate [18].

Table 5: Macroscopic rate constants for butyl acrylate at 70 °C, taken primarily from Nikitin et al. [79]

Rate Constant	Macroscopic Value	Units	Reference
k_p	4.16×10^4	L/mol/s	[12]
$k_{tr,m}$	3.16	L/mol/s	[70]
$k_{tr,s}$	35.1	L/mol/s	[79]
$k_{tr,p}$	0.151	L/mol/s	[9]
k_{bb}^*	880	s ⁻¹	[79]
k_d	2.36×10^{-4}	s ⁻¹	[3]
$k_{p,mcr}$	53.1	L/mol/s	[55]
$k_{tr,m,mcr}$	1.92×10^{-2}	L/mol/s	[70]
k_t	1.88×10^8	L/mol/s	[19, 78]
$k_{t,h}$	3.85×10^7	L/mol/s	[19, 78]
$k_{t,mcr}$	2.53×10^6	L/mol/s	[19, 78]

The rate constant for chain transfer to monomer, $k_{tr,m}$, was measured by Maeder and Gilbert [70] using the molecular weight distribution from a seeded emulsion polymerization. This system approximates zero-one kinetics, where no more than one radical at a time is present in a polymer particle, thus minimizing termination and ensuring that chain transfer to monomer dominates the number-average molecular weight [70]. The rate constant for chain transfer to solvent, $k_{tr,s}$, is calculated from the ratio $C_{tr,s} = k_{tr,s}/k_p$, for which Nikitin et al. determined a pre-exponential factor of 10.5 (unitless) and an activation energy of 26.9 kJ/mol. The Arrhenius fit was performed using values of $C_{tr,s}$ at 50, 60, and 70 °C which were calculated by assuming that chain transfer to solvent is the dominant chain-stopping event and accounting for termination and chain transfer to monomer [79]. Intermolecular chain transfer to polymer is not accounted for in the calculation of $C_{tr,s}$ because its contribution to the number-average molecular weight had already been shown to be less than 1% for the experiments performed by Nikitin et al. [79] The experimental conditions for the rate-equation model, corresponding to the data set used for comparison from Nikitin et al. [79], are given in Table 6.

Table 6: Initial conditions for rate-equation model [79].

Parameter	Value	Units
T	70	°C
$[M]_0$	1.63	mol/L
$[S]_0$	5.82	mol/L
$[I]_0$	2.1×10^{-2}	mol/L

The backbiting rate constant in the rate-equation model is computed as:

$$k_{bb} = R_{bb} \left(\frac{\mu_n}{2} \right) \quad (54)$$

where $R_{bb} \left(\frac{\mu_n}{2} \right)$ is the cumulative backbiting rate taken at half the number-average chain length. The factor of two is included because the backbiting rate constant

should only incorporate the length of live chains, as dead chains are included in μ_n but cannot backbite, and the average length of a live chain is half its dead length. $R_{bb}(\frac{93}{2}) = 880 \text{ s}^{-1}$, as taken from experimental data [79], so the backbiting CDF is converted into a backbiting rate distribution according to this value.

Mid-chain radicals produced by backbiting and intermolecular chain transfer to polymer are modeled separately in order to examine the amount of branching resulting from each type of mid-chain radical. The rate constant for intermolecular chain transfer to polymer, $k_{tr,p}$, is difficult to measure experimentally, so the value of this rate constant is commonly estimated [9, 79, 92]. For the study presented here, the value used for $k_{tr,p}$ is estimated [9] through the combination of rate constants obtained from (1) a model optimization around experimental data for a seeded, semicontinuous emulsion polymerization of butyl acrylate [92] and (2) the simulation of PLP/SEC for butyl acrylate [10]. The rate constant used for propagation of mid-chain radicals, $k_{p,mcr}$, has been determined by Nikitin et al. [78] through a series of PLP/SEC experiments, where the pulse repetition rate of the laser is varied, thereby varying the apparent propagation rate constant, which is a combination of the propagation rates of secondary and mid-chain radicals. An average propagation rate constant for butyl acrylate, irrespective of the PLP/SEC experiments, is determined through simulations using an iterative algorithm. The value of $k_{p,mcr}$ is then determined from the difference between the average and apparent propagation rate constants [78].

The rate constant for chain transfer to monomer for mid-chain radicals, $k_{tr,m,mcr}$, is taken to be the rate constant for chain transfer to monomer in methyl methacrylate [9, 79]. Having an extra methyl group attached to a vinyl carbon, methyl methacrylate is a more sterically hindered molecule than butyl acrylate, so the rate constant for methyl methacrylate is used as an approximation for the rate constant of a mid-chain radical in butyl acrylate, which is more sterically hindered than a secondary radical in butyl acrylate. The chain transfer ratio $k_{tr,m}/k_p$ for methyl methacrylate

was determined from molecular weight distributions [110] and converted to the rate constant for chain transfer to monomer [70] using a propagation rate constant for methyl methacrylate obtained by an IUPAC Working Party [20].

The same activation energy of 5.6 kJ/mol is used for k_t , $k_{t,h}$, and $k_{t,mcr}$ [78, 79], where the activation energy was determined through single-pulse PLP experiments in combination with near-infrared spectroscopy [19] to obtain a monomer conversion profile and chain transfer to monomer was assumed to be negligible, thus giving the ratio k_t/k_p . The pre-exponential factors for the rate constants were obtained by fitting a steady-state model to literature data for solution polymerization of butyl acrylate at low conversion [77, 78].

6.2 Comparison to Experimental Data

Before making predictions about the amounts of long-chain and short-chain branching, the model is first compared against the experimental data [79]. Nikitin et al. validated this set of rate constants against their data for μ_n and degree of branching, but not against their data for monomer conversion [79]. With the exception of the initiator efficiency, all of the parameters and rate constants used in this study were taken directly from published sources.

A typical value is used for initiator efficiency, $f = 0.4$, and the results are shown in Figure 27. The monomer conversion predicted by the rate-equation model is in good agreement with the experimental data [79] up to 75% conversion. The number-average molecular weight predicted by the model is shown in Figure 28, passing relatively close to the experimental data point [79]. The number-average molecular weight predicted by the steady-state model of Nikitin et al. [79], which is based on the instantaneous monomer conversion, is in agreement with the prediction of the rate-equation model. Chain transfer to solvent, shown in Equation (17), dominates the molecular weight. The rate of chain transfer to solvent is essentially constant

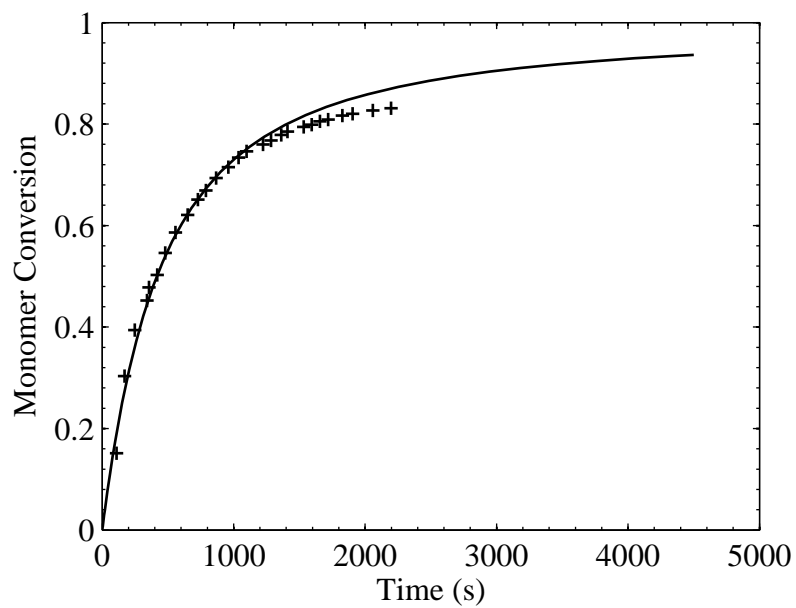


Figure 27: Monomer conversion from rate-equation simulation compared to the experimental data from Nikitin et al. (+) [79].

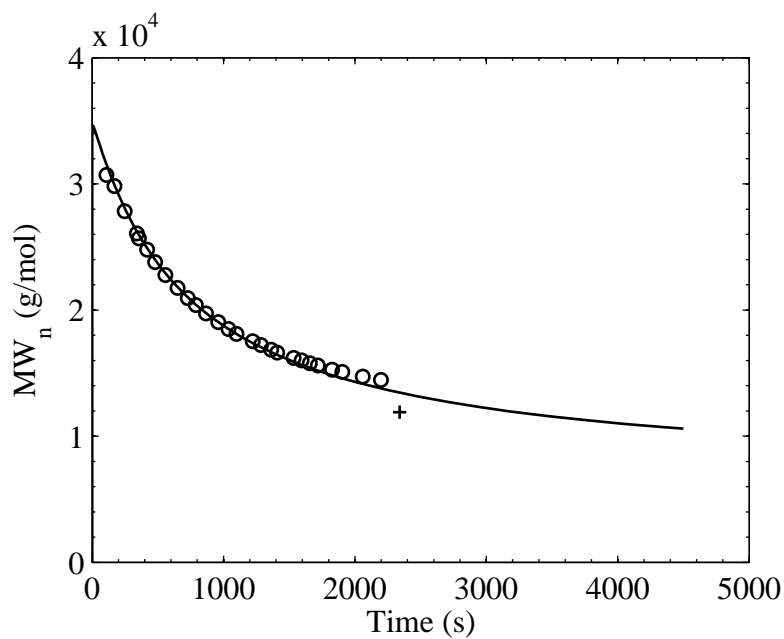


Figure 28: Number-average molecular weight from rate-equation simulation (line) and steady-state model of Nikitin et al. (circle) [79] compared to experimental data point from Nikitin et al. (+).

throughout the polymerization, so the number-average molecular weight decreases along with the rate of polymerization. For mid-chain radicals, chain transfer to solvent is neglected, as Nikitin et al. [79] did not report a value for this rate constant, but if the value of $k_{tr,s,mcr}$ were estimated as $k_{tr,s,mcr} = k_{tr,s}(k_{tr,m,mcr}/k_{tr,m})$, then the number-average molecular weight would be reduced by up to 17% at the end of the simulation. Since this model uses only rate constants reported in the literature to make a comparison to the experimental data of Nikitin et al. [79], the estimation of any rate constants should be avoided, and thus $k_{tr,s,mcr}$ is set to zero.

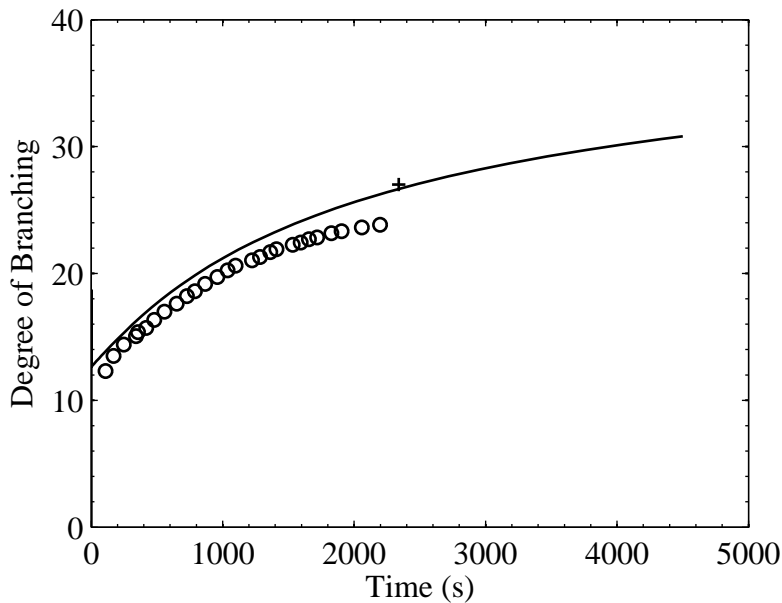


Figure 29: Degree of branching from rate-equation simulation (line) and steady-state model of Nikitin et al. (circle) [79] compared to experimental data point from Nikitin et al. (+).

As a final comparison to the experimental data, Figure 29 shows the degree of branching, or branches per 1000 mers, predicted by the rate-equation model. Initially, the average chain length is about 270 mers, well above the highest branch cutoff length of $L_{cut} = 40$ mers. By the end of the simulation, the average chain length is near 80 mers, so at $L_{cut} = 40$ mers no long-chain branches are formed via backbiting. The results from the the rate-equation model shown in Figure 29 only

include branches formed by propagation of mid-chain radicals, as calculated in Equation (39) and (40). The predicted degree of branching from the steady-state model of Nikitin et al. [79] follows a trend similar to that of the rate-equation model, but the predictions from their model are somewhat lower. Measuring the concentration of quaternary, or branched, carbons using nuclear magnetic resonance (NMR) spectroscopy [4, 79] provides clear evidence of the structures generated through mid-chain radical propagation, but shows no discernable peaks [68] that would correspond to the structures generated through termination of mid-chain radicals, shown in Equation (23) and (24). The NMR signatures indicative of mid-chain radical termination may lie within larger peaks, but due to the low probability of mid-chain radical termination combined with the experimental error, no definite conclusion can be reached [68]. The model prediction is close to the experimental data point [79] for degree of branching. Using the nominal rate constants, the model agrees reasonably with all of the experimental measurements used for comparison [79]. If the estimated value of $k_{tr,s,mcr}$ were used in the model, the final branch content as shown in Figure 29 would be reduced by as much as 11%. As chain transfer to solvent of a mid-chain radical prevents a branch from being formed, the total amount of branching would be reduced, but the relative amounts of branching resulting from backbiting and intermolecular chain transfer, as well as the relative amounts of short-chain and long-chain branching, would remain unchanged.

6.3 Branching Predictions

Figure 30(a) and 30(b) show the total concentration of branch points produced by backbiting and intermolecular chain transfer to polymer, including branches that formed by termination of mid-chain radicals. As has been shown by previous authors, backbiting is responsible for the overwhelming majority of branch points, by a factor of about 10^4 in this case, particularly when the monomer concentration is low [4], as

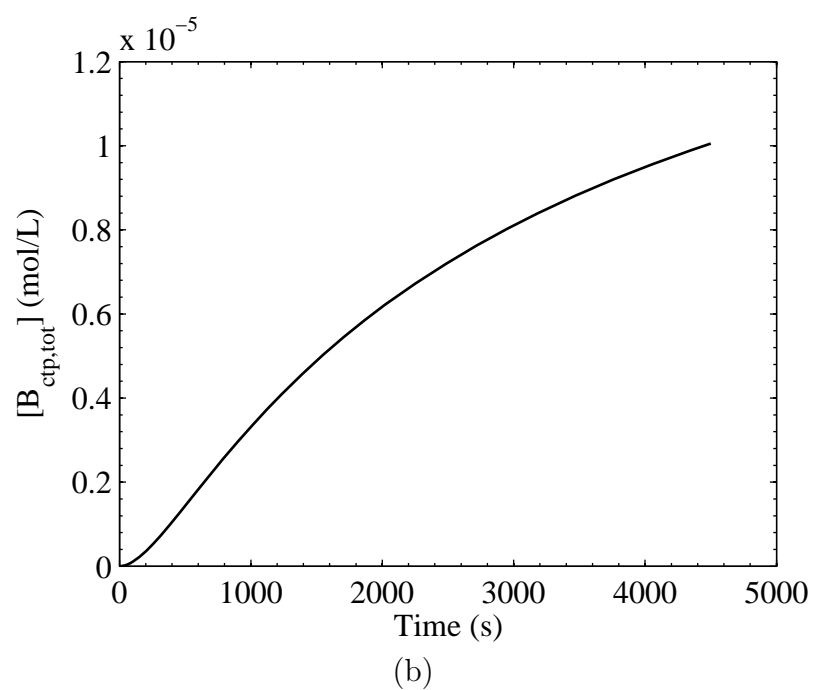
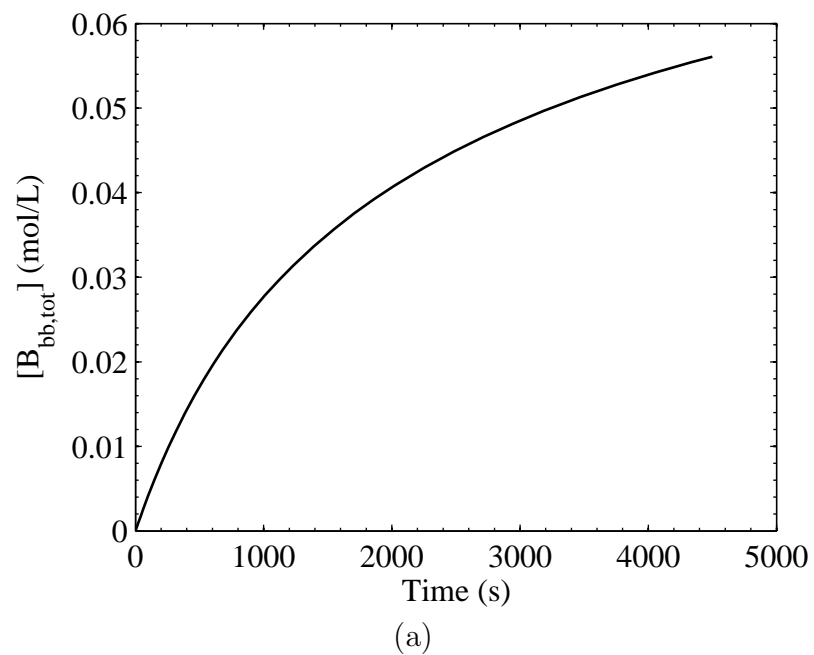


Figure 30: Concentration of branches produced by (a) backbiting and (b) intermolecular chain transfer to polymer, including branches produced by termination of mid-chain radicals.

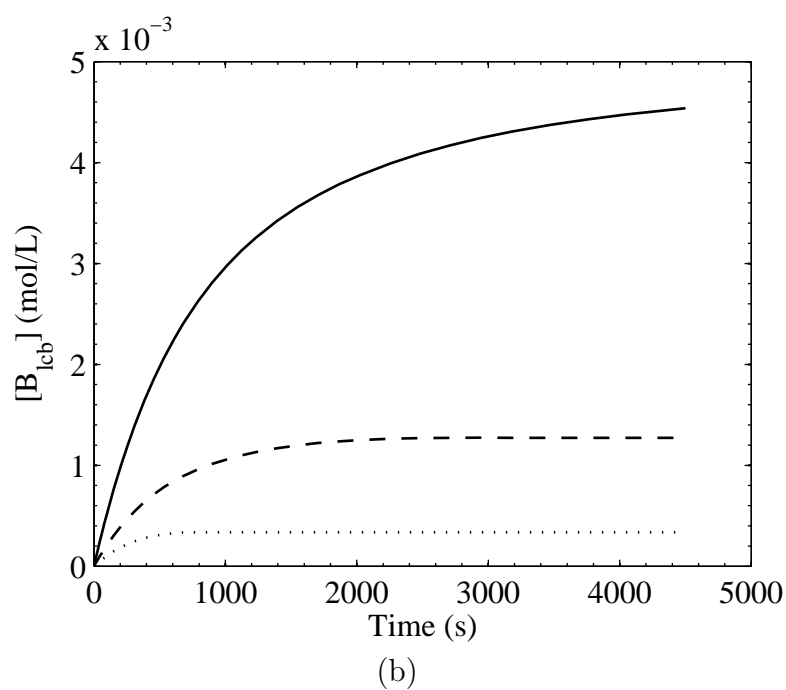
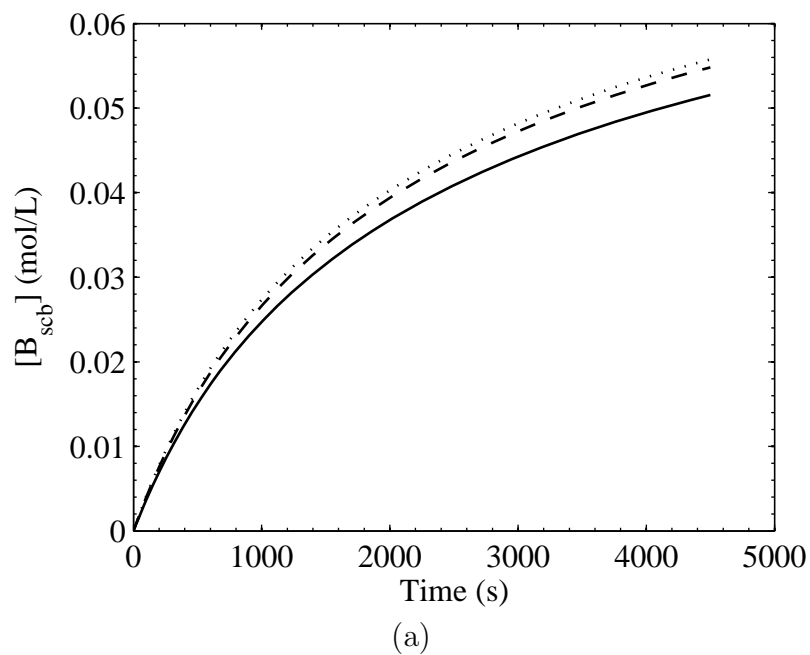


Figure 31: Concentration of (a) short-chain and (b) long-chain branches at $L_{cut} = 10$ (solid line), $L_{cut} = 25$ (dashed line), and $L_{cut} = 40$ (dotted line), including branches produced by termination of mid-chain radicals.

it is in Nikitin’s solution polymerizations [79]. The value of k_{bb}^* given in Table 5 was determined under the assumption that intermolecular chain transfer to polymer is insignificant for this system [79], and the model results show that this assumption is consistent. In order to form a branch, a mid-chain radical must react through either propagation or termination. For this simulation of solution polymerization, 84% of the final branch content results from propagation of mid-chain radicals. The rest of the branches are formed through termination reactions of mid-chain radicals, as shown in Equation (23) and (24). In both Figure 30(a) and 30(b), the rate of branch formation decreases with time due to the depletion of monomer, in contrast to systems with higher solids concentrations, where branching from intermolecular chain transfer to polymer becomes significant as the polymer concentration increases. Figure 31(a) and 31(b) show the concentration of short-chain and long-chain branches, respectively, using cutoff lengths of 10, 25, and 40 mers. Using cutoff lengths of 25 and 40 mers, the concentration of long-chain branches plateaus, as observed in Figure 31(b), when $\frac{\mu_n}{4} < L_{cut}$, since an average chain length of $\frac{\mu_n}{2}$ is used to determine the backbiting rate constant, and long-chain branches cannot be formed if the average chain length is less than $2L_{cut}$. At a cutoff length of 10 mers, the concentration of long-chain branches is about 8% of the total branch concentration, but is about 500 times the concentration of branches produced by intermolecular chain transfer to polymer. Even when the cutoff length is increased to 40 mers, the amount of long-chain branching is 30 times the concentration of branches produced by intermolecular chain transfer to polymer, indicating that backbiting is dominant in the formation of long-chain branches, at least for this system. This result shows that the general assumption of intermolecular chain transfer to polymer being exclusively responsible for long-chain branching does not necessarily hold true for solution polymerizations.

To examine the significance of this finding that backbiting is overwhelmingly dominant in branch formation, the concentration of polymer repeat units determined by

the rate-equation model should be compared to a critical concentration where chains are expected to overlap each other in solution. Below this critical concentration of polymer, backbiting is expected to dominate, as the coiled polymer chains do not overlap each other. The probability of intermolecular chain transfer to polymer increases with the concentration of polymer repeat units. This critical concentration of polymer repeat units is assumed to be equal to the concentration of repeat units within a single coiled chain, which is calculated as [4]

$$c^* = \frac{0.88}{N_A MW_n^{1/2}} \left(\frac{MW_{BA}}{\alpha^2 l^2 C_\infty} \right)^{3/2} \quad (55)$$

where MW_{BA} is the molecular weight of butyl acrylate, 128.17 g/mol, α is the coil expansion factor, l is the carbon-carbon bond length, and C_∞ is the characteristic ratio. The parameter values used by Ahmad et al. [4] are $\alpha = 1.25$, $l = 0.154$ nm, and $C_\infty = 8$. The values of both α and C_∞ are estimates [4], but c^* is much more sensitive to the value of α , so only the value of α will be examined in detail. In a theta solvent, $\alpha = 1$ [21], but the solution polymerization of butyl acrylate examined in this work was carried out in a mixture of xylene isomers, which are known to be good solvents for butyl acrylate [85]. A coiled polymer chain is more expanded in a good solvent, so α would be greater than one for the system considered in this work. For butyl methacrylate in aromatic solvents such as benzene and toluene, values of α determined through light-scattering and viscosity measurements range from 1.28 to 1.48, for number-average molecular weights ranging from 1.1×10^5 to 4.7×10^5 g/mol, at 25 °C [118, 119]. α increases with both molecular weight and temperature. Although the number-average molecular weight predicted by the rate-equation model is a factor of 10 less than the experimental molecular weights corresponding to the α values, the temperature for the butyl acrylate solution polymerization simulated by the rate-equation model is 70 °C, so these factors should balance each other somewhat, meaning that $\alpha = 1.25$ should be a reasonable estimate.

Figure 32 shows that the concentration of polymer repeat units predicted by the

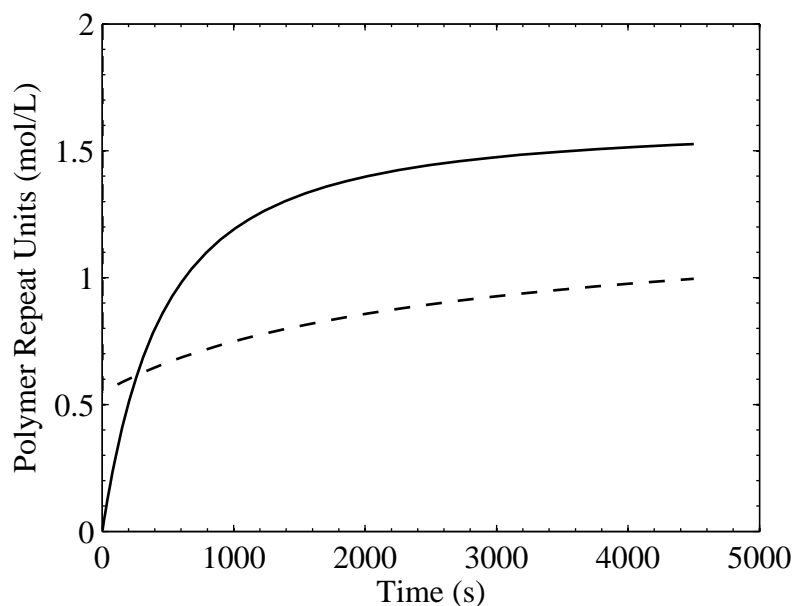
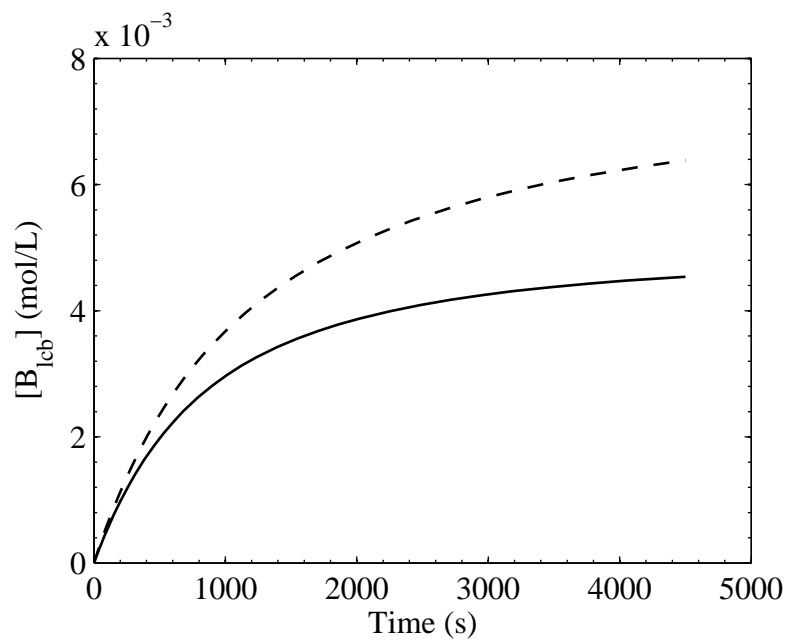


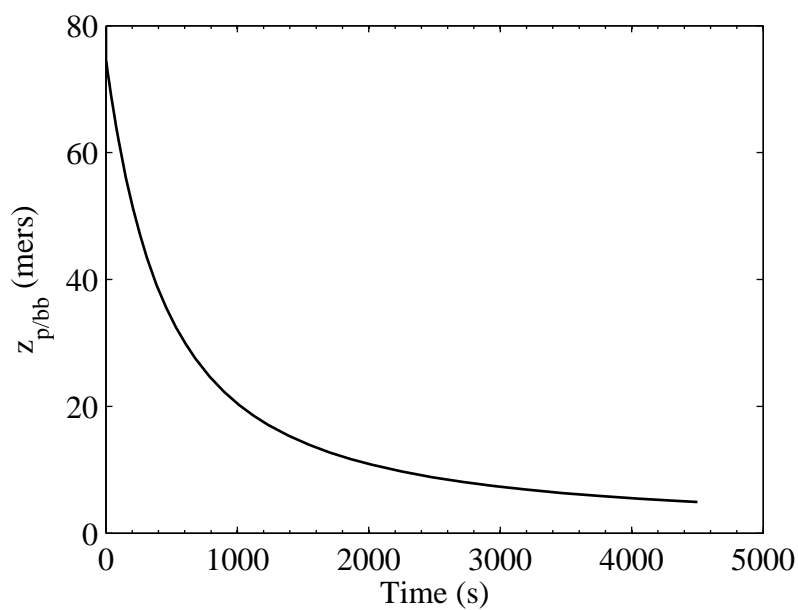
Figure 32: Concentration of polymer repeat units predicted by rate-equation model (solid line) compared to critical concentration c^* (dashed line) necessary for polymer coil overlap, calculated from Equation (55).

rate-equation model is significantly greater than the critical concentration c^* estimated by Equation (55), indicating that the polymer coils do overlap each other. This finding, taken with the data shown in Figure 30(a) and 30(b), indicates that backbiting may be highly dominant in branch formation over intermolecular chain transfer even when polymer coils come in contact with one another in solution. When polymer coils overlap in solution, the common assumption is that intermolecular chain transfer to polymer should be significant in branch formation, but the results presented here show that this assumption is not valid for this system. Even though the polymer chains overlap in solution, the overwhelming majority of all branches, including long-chain branches, are produced by backbiting.

Determination of the long-chain branch concentrations based solely upon the number-average chain length and the distance of a backbite from the radical chain-end appears to be reasonable at first glance. The drawback to this basic approach, however, is that it does not account for any other kinetic or microstructural factors which

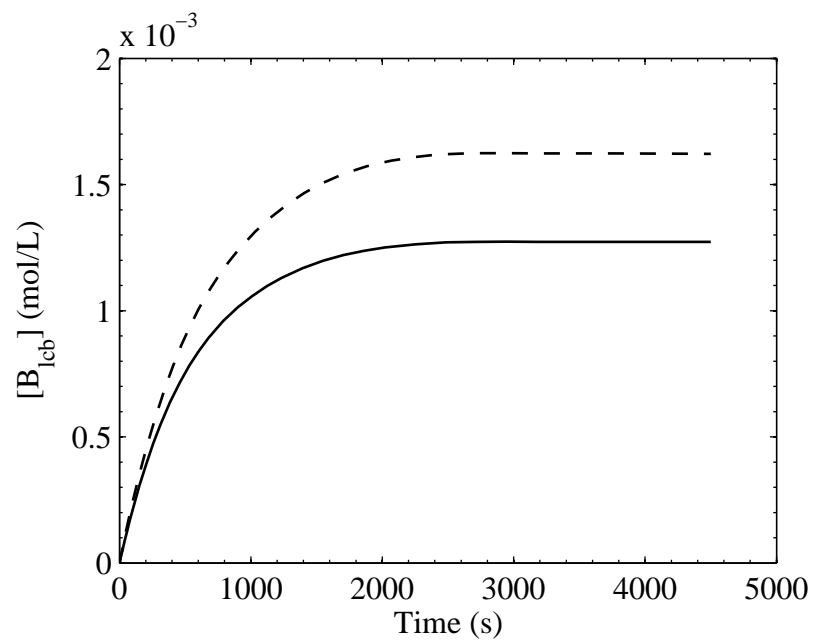


(a)

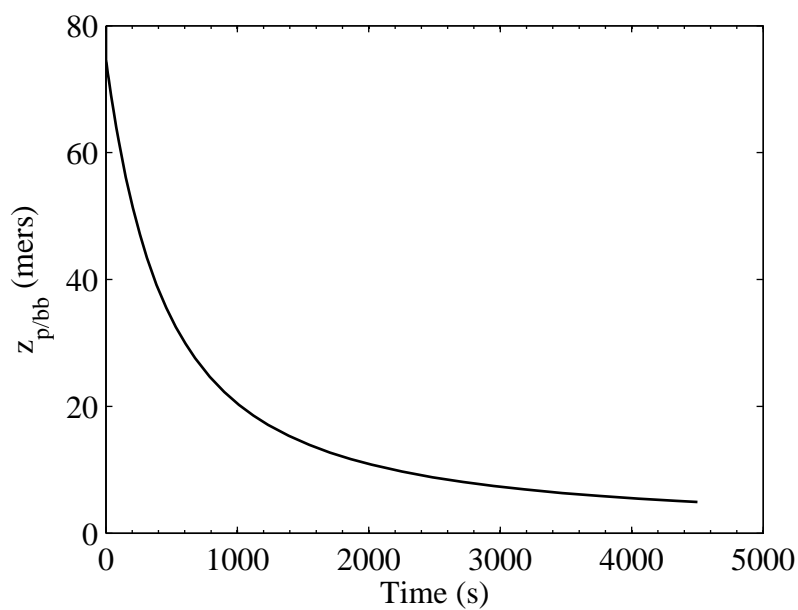


(b)

Figure 33: (a) Long-chain branch concentration at $L_{cut} = 10$ both with (solid line) and without (dashed line) backbiting as a branch-stopping event; (b) $z_{p/bb}$, the number of propagation events per backbiting event, calculated from Equation (56).

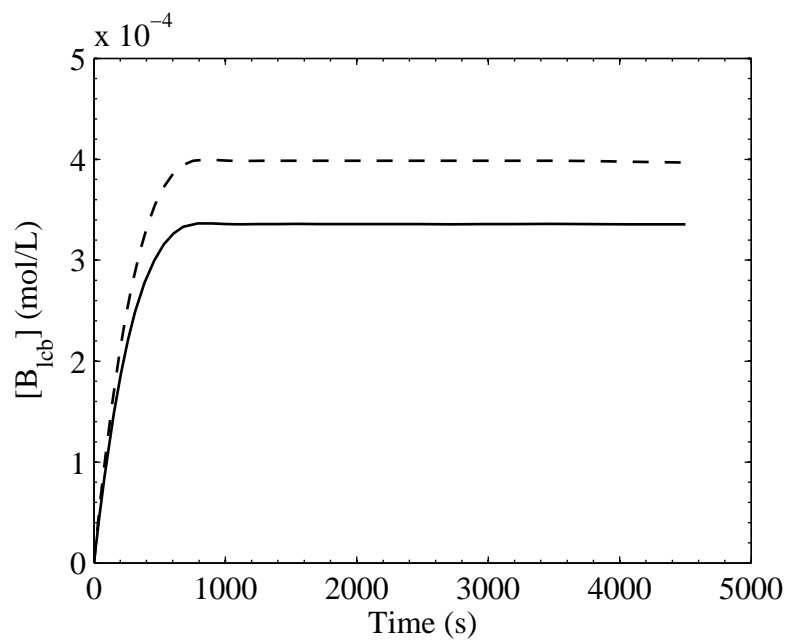


(a)

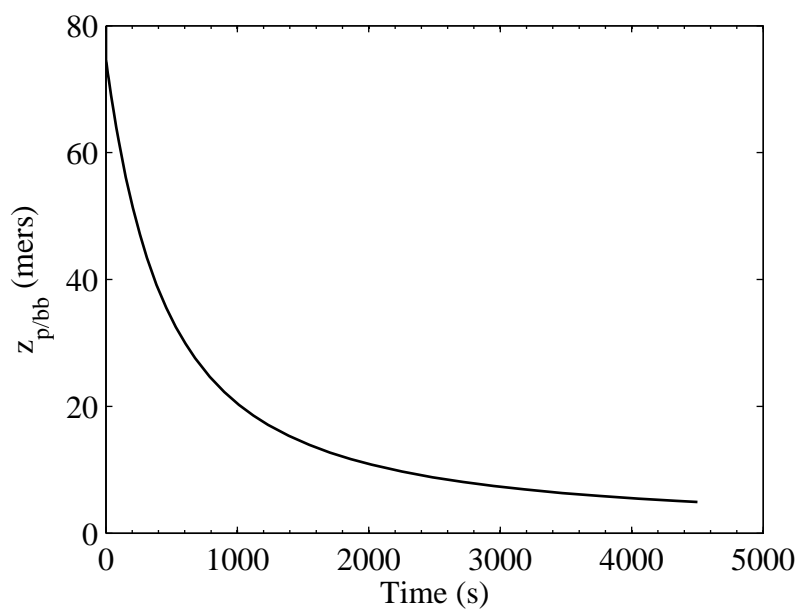


(b)

Figure 34: (a) Long-chain branch concentration at $L_{cut} = 25$ both with (solid line) and without (dashed line) backbiting as a branch-stopping event; (b) $z_{p/bb}$, the number of propagation events per backbiting event, calculated from Equation (56).



(a)



(b)

Figure 35: (a) Long-chain branch concentration at $L_{cut} = 40$ both with (solid line) and without (dashed line) backbiting as a branch-stopping event; (b) $z_{p/bb}$, the number of propagation events per backbiting event, calculated from Equation (56).

may affect the amount of long-chain branches. Figure 17 illustrates one such factor, where the growth of a radical after branching determines whether a long-chain or short-chain branch is created. Under the more general definition of long-chain branching, Figure 17(a) would be correctly interpreted as producing a long-chain branch, as the radical propagates for a length greater than L_{cut} . The new segment becomes part of the backbone of the chain. In Figure 17(b), a branch-stopping event occurs before the radical propagates to a length of L_{cut} , so a backbiting event that appears to have formed a long-chain branch instead forms a short-chain branch, since the new segment is classified as a branch. The segments contained in the backbone of the chain remain the same in Figure 17(b). While any chain-stopping event is also a branch-stopping event, backbiting stops the growth of a branch without stopping chain growth. Figure 33(a), 34(a), and 35(a) show the concentration of long-chain branches both with and without backbiting included as a branch-stopping event. Equation (48) is used to calculate the probability of a radical propagating to a length of L_{cut} before a branch-stopping event occurs. Figure 33(b), 34(b), and 35(b) show the average number of propagation events that occur between backbiting events, calculated as

$$z_{p/bb} = \frac{k_p[M]}{R_{bb}\left(\frac{\mu_n}{2}\right)} \quad (56)$$

where $R_{bb}\left(\frac{\mu_n}{2}\right)$ is the cumulative backbiting rate taken at half the number-average chain length. $z_{p/bb}$ decreases with monomer concentration, while the decrease in number-average chain length has a minimal effect. As the value of L_{cut} is increased, the value of $z_{p/bb}$ reaches L_{cut} sooner, with this critical time dropping from 2190 seconds at $L_{cut} = 10$ down to 370 seconds at $L_{cut} = 40$. When the critical value of $z_{p/bb}$ is reached, the generation of long chain branches slows and eventually ceases, an effect clearly observed in Figure 34(a) and 35(a). If backbiting is excluded, more long-chain branches are produced, although the difference between the two cases decreases as the value of L_{cut} is increased. While the ratio $z_{p/bb}$ explains one significant impact

of the reaction kinetics on the branch length, other additional factors are likely to affect the amount of long-chain branching, including backbiting from a branch to the backbone of a chain. Such additional factors are not as straightforward to implement in the rate-equation model, as they depend upon the branching topology of individual chains and the distribution of chain lengths.

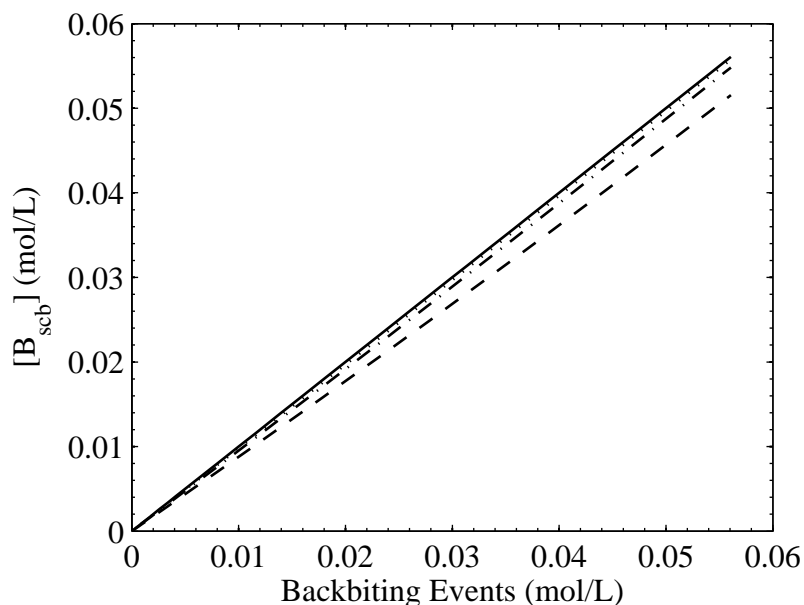


Figure 36: Concentration of short-chain branches vs. concentration of backbiting events, using cutoff lengths of 9 mers (dashed line), 24 mers (dash-dot line), and 39 mers (dotted line). The solid line has a slope of one, which is the limit where all backbiting events produce a short-chain branch.

Figure 36 illustrates the likelihood of a backbiting event forming a branch within a given range of lengths. As the maximum length is increased for short-chain branches, more of the branches are captured within the given range. A significant fraction of branches, about 92% of the final content, have a length up to 9 mers. Figure 36 shows that a small fraction of branches, about 6%, have a length between 10 to 24 mers, and an even smaller fraction, about 2%, have a length between 25 to 39 mers. By the end of the simulation, essentially all of the backbiting events have resulted in branches, due to termination of mid-chain radicals, so using backbiting events as the abscissa, instead of branches produced from backbiting, has a negligible effect on

Figure 36.

6.4 Viscosity Predictions

Short-chain and long-chain branching can affect chain overlap and entanglements by reducing the radius of gyration of polymer chains. To quantify the effects of branching on the radius of gyration, the intrinsic viscosity is calculated, using Equation (25) – (30) to determine the influence of long-chain branching, and Equation (31) – (33) to estimate the additional effect on $[\eta_b]$ resulting from short-chain branching. As seen in Figure 37 and 38, the intrinsic viscosity is most strongly influenced by the molecular weight, following a similar downward trend even when including the effects of branching. The rate equation model only predicts the number-average molecular weight, so this is used in place of the viscosity-average molecular weight in the Mark-Houwink-Sakurada equation, a substitution that is likely to have a significant effect on the linear-chain viscosity. Since the focus here is on predicting the effect of long-chain and short-chain branching on the intrinsic viscosity, the primary concern is the change in the intrinsic viscosity due to branching, rather than the actual values. Figure 37(a) shows that long-chain branching reduces the intrinsic viscosity by nearly 2 mL/g initially, but that this reduction is less than 1 mL/g at the end of the simulation, due to the decreasing rate of formation of long-chain branches. Figure 37(b) and 38 show that the long-chain branched viscosity becomes closer to the linear-chain viscosity as the cutoff length is increased, due to the smaller number of branches classified as long-chain branches. The error introduced by neglecting short-chain branching increases with time due to the faster rate of formation of short-chain branches relative to long-chain branches, so that the multiple $G_{lcb}G_{scb}$ in Equation (33) remains nearly constant throughout the entire simulation. Interestingly, the value of $[\eta_b]$ is fairly insensitive to the choice of cutoff length L_{cut} . However, the values of $[\eta_b]$ and $[\eta_l]$ are nearly overlapping at $L_{cut} = 40$, similar to the observations of Castignolles et al.

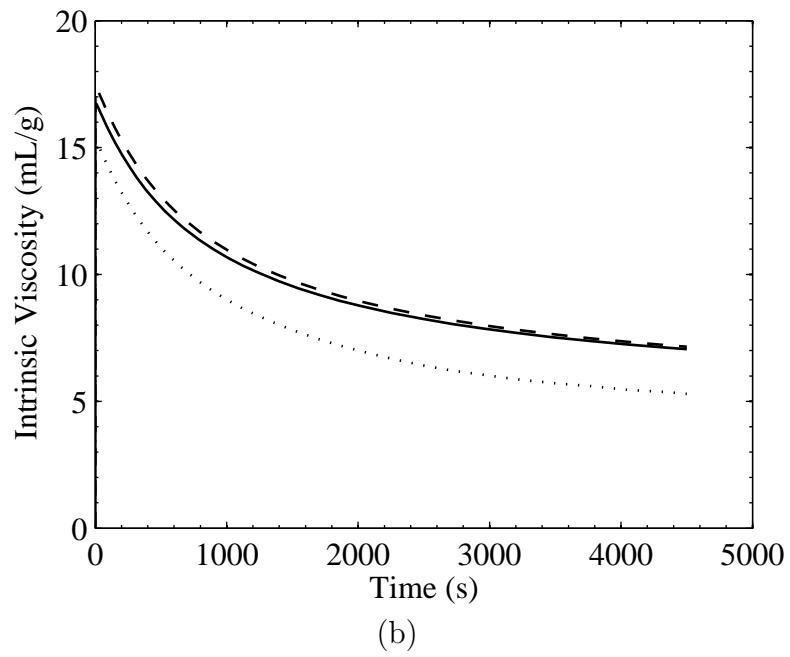
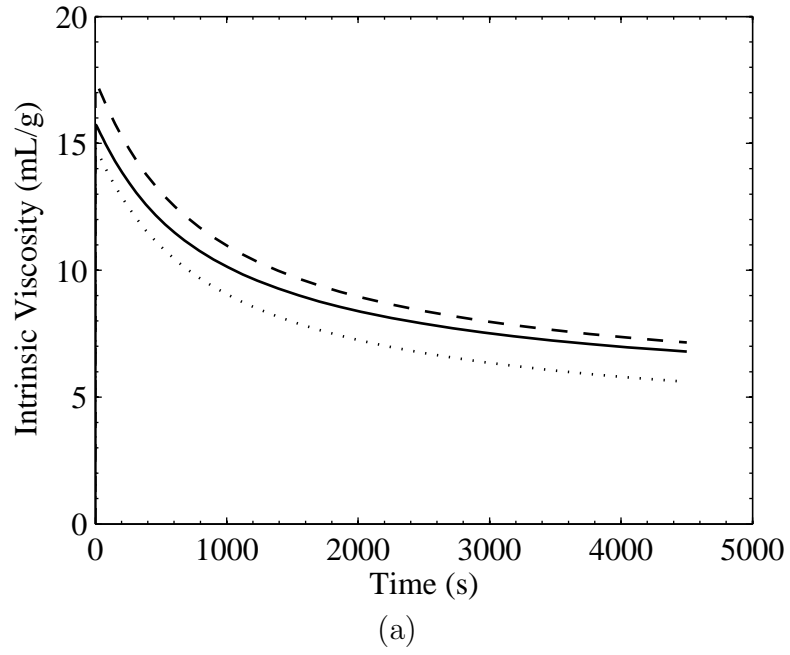


Figure 37: Intrinsic viscosity predicted from rate-equation simulation at (a) $L_{cut} = 10$ and (b) $L_{cut} = 25$, showing $[\eta_i]$ (dashed line), $[\eta_b]$ (solid line), and $[\eta_{corr}]$ (dotted line).

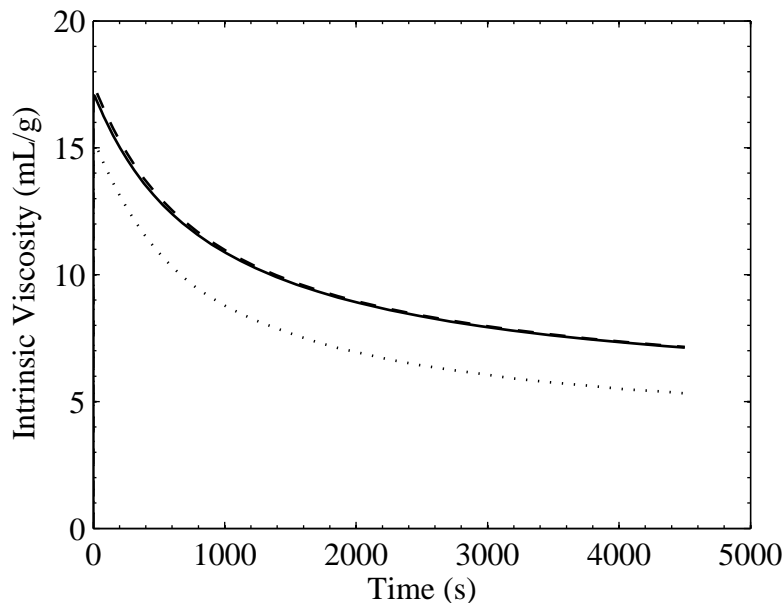


Figure 38: Intrinsic viscosity predicted from rate-equation simulation at $L_{cut} = 40$, showing $[\eta_l]$ (dashed line), $[\eta_b]$ (solid line), and $[\eta_{corr}]$ (dotted line).

[34], who interpret the similarity in their branched and linear-chain viscosities as an indication that no long-chain branching is present in their samples of butyl acrylate. Due to the need for more sensitive measurement techniques [34] and the use of inexact correlations to calculate linear-chain viscosity, the low levels of long-chain branching predicted by the simulations presented here may not currently be observable in the laboratory. The possibility also exists that some branches of intermediate length, between 10 to 40 mers, are not easily observed through viscosity measurements, so these simulations incorporating the backbiting CDF provide insight into branches in this range of lengths.

In addition to the potential effects of chain conformation discussed earlier, another important aspect of the backbiting CDF in Figure 15 is that it is for an isolated chain. In bulk polymerizations or melts or at high conversion, the CDF may not be as accurate and may over-predict the amount of long-chain branches from backbiting, due to higher amounts of intermolecular chain transfer to polymer. However, given the orders-of-magnitude difference between $[B_{bb}]$ and $[B_{ctp}]$, neither the discrepancies

in chain conformation nor the isolation of the chain should change the conclusion that backbiting is likely the dominant event creating long-chain branches for this solution polymerization system.

6.5 Conclusions

The rate-equation model presented here provides good agreement with experimental data for the solution polymerization of butyl acrylate. In agreement with previous studies, the model predicts that a majority of branches are formed through backbiting. While the kinetic predictions appear reasonable compared to experimental data, the focus of this modeling effort is not the accuracy of either the kinetic or the viscosity predictions, but rather the commonly-held assumption that backbiting only produces short-chain branches while intermolecular chain transfer to polymer produces any long-chain branches. Kinetic and NMR branching data are combined to provide insight into the kinetic origin of the branches. Using a cumulative distribution function for the backbiting rate, the model predicts that backbiting can form a measurable fraction of branches that are much longer than the typically assumed backbiting length of 2 mers. This finding is in contrast to the common assumption that all long-chain branching results from intermolecular chain transfer to polymer. Backbiting is shown to be overwhelmingly dominant over intermolecular chain transfer to polymer for the entire polymerization, a finding that is especially noteworthy because, for the majority of the polymerization, the concentration of polymerized mers is above the critical concentration for chain overlap, a condition that would normally be assumed to lead to significant intermolecular chain transfer to polymer. The predictions of intrinsic viscosity indicate that the amount of branching resulting from backbiting should have an observable effect on the intrinsic viscosity. The combination of spatial and non-spatial models used in this work provides insights into the development of the branching structure that otherwise would not be easily achieved.

With the availability of both NMR and viscosity data, future modeling studies can now distinguish between these different kinetic origins of branching.

CHAPTER VII

EXAMINATION OF THE BRANCH-LENGTH DISTRIBUTION IN BUTYL ACRYLATE USING THE WELL-MIXED DISCRETE MODEL

The focus of this chapter is the study of the branch-length distribution in butyl acrylate solution polymerization using the well-mixed kinetic Monte Carlo (KMC) model to provide detailed information regarding the branching topology of chains, which is not readily accessible using the rate-equation model. As the well-mixed KMC model requires a finite system size, a significant effect present in these results is the artificial confinement of radicals. The continuity of the single phase in solution polymerization precludes the possibility of zero-one kinetics, as absorption and desorption of radicals are irrelevant, so two or more radicals may exist until termination by combination occurs. The system size for the KMC model is varied, therefore providing insight into how the amounts of short-chain and long-chain branching could vary inside a confined system. A more realistic prediction of the amounts of short-chain and long-chain branching is made possible by the detailed recording of branching topology in individual chains.

7.1 Rate Constants

To apply the rate constants used in the preceding chapter to the well-mixed KMC model, the rate constants must be scaled down to the level of reactions between individual molecules. The symbols used in this chapter refer to the molecular reaction rates shown in Table 2. For initiator dissociation, the molecular rate constant $k_{d,m}$ is identical to the macroscopic value. The molecular rate constants for

propagation of secondary and mid-chain radicals are given by $k_{p,m} = k_p / (V_{sol}N_A)$ and $k_{p,mcr,m} = k_{p,mcr} / (V_{sol}N_A)$, respectively, where V_{sol} is the volume of the system under consideration and N_A is Avogadro's number. The molecular rate constants for chain transfer to monomer for secondary and mid-chain radicals are given by $k_{tr,m,m} = k_{tr,m} / (V_{sol}N_A)$ and $k_{tr,m,mcr,m} = k_{tr,m,mcr} / (V_{sol}N_A)$, respectively. As the concentration of monomer decreases, the rates of propagation and chain transfer to monomer decrease. The initial concentration of butyl acrylate in the system, $[M]_0$, is 1.63 mol/L [79], so the initial rates of propagation and chain transfer to monomer are determined by this concentration. The molecular rate constant for chain transfer to solvent is calculated as $k_{tr,s,m} = k_{tr,s} / (V_{sol}N_A)$. The concentration of solvent in the system is assumed to remain constant at a value of 5.82 mol/L [79].

Table 7: Molecular rate constants for butyl acrylate at 70 °C and a system radius of 100 nm, calculated from macroscopic values taken primarily from Nikitin et al. [79]

Rate Constant	Molecular Value	Units	Reference
$k_{d,m}$	2.36×10^{-4}	s^{-1}	[3]
$k_{p,m}$	1.65×10^{-2}	s^{-1}	[12]
$k_{t,m}$	1.49×10^2	s^{-1}	[19, 78]
$k_{tr,m,m}$	1.25×10^{-6}	s^{-1}	[70]
$k_{tr,s,m}$	1.39×10^{-5}	s^{-1}	[79]
$k_{tr,p,m}$	5.97×10^{-8}	s^{-1}	[9]
$k_{bb}(93/2)$	880	s^{-1}	[79]
$k_{p,mcr,m}$	2.11×10^{-5}	s^{-1}	[55]
$k_{tr,m,mcr,m}$	7.61×10^{-9}	s^{-1}	[70]
$k_{t,mcr,m}$	2.0	s^{-1}	[19, 78]
$k_{t,h,m}$	30.5	s^{-1}	[19, 78]

For reactions involving two chains, including termination and chain transfer to polymer, the number of potential reactions in the system must be considered. When n radicals are present in any system, and n is a small number, the number of possible

combinations between the radicals scales as $n(n-1)/2$. As the value of n approaches infinity, this scaling approaches $n^2/2$. For a small number of radicals, especially just one or two, the scaling of $n^2/2$ is not accurate, so the number of termination reactions must be calculated as $n(n-1)/2$, in the cases of termination between two secondary radicals or termination between two mid-chain radicals. For the case of hybrid termination between secondary radicals and mid-chain radicals, the number of termination reactions is calculated as $n_s n_m / 2$, where n_s is the number of secondary radicals and n_m is the number of mid-chain radicals. Termination requires the presence of two radicals, so the molecular rate constants for termination between two secondary radicals, hybrid termination between a secondary and a mid-chain radical, and termination between two mid-chain radicals are calculated, respectively, as

$$k_{t,m} = k_t [R^*] \quad (57)$$

$$k_{t,h,m} = k_{t,h} [R^*] \quad (58)$$

$$k_{t,mcr,m} = k_{t,mcr} [R^*] \quad (59)$$

where $[R^*]$ is the concentration of two radicals in the system, $2 / (V_{sol} N_A)$. Intermolecular chain transfer to polymer requires a radical to react with a bonded mer, so the molecular rate is computed as shown in Table 2:

$$r_{tr,p,m} = k_{tr,p,m} \sum_{i=1}^n \left(\sum_{j=1}^{N_c} M_j - M_i \right) \quad (60)$$

where n is the total number of radicals, N_c is the total number of chains, M_j is the number of mers in each chain, and M_i is the length of the chain containing radical i . In the KMC model, each possible reaction of a radical with a bonded mer in another chain is counted as an intermolecular chain transfer event. The number of

intermolecular chain transfer to polymer events for a single radical is then equal to the total number of monomers that have reacted through propagation, excluding the length of the chain containing that radical. M_i must be subtracted for each radical, since a radical is not allowed to transfer to mers in its own chain, as this would constitute a backbiting event. The molecular rate constant for intermolecular chain transfer to polymer is then calculated as

$$k_{tr,p,m} = k_{tr,p} [M^*] \quad (61)$$

where $[M^*]$ is the concentration of one bonded mer in the system, $[M^*] = 1/(V_{sol}N_A)$, so each bonded mer is assumed to have an equal probability of receiving a radical through a chain transfer event.

The rate constant for backbiting $k_{bb}(j)$ at a specified distance j is given by the incremental increase $R_{bb}(j) - R_{bb}(j - 1)$ of the cumulative distribution function. For the well-mixed KMC model, the cumulative backbiting rate for each radical is computed as

$$r_{bb} = \sum_{j=2}^D m_j [R_{bb}(j) - R_{bb}(j - 1)] \quad (62)$$

where m_j is the number of mers at a distance j from the radical, stored in the backbiting arrays as mentioned previously. In the case of a linear chain, this would simply be $R_{bb}(D)$, but when there are branches, Equation (62) gives a different result. For the backbiting CDF used in the KMC simulations, the maximum backbiting distance D is 1999 mers. An alternate calculation of the backbiting rate r_{bb} is given in Table 2, summing over all secondary radicals in the particle, where $m_{i,j}$ is the number of mers at a distance j from radical i . Because they are less mobile, mid-chain radicals are not permitted to backbite in our well-mixed KMC model. As mentioned in the previous chapter, Nikitin calculated a backbiting rate of 880 s^{-1} for a number-average chain length of 93, but this average is primarily comprised of dead chains. The average length of a live chain is taken to be half its dead length, so the

backbiting CDF is converted to a backbiting rate distribution according to the value $k_{bb}(93/2) = 880 \text{ s}^{-1}$.

7.2 Comparison to Experimental Data

As Figure 39 shows, the conversion versus time data from the KMC simulations are in reasonable agreement with the experimental data [79], but the conversion rate from each of the KMC simulations is lower than that predicted by the rate-equation model. This decrease in the conversion rate is due to the effects of artificial confinement introduced in the KMC simulation. Since the experimental data are for the solution polymerization of butyl acrylate, no confinement of radicals occurs in the experimental system; the rate-equation model does not include confinement effects. The conversion rate increases with the system radius, as shown in Figure 39, because

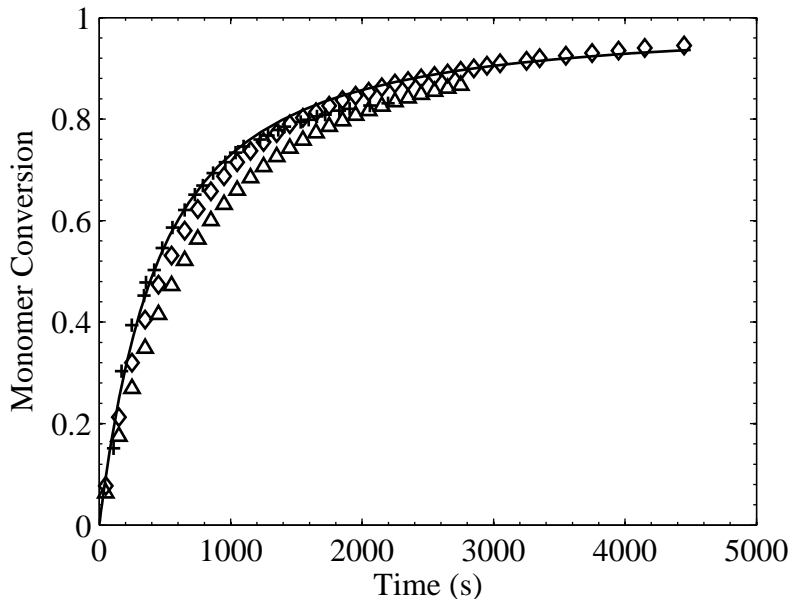


Figure 39: Monomer conversion from KMC simulations with system radii of 100 nm (triangle) and 200 nm (diamond) compared to rate-equation simulation (solid line) and experimental data from Nikitin et al. (+) [79].

confinement of radicals increases the molecular termination rate constant, decreasing the average lifetime of each radical. The average number of secondary radicals for the system radius of 200 nm is about 0.29 with an average radical lifetime of 0.19

seconds, but this decreases to 0.04 secondary radicals for the system radius of 100 nm, with an average radical lifetime of 0.084 seconds, indicating that the lifetime of an average radical is indeed reduced by the increase in confinement. The level of detail captured by the KMC model limits the system size to approximately 10^7 monomers, to stay within a reasonable computational time, and the system with a 200-nm radius contains 3.2×10^7 monomers. Increasing the system radius to 250 nm causes an increase in computational time from 20 to 60 hours per realization, on average, as this doubles the number of monomers. Data from KMC simulations using a radius of 250 nm show a negligible increase in conversion rate, and doubling the system size again would likely have resulted in a computational time around one week per realization, so no simulations were attempted beyond the 250-nm radius. For the system radius of 100 nm, the results presented in this work are an average over 50 individual simulation runs, while for the 200-nm system radius, the results are an average over 6 individual runs, since the 200-nm system contains eight times the number of monomers in the 100-nm system, so approximately the same total number of monomers are included for each system size when summing over all the runs. Increasing the system size increases the number of chains in each run, so fewer runs are necessary to achieve the same sample size as for a smaller system.

The data presented in Figure 40 show that the number-average molecular weights predicted by the KMC simulations are initially lower than those predicted by the rate-equation model, but the values from the KMC simulations quickly become greater than the values from the rate-equation model, although only slightly. The values of the number-average molecular weight (MW_n) predicted by the KMC simulations still pass reasonably close to the experimental data point [79]. As Figure 40 shows, MW_n decreases along with monomer concentration, so chain transfer to monomer should not be the dominant chain-stopping event, otherwise MW_n would increase as

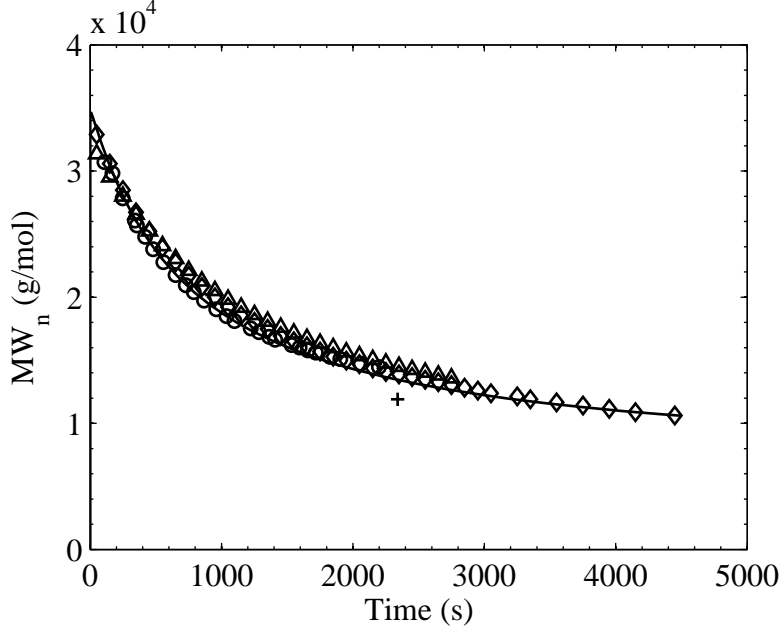


Figure 40: Number-average molecular weight from KMC simulations with system radii of 100 nm (triangle) and 200 nm (diamond) compared to rate-equation simulation (solid line), results from the model of Nikitin et al. (circle) [79] and experimental data point from Nikitin et al. (+).

the monomer concentration decreases. Since terminal-double bond (TDB) polymerization is included in the KMC simulations, and TDBs are generated through chain transfer to monomer, the value of MW_n resulting from chain transfer to monomer should be estimated to determine whether TDB polymerization is significant. At zero monomer conversion, the expected molecular weight from chain transfer to monomer is calculated as:

$$MW_{n,tr,m} = \frac{MW_{BA}k_p[M]_0}{k_{tr,m}[M]_0} = \frac{128.17 \times 41,643 \times 1.63}{3.16 \times 1.63} = 1.69 \times 10^6 \text{ g/mol} \quad (63)$$

This molecular weight is nearly two orders of magnitude higher than the initial value of MW_n of 3.5×10^4 g/mol predicted by the rate-equation model, so chain transfer to monomer indeed appears to be insignificant as a chain-stopping event. The concentration of TDBs is then vanishingly small when compared to the concentration of monomer, especially since none of the simulations exceed 95% conversion, so the

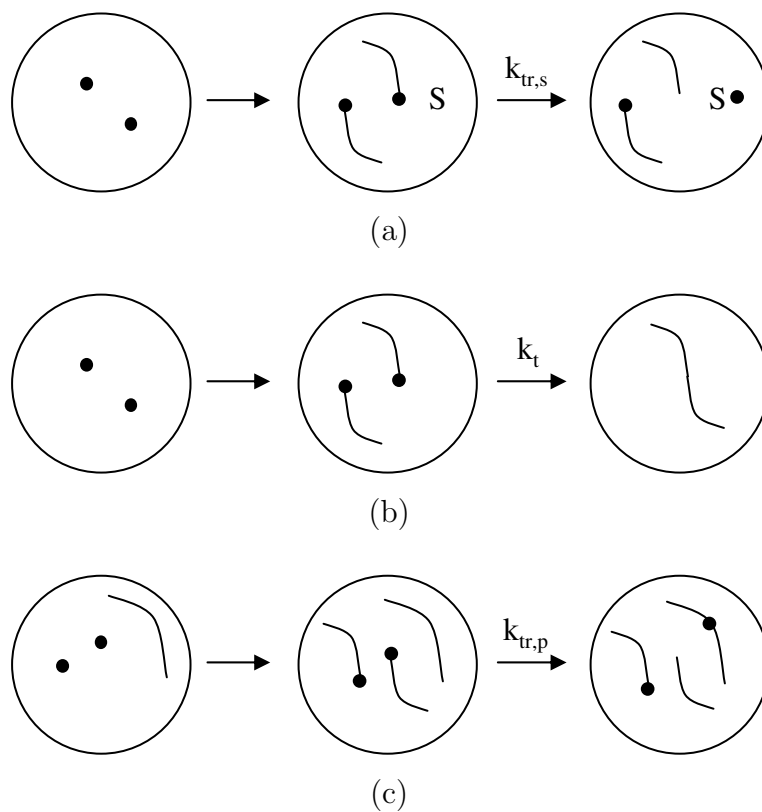


Figure 41: Possible chain-stopping events considered for butyl acrylate solution polymerization, including (a) chain transfer to solvent, (b) termination by combination, and (c) intermolecular chain transfer to polymer.

effect of TDB polymerization on the results should be negligible. The results from the steady-state model of Nikitin et al. [79] are in good agreement with both the rate-equation and KMC models. According to Nikitin et al. [79], chain transfer to solvent is the dominant chain-stopping event. As illustrated in Figure 41, three possible chain-stopping events are considered here, to determine which should be dominant. In Figure 41(a), dissociation of an oil-soluble initiator molecule is followed by propagation of both radicals, and then one of the radicals transfers to a solvent molecule. To verify that chain transfer to solvent is the dominant chain-stopping event, the expected molecular weight for chain transfer to solvent is calculated at zero monomer conversion:

$$MW_{n,tr,s} = \frac{MW_{BA}k_p[M]_0}{k_{tr,s}[S]_0} = \frac{128.17 \times 41,643 \times 1.63}{35.1 \times 5.82} = 4.25 \times 10^4 \text{ g/mol} \quad (64)$$

This molecular weight is reasonably close to the initial value of MW_n predicted by the rate-equation model. Termination by combination of two secondary radicals is illustrated in Figure 41(b), where two radicals are generated from an oil-soluble initiator molecule, and the radicals then propagate for the same duration before terminating. This gives an expected molecular weight of

$$MW_{n,t} = \frac{2MW_{BA}k_p[M]_0}{k_{t,m}} = \frac{2 \times 128.17 \times 41,643 \times 1.63}{149.2} = 1.17 \times 10^5 \text{ g/mol} \quad (65)$$

for the system radius of 100 nm and

$$MW_{n,t} = \frac{2MW_{BA}k_p[M]_0}{k_{t,m}} = \frac{2 \times 128.17 \times 41,643 \times 1.63}{18.65} = 9.33 \times 10^5 \text{ g/mol} \quad (66)$$

for the system radius of 200 nm. These values are higher than the initial MW_n predicted by the models, with a difference of nearly two orders of magnitude for the 200-nm radius, which has the smaller value of $k_{t,m}$ due to the decreased confinement of the radicals. In the absence of confinement, the molecular weight for termination

by combination would be even higher than 9.33×10^5 g/mol, so termination by combination is unlikely to be a significant chain-stopping event. Lastly, chain transfer to polymer should be considered, as illustrated in Figure 41(c), and this calculation must be done for some non-zero value of polymer concentration. The value of the molecular rate constant for chain transfer to polymer should be computed based on the concentration of polymerized mers, or rather the total concentration of monomers which have been consumed through propagation. At a monomer conversion of 5%, the cumulative molecular rate constant for chain transfer to polymer is

$$k_{tr,p,m,c} = 0.05k_{tr,p}[M]_0 = 0.05 \times 0.151 \times 1.63 = 1.23 \times 10^{-2} \text{ s}^{-1} \quad (67)$$

giving an expected MW_n of

$$MW_{n,tr,p} = \frac{MW_{BA}k_p[M]_0}{k_{tr,p,m,c}} = \frac{128.17 \times 41,643 \times 1.63}{1.23 \times 10^{-2}} = 7.09 \times 10^8 \text{ g/mol} \quad (68)$$

which is over 10^4 times the value of MW_n predicted by the KMC and rate-equation models. Based on the values of MW_n calculated for the various chain-stopping events, chain transfer to solvent appears to be dominant in determining the molecular weight for the confined systems examined here, even more so for unconfined systems. The fact that the molecular weights predicted by the KMC simulations become slightly higher than those predicted by the rate-equation model may be due to the lower rate of conversion in the confined systems, as observed in Figure 39. The predicted molecular weight in the KMC results is likely inflated due to the increased amount of propagation occurring between chain-stopping events, which results from the higher monomer concentrations in the KMC simulations. While termination by combination determines the total lifetime of a radical, and therefore affects the overall rate of conversion, its contribution as a chain-stopping event is shown to be insignificant. The rate of propagation for a radical is still determined by the instantaneous monomer

concentration.

7.3 Branching Predictions

Figure 42 shows that the degree of branching predicted by the KMC simulations decreases with increasing confinement. While the prediction of the rate-equation model compares well to the experimental data point [79], the predictions of the KMC simulations are somewhat lower. As the termination rate increases due to confinement, the decreasing radical lifetime provides fewer opportunities for backbiting or chain transfer to polymer, reducing the number of branch points. Most of the branches are

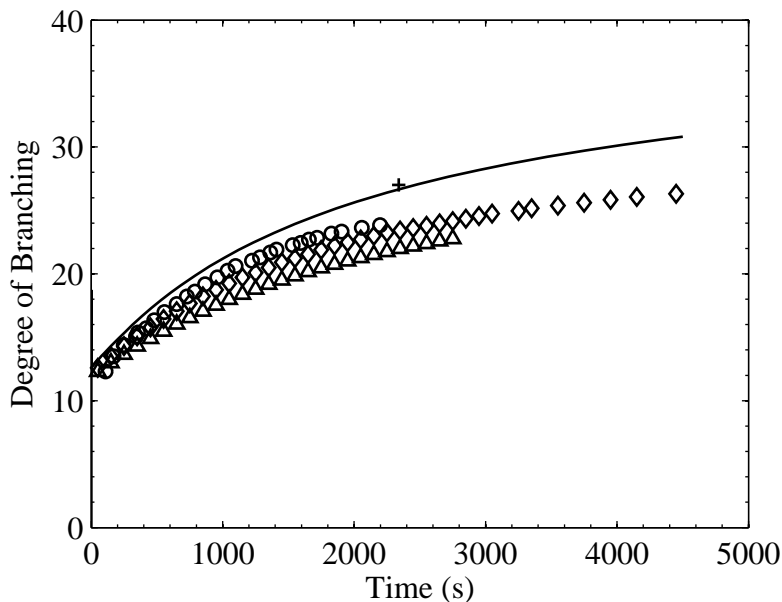


Figure 42: Degree of branching from rate-equation model (solid line) and KMC simulations for system radii of 100 nm (triangle) and 200 nm (diamond) compared to the results from the model of Nikitin et al. (circle) [79] and the experimental data point from Nikitin et al. (+).

produced by propagation of mid-chain radicals, 84% for the rate-equation simulation, so the rate of branch formation decreases with monomer concentration. The results in Figure 43 show that the concentration of branches produced by both backbiting and chain transfer to polymer decreases as the system size is reduced because of the reduced radical lifetime resulting from faster termination. Most of the branches are

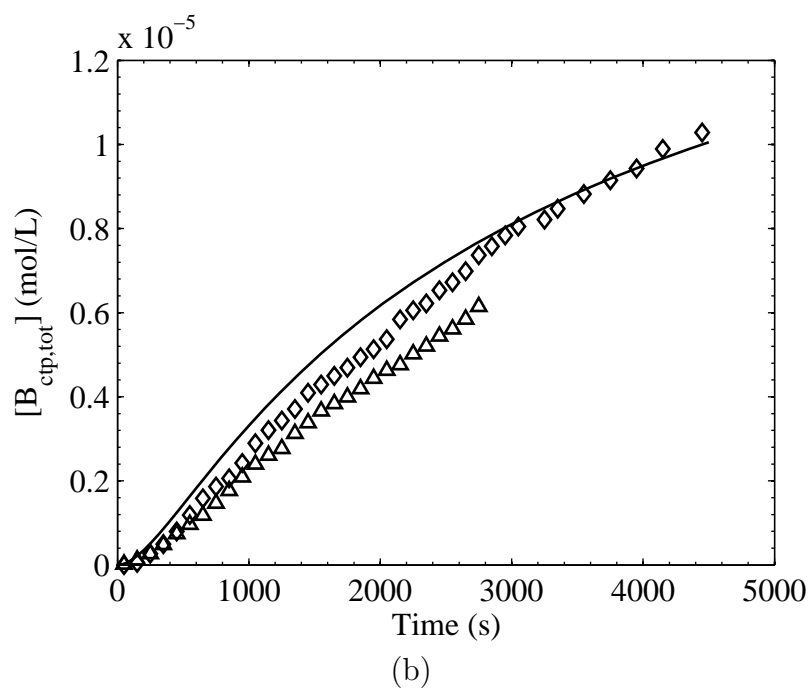
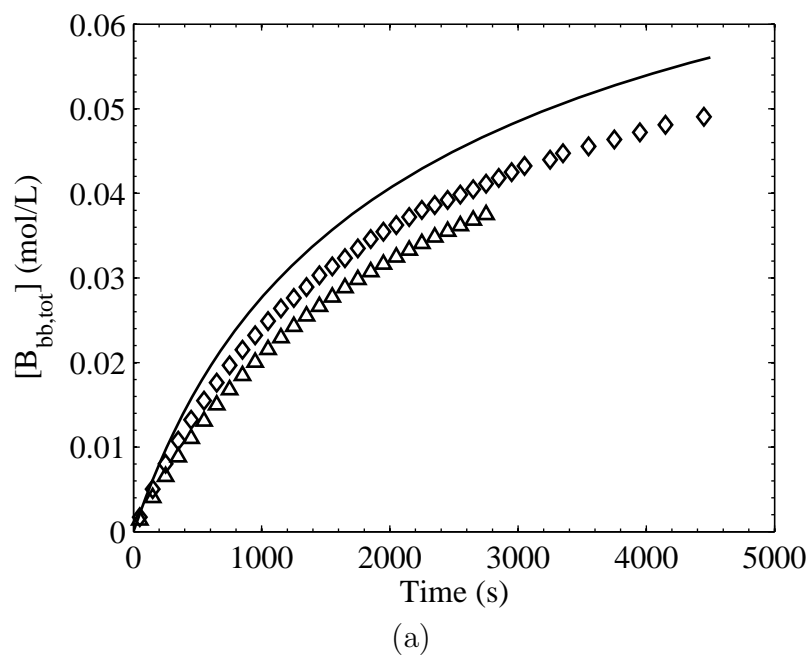


Figure 43: Concentration of branches produced by (a) backbiting and (b) intermolecular chain transfer to polymer, including branches produced by termination of mid-chain radicals, from rate-equation model (solid line) and KMC simulations for system radii of 100 nm (triangle) and 200 nm (diamond).

produced via backbiting, consistent with the assumptions made by Nikitin et al. [79]. To show the significance of this finding, the critical concentration of repeat units for polymer coil overlap, c^* , is calculated from Equation (55) and compared to the concentration of repeat units calculated from the rate-equation and KMC simulations.

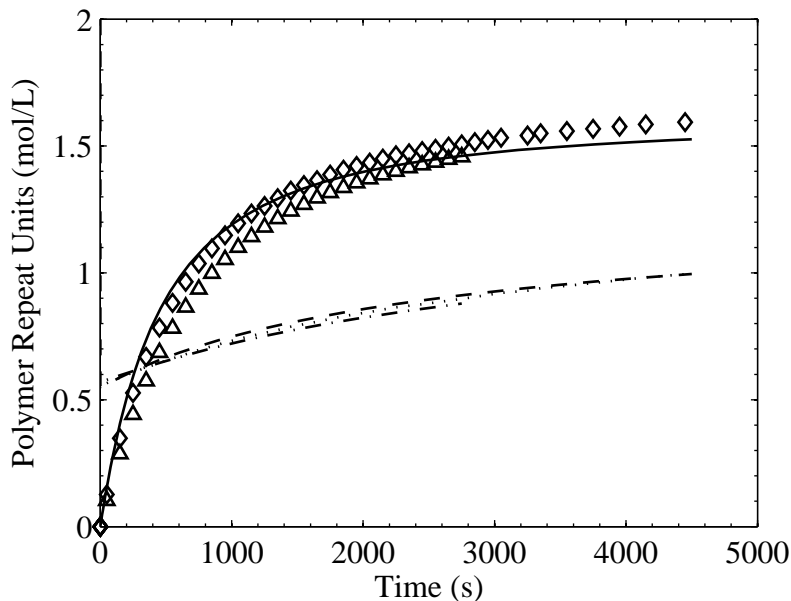


Figure 44: Concentration of polymer repeat units predicted by rate-equation model (solid line) and KMC simulations for system radii of 100 nm (triangle) and 200 nm (diamond), compared to critical concentration c^* calculated from Equation (55) for rate-equation model (dashed line) and KMC simulations for system radii of 100 nm (dash-dot line) and 200 nm (dotted line).

Figure 44 shows that the concentration of polymer repeat units predicted by each of the simulations is greater than the critical concentration c^* estimated by Equation (55), indicating that the polymer coils do overlap each other. This finding, taken with the data shown in Figure 43(a) and 43(b), indicates that backbiting may be highly dominant in branch formation over intermolecular chain transfer even when polymer coils come in contact with one another in solution. As shown in Figure 44, the variation between the values of c^* calculated for the rate-equation model and the KMC simulations is minimal, while the concentration of polymer repeat units for each simulation follows a trajectory similar to that of the monomer conversion. The results

from the KMC simulations show that, as with the rate-equation model, the common assumption that intermolecular chain transfer to polymer should be significant in branch formation when polymer coils overlap in solution is not valid for this system. Even though the polymer chains overlap in solution, the overwhelming majority of all branches, including long-chain branches, are produced by backbiting.

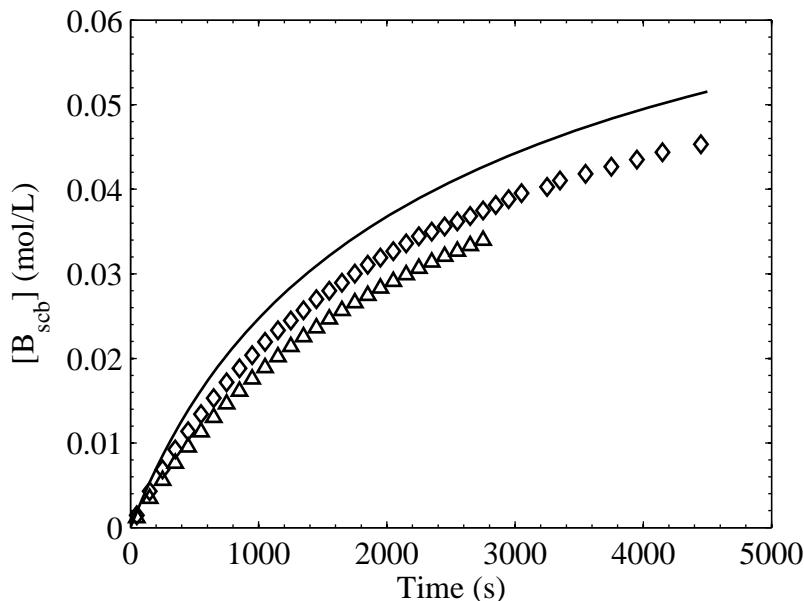


Figure 45: Concentration of short-chain branches at $L_{cut} = 10$, including branches produced by termination of mid-chain radicals, from rate-equation model (solid line) and KMC simulations for system radii of 100 nm (triangle) and 200 nm (diamond).

Figure 45, 46, and 47 show that the short-chain branch concentrations follow a similar trajectory to the data in Figure 43(a) for the concentration of branches produced by backbiting, and that the concentration of short-chain branches increases slightly as the value of L_{cut} is increased from 10 to 40 mers. Comparison of the short-chain branch concentrations to the corresponding long-chain branch concentrations in Figure 48(a), 49(a), and 50(a) shows that most of the branches are short-chain branches, as expected based on the backbiting CDF. Following the same trend as the other plots of branch concentration, the rate of formation of long-chain branches decreases with monomer concentration. The concentration of long-chain branches also

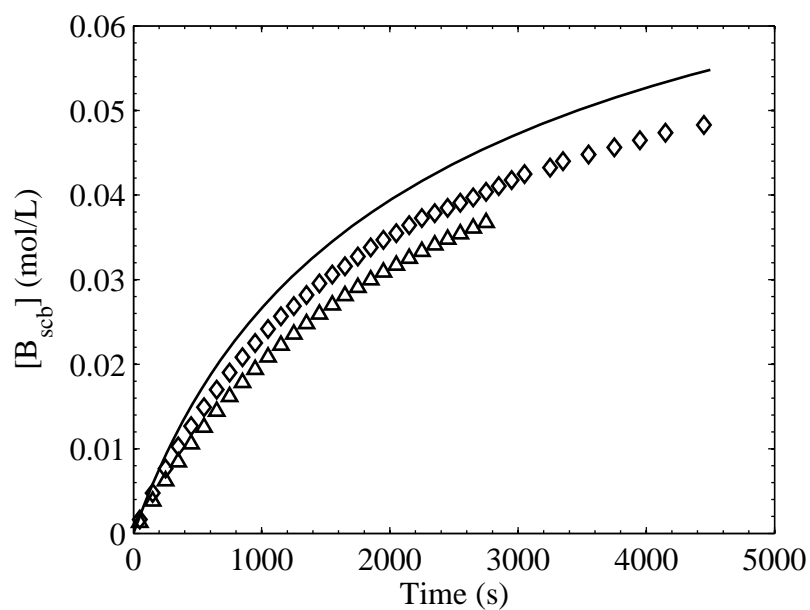


Figure 46: Concentration of short-chain branches at $L_{cut} = 25$, including branches produced by termination of mid-chain radicals, from rate-equation model (solid line) and KMC simulations for system radii of 100 nm (triangle) and 200 nm (diamond).

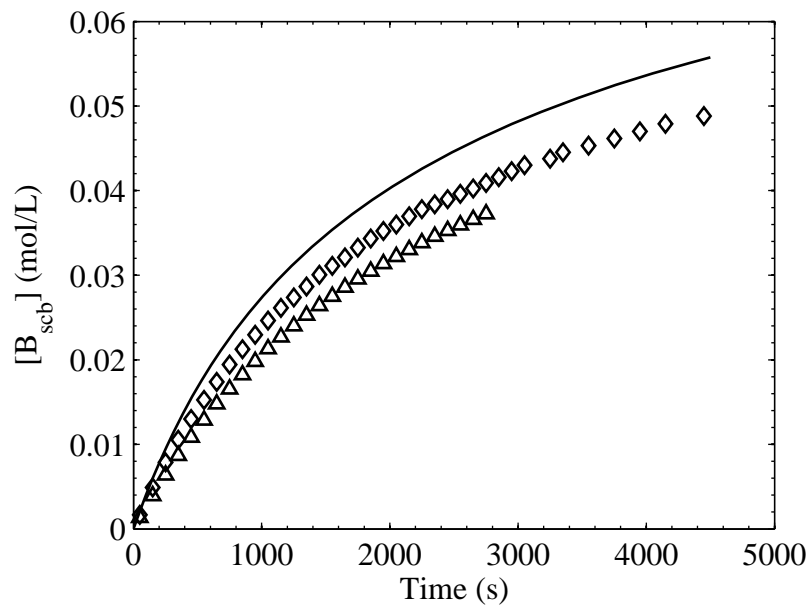


Figure 47: Concentration of short-chain branches at $L_{cut} = 40$, including branches produced by termination of mid-chain radicals, from rate-equation model (solid line) and KMC simulations for system radii of 100 nm (triangle) and 200 nm (diamond).

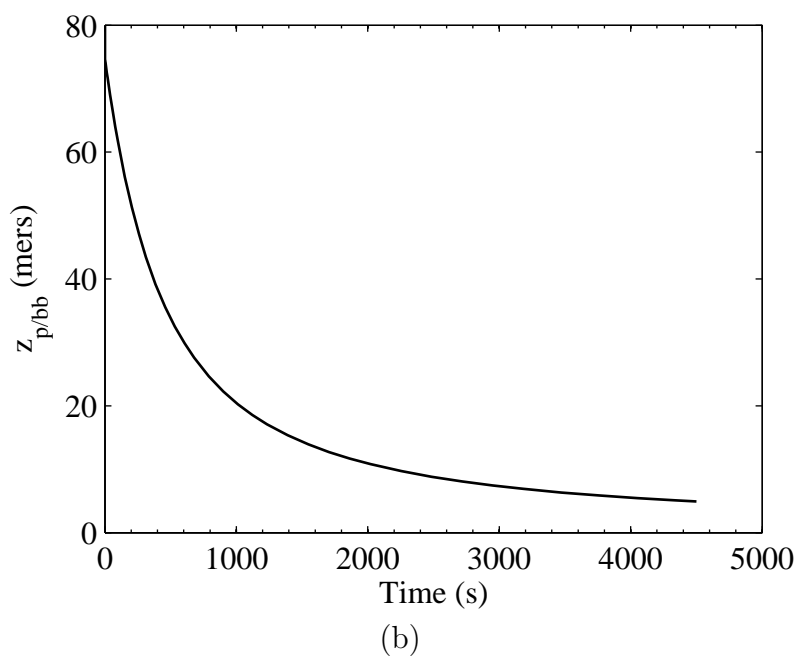
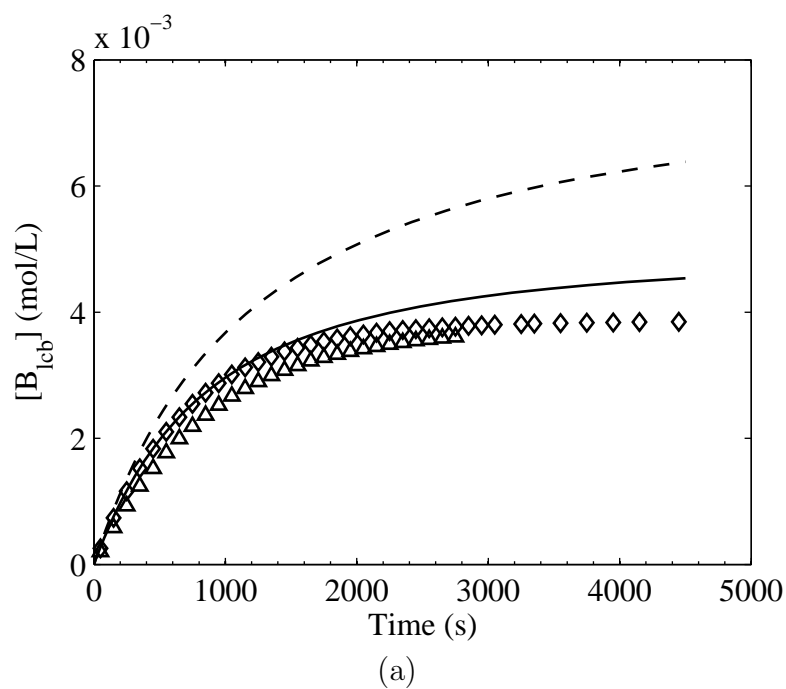


Figure 48: (a) Long-chain branch concentrations at $L_{cut} = 10$, from KMC simulations for system radii of 100 nm (triangle) and 200 nm (diamond) and from rate-equation model, determined both with (solid line) and without (dashed line) backbiting as a branch-stopping event; (b) $z_{p/bb}$, the number of propagation events per backbiting event, calculated from Equation (56).

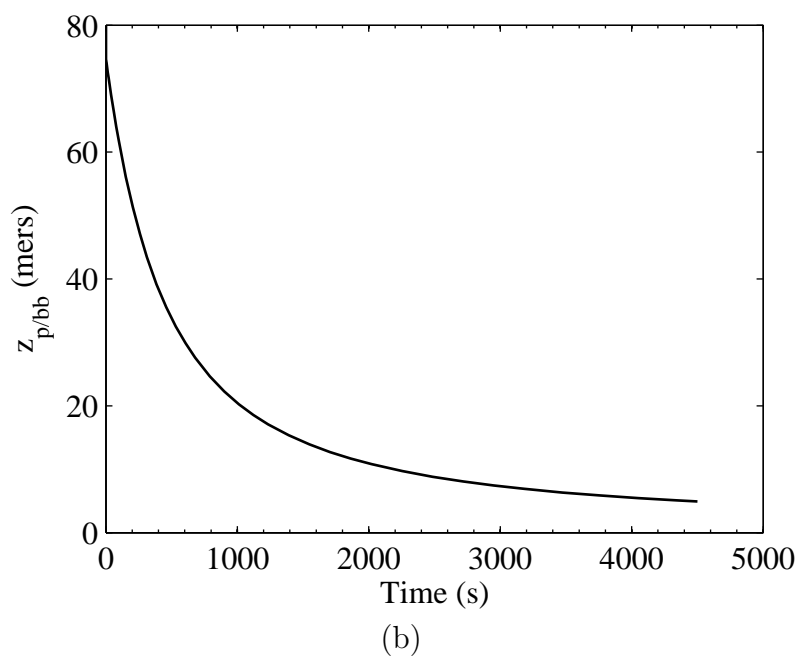
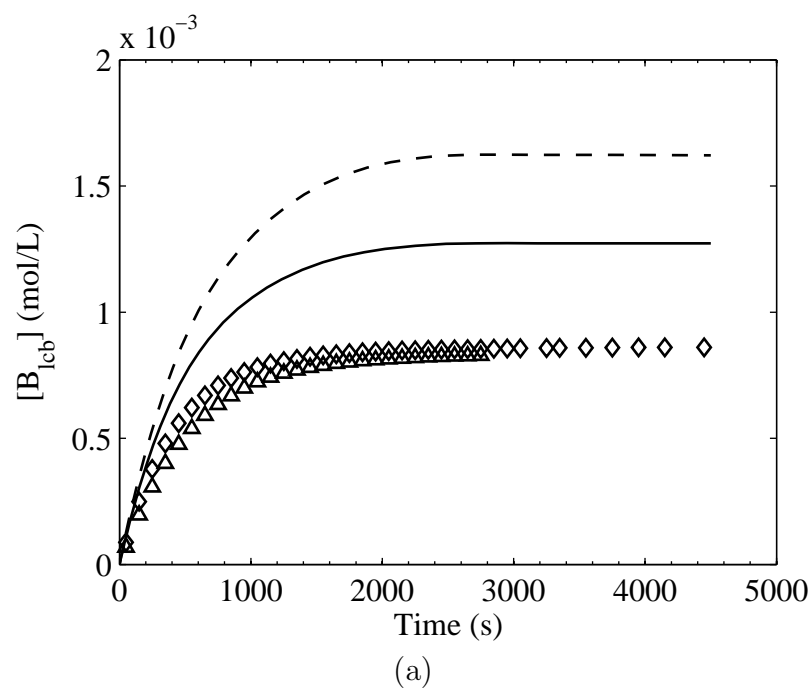


Figure 49: (a) Long-chain branch concentrations at $L_{cut} = 25$, from KMC simulations for system radii of 100 nm (triangle) and 200 nm (diamond) and from rate-equation model, determined both with (solid line) and without (dashed line) backbiting as a branch-stopping event; (b) $z_{p/bb}$, the number of propagation events per backbiting event, calculated from Equation (56).

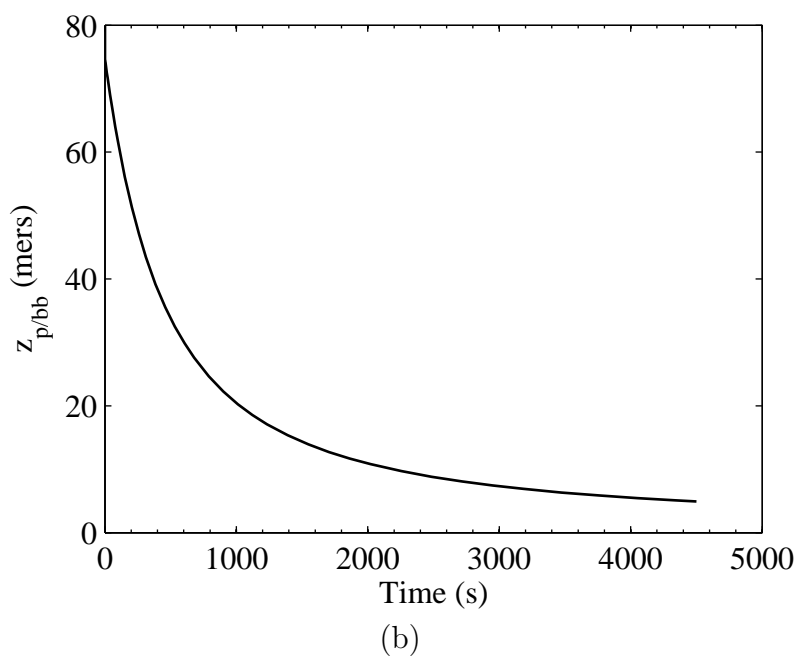
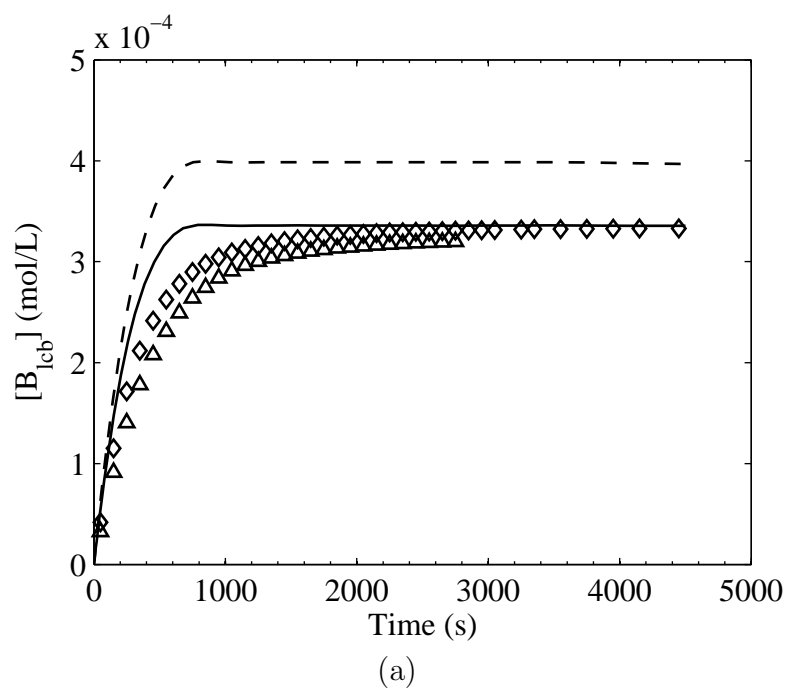
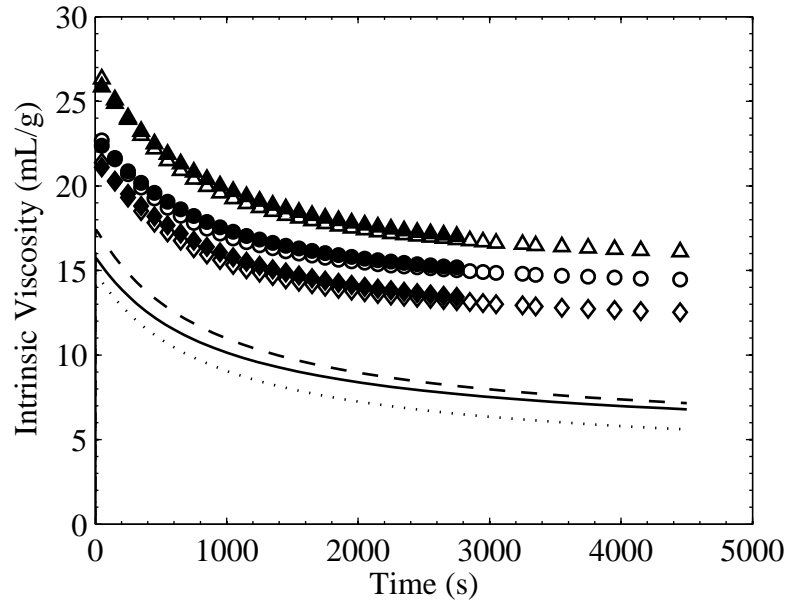


Figure 50: (a) Long-chain branch concentrations at $L_{cut} = 40$, from KMC simulations for system radii of 100 nm (triangle) and 200 nm (diamond) and from rate-equation model, determined both with (solid line) and without (dashed line) backbiting as a branch-stopping event; (b) $z_{p/bb}$, the number of propagation events per backbiting event, calculated from Equation (56).

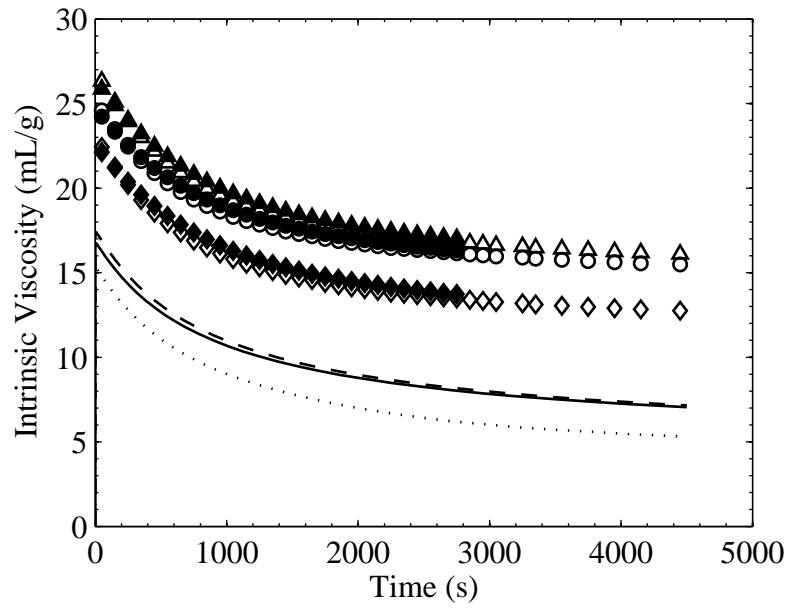
decreases as the minimum length L_{cut} for a long-chain branch is increased, following from the result that the majority of branches are produced by backbiting and about 80% of the branches formed by backbiting are less than 10 mers in length. For all three values of L_{cut} , the long-chain branch concentration from the KMC simulations quickly reaches a plateau, with the start of this plateau becoming earlier as L_{cut} is increased. Figure 17(a) shows a case where $z_{p/bb}$ is greater than L_{cut} , and Figure 17(b) shows a case where $z_{p/bb}$ is less than L_{cut} . In both the rate-equation model and the KMC simulations, once $z_{p/bb}$ drops below L_{cut} , formation of long-chain branches slows and eventually stops, an effect that is clearly observable in Figure 49(a) and 50(a), although the rate-equation model reaches a plateau later than the KMC simulations. Noting that the y-axes are scaled differently in Figure 48(a), 49(a), and 50(a), the gap between the plateaus of the rate-equation model and KMC simulations decreases as the value of L_{cut} is increased. This gap is less obvious in Figure 48(a) due to the longer time required for both models to reach a plateau value. As shown in Figure 50(a), when L_{cut} is increased to 40, the plateau of the rate-equation model including backbiting as a branch-stopping event approaches the plateau from the 200-nm KMC simulations, at longer times. Backbiting, as a branch-stopping event, is clearly significant in determining the plateau value of long-chain branching in the KMC simulations, but there are remaining effects occurring in the KMC simulations which are not captured in the rate-equation model.

7.4 Viscosity Predictions

In Figure 51 and 52, there is an obvious difference between the viscosity predictions of the rate-equation and KMC simulations. This difference is due to the molecular weight used in the Mark-Houwink-Sakurada equation to determine the linear-chain viscosity. While the viscosity-average molecular weight M_v may be calculated in the KMC simulations since the length of each chain is known, the rate-equation model



(a)



(b)

Figure 51: Intrinsic viscosity predicted from simulations at (a) $L_{cut} = 10$ and (b) $L_{cut} = 25$, showing predictions of rate-equation model as $[\eta_l]$ (dashed line), $[\eta_b]$ (solid line), and $[\eta_{corr}]$ (dotted line); predictions of 100-nm radius KMC simulations as $[\eta_l]$ (filled triangle), $[\eta_b]$ (filled circle), and $[\eta_{corr}]$ (filled diamond); and predictions of 200-nm radius KMC simulations as $[\eta_l]$ (open triangle), $[\eta_b]$ (open circle), and $[\eta_{corr}]$ (open diamond).

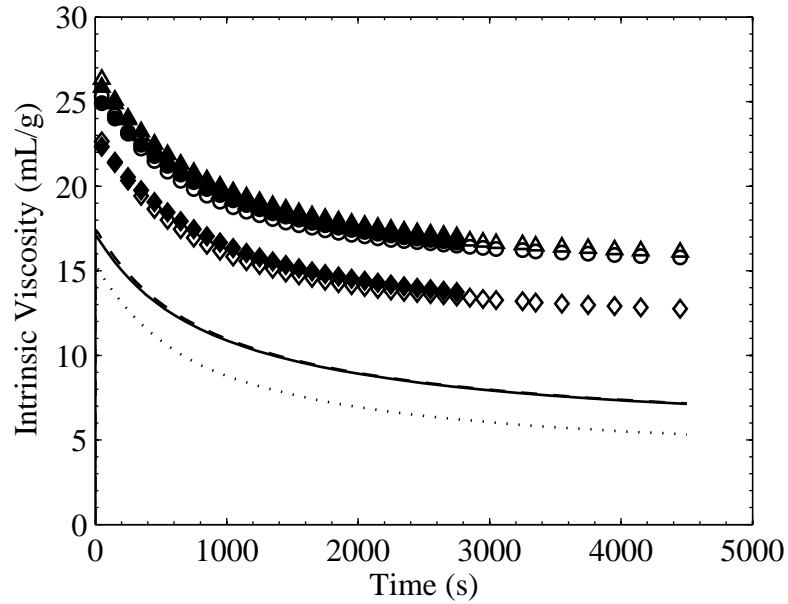


Figure 52: Intrinsic viscosity predicted from simulations at $L_{cut} = 40$, showing predictions of rate-equation model as $[\eta_l]$ (dashed line), $[\eta_b]$ (solid line), and $[\eta_{corr}]$ (dotted line); predictions of 100-nm radius KMC simulations as $[\eta_l]$ (filled triangle), $[\eta_b]$ (filled circle), and $[\eta_{corr}]$ (filled diamond); and predictions of 200-nm radius KMC simulations as $[\eta_l]$ (open triangle), $[\eta_b]$ (open circle), and $[\eta_{corr}]$ (open diamond).

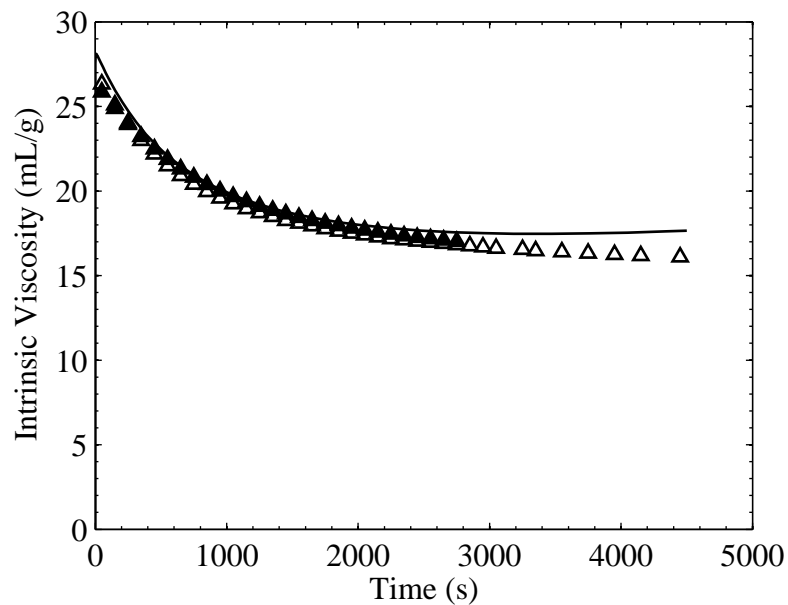


Figure 53: Linear-chain intrinsic viscosity from KMC simulations using system radii of 100 nm (filled triangle) and 200 nm (open triangle) compared to intrinsic viscosity obtained from rate-equation model with molecular weight scaled by the polydispersity from 200-nm radius KMC simulations.

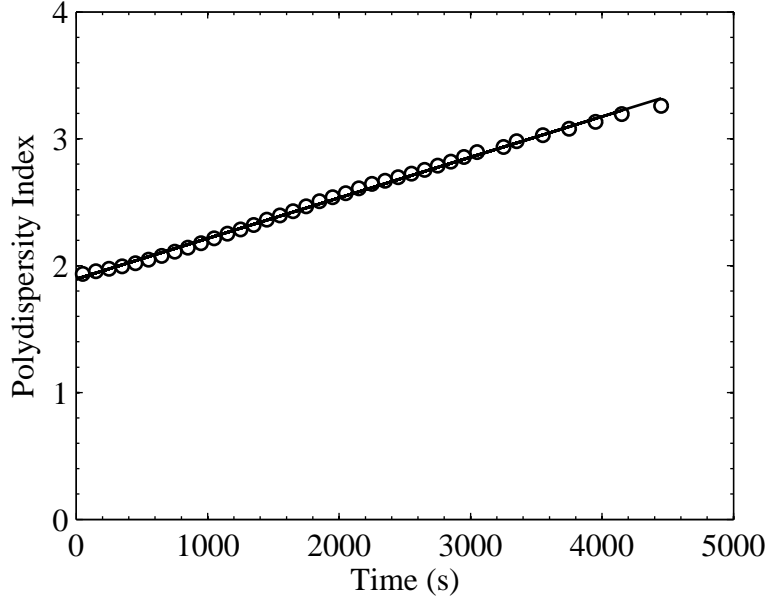


Figure 54: Polydispersity index obtained from KMC simulations using system radius of 200 nm (circle) and corresponding linear fit, $3.2 \times 10^{-4}t + 1.90$ with $R^2 = 0.997$.

substitutes the number-average molecular weight M_n in place of M_v , so the resulting linear-chain viscosity is significantly lower for the rate-equation model. Figure 53 shows the linear-chain intrinsic viscosity obtained from the rate-equation model when M_n is scaled using a linear fit of the polydispersity obtained from the 200-nm KMC simulations, which provides an estimate of the weight-average molecular weight M_w for the rate-equation model. The polydispersity index from the 200-nm KMC simulations and its linear fit are shown in Figure 54. Using this estimate of M_w in the Mark-Houwink-Sakurada equation gives a linear-chain viscosity for the rate-equation model that is near the intrinsic viscosity calculated from the KMC simulations, showing that that the difference in molecular weight is the primary cause for the discrepancy between the models in Figure 51 and 52. The KMC model therefore provides a more accurate prediction of the intrinsic viscosity, especially as the system size is increased to reduce the effects of confinement. The effects of long-chain and short-chain branching are similar for the rate-equation and KMC simulations. Long-chain branching reduces the predicted intrinsic viscosity, and increasing the value

of L_{cut} brings the long-chain-branched viscosity closer to the linear-chain intrinsic viscosity, as the concentration of branches classified as long-chain branches becomes smaller. Including the effects of both short-chain and long-chain branching causes a further decrease in the predicted intrinsic viscosity, but this prediction is relatively insensitive to the value of L_{cut} .

7.5 Conclusions

The well-mixed KMC model allows examination of the effects of radical confinement on branching. Comparison of the KMC simulation results to the experimental data and the results of the rate-equation model shows that confinement of radicals reduces both the conversion rate and the degree of branching, due to a decreased radical lifetime. For the experimental conditions used here [79], the number-average molecular weight is essentially unchanged by radical confinement, since the rate of chain transfer to solvent, the dominant chain-stopping event, is unaffected by confinement. Branch-length distribution is more readily studied using the KMC model as compared to the rate-equation model, due to the details in the branching topology of individual chains which may affect the length of branches produced by both backbiting and intermolecular chain transfer to polymer. The KMC model also improves the prediction of intrinsic viscosity, as the viscosity-average molecular weight is easily computed when the length of each chain in the system is known. The key finding from the previous chapter, that backbiting is overwhelmingly dominant in branch formation even at polymer concentrations where polymer coils may overlap, holds true for the KMC simulation results. Although the KMC model is more computationally intensive than the rate-equation model, the accessibility of microstructural details and the availability of distributions for systems containing many chains make the KMC model better suited for the simulation of branch length.

CHAPTER VIII

CONCLUSIONS AND FUTURE DIRECTIONS

8.1 Conclusions

At the outset of this project, the spatially-resolved kinetic Monte Carlo (KMC) model was considered to be the only model necessary for studying molecular-level mechanisms such as those examined in this work, and the simultaneous reaction and diffusion of polymer chains was viewed as a major advantage of the spatially-resolved model, allowing inherent approximations of diffusion-limited reactions such as termination and at high conversion, propagation. Diffusion of oligomers was simulated on the lattice with measurable success, once the reptation event was incorporated into the model, and trends of diffusivity versus oligomer length found in the literature [51] were reproduced after some tuning of the rate constants for reptation and bond fluctuation. Incorporation of reactions alongside diffusion followed next, but the issue of extreme model stiffness quickly became obvious, as the events of reptation and bond fluctuation occur on a scale about 10^6 times faster than the reactions. Invoking the “tau-leaping” algorithm [50] reduced this difference in time scales such that diffusion was only 10 or 100 times faster than the fastest reaction, but simulations of polymerization in a 100-nm diameter miniemulsion particle still required over a month to reach monomer conversions between 75–90%. The inefficiency of the spatially-resolved model for simulating a full complement of reactions had become apparent, so the effects of diffusion on the nucleation mechanisms of oil-soluble initiators, the study underway at the time, were reconsidered. Realizing that the diffusive effects on reactions such as termination are minimal at lower polymer concentrations, the well-mixed assumption, an extension of the “tau-leaping” algorithm, was invoked, and the

well-mixed KMC model was created. Simulation of diffusion-dependent events such as radical desorption and termination is simplified in the well-mixed model, and the results need only be interpreted in light of the primary limitation, that the well-mixed assumption does not necessarily hold true at higher conversions.

The well-mixed KMC model has proven to be a useful tool for examining the nucleation mechanisms of oil-soluble initiators in styrene miniemulsion polymerization, stripping away the zero-one assumption and leaving in its place only a few reasonably justified assumptions regarding individual reactive events, assumptions which are unlikely to have a major impact on the predicted molecular-weight distribution and therefore are unlikely to impact the conclusions of the study. Multi-modal molecular-weight distributions, which might require a high number of moments to simulate using a rate-equation model, are easily obtained from the well-mixed KMC model without requiring any adjustments to the model algorithm. Overlapping and minor modes of the molecular weight distribution become more obvious, thereby allowing for clearer observation of the presence of certain chain-stopping events.

The combination of models employed to study the branch-length distribution in butyl acrylate solution polymerization leveraged the advantages of each model to examine the significance of backbiting and other reactions on the both the amount and length of branches. The spatially-resolved model provided an appropriate platform for determining the branch lengths achievable through backbiting, leading to the construction of the backbiting cumulative distribution function (CDF), which permitted removal of the common assumption that backbiting only produces short-chain branches, and ultimately led to the larger study of branch-length distribution. Prediction of the amounts of short-chain and long-chain branching is more direct with the well-mixed KMC model, where the detailed branching topology of each chain is simulated. While the rate-equation model is much more efficient at predicting the

amounts of short-chain and long-chain branching, its assumption of a simple branching topology does not capture all of the microstructural features that affect branch length. Physical properties such as intrinsic viscosity are also more readily determined using distributions available in the well-mixed KMC model.

Models that allow for simulation across multiple length and time scales permit simultaneous examination of detailed molecular mechanisms and prediction of experimental observables such as monomer conversion and molecular-weight distribution, providing insight into microstructural features that are often not observable through laboratory experiments. Combining multiple modeling techniques to study a particular system or mechanism, with consideration to the objectives of the study, can provide a more thorough exploration of the system variables and produce a more efficient modeling methodology. Further refinement of these modeling techniques toward examining the microstructure of polymers will become possible only as finer resolutions of measurement are achieved through the advancement of experimental techniques.

8.2 Future Directions

Particle morphology in emulsion or miniemulsion polymerization is an aspect that, although initially envisioned for the spatially-resolved model, was not ultimately part of this thesis. The assembly of core-shell particles using triblock copolymers is an intriguing topic, as the chemical bonding between the core and shell, depicted in Figure 55(b), could improve the effectiveness of core-shell particles in applications such as adhesives and impact modifiers. Such particles have been successfully synthesized using a difunctional surface-active initiator and a surface-active reversible addition-fragmentation chain transfer (RAFT) agent [76]. The growth of entire chains from the core through the second layer is accomplished by using a RAFT agent to maintain living radical polymerization. If both surface-active RAFT agent and surface-active

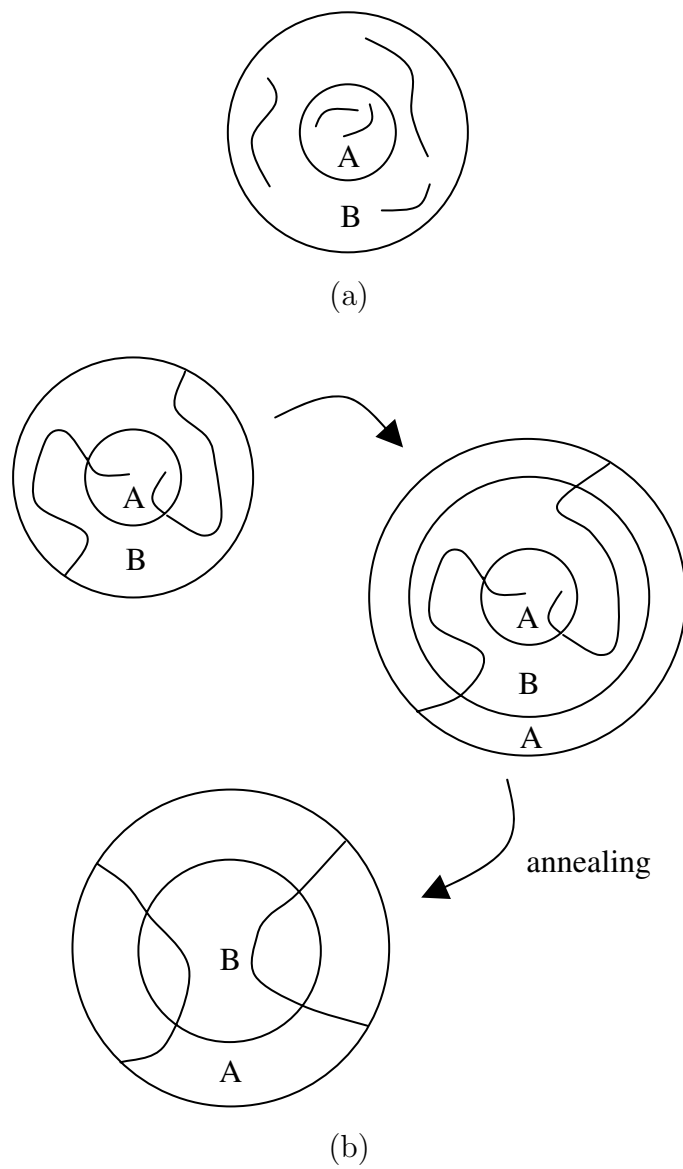


Figure 55: Possible core-shell particle structures using monomers of types A and B (a) with separate polymer chains in the core and shell and (b) using a combination of surface-active initiator and RAFT agent to grow triblock copolymer chains through three layers, followed by annealing.

initiator are excluded from the particles, then most of the radicals will terminate before the second stage of the process, thus preventing the growth of diblock or triblock copolymers. With the inclusion of both a difunctional surface-active initiator and a surface active RAFT agent, the core of monomer type A may be converted with a polydispersity near 1.0, then the surface radicals propagate outward to form the first shell using monomer type B, and finally the second shell is formed using monomer type A. In order for the layers of the particle to remain separated, monomers A and B must be relatively insoluble in one another. After the polymerization is completed, the particle is annealed so that the mers in the core and second shell diffuse together, driven by the decrease in free energy resulting from the minimization of the surface area between the two phases.

Using only the spatially-resolved model, simulating the growth of a triblock copolymer and the formation of the core-shell structure through annealing would be highly computationally expensive. Anchoring of the initiator end group to the surface of the particle would likely prevent full conversion of the core, and even if that could be achieved, maintaining end groups at the outer surface of the first shell could pose problems as the radicals propagate through the FCC lattice. Dividing this simulation effort between the well-mixed KMC and spatially-resolved models would allow for a more efficient simulation procedure, as the polymerization could be simulated off-lattice using the well-mixed KMC simulation. Then, chains could be sampled from a distribution of block lengths and molecular weights and placed on the FCC lattice. The annealing process could be simulated by weighting the bond fluctuation and reptation events so that mers are more likely to diffuse towards other mers of the same type.

The ultimate goal for most modeling efforts is to develop some type of reduced-order process model that is capable of making stand-alone predictions of product properties based on the processing conditions, so that such a model can be applied for

process control. The modeling efforts presented in this work do not consider changes in process variables such as temperature or initiator concentration. Although, as for the modeling studies of butyl acrylate solution polymerization, nominal rate constants may provide a reasonable reproduction of experimental or process data, certain factors such as initiator efficiency remain somewhat ambiguous and can only be accounted for by updating a model according to experimental or process data. Further studies should be performed to examine the robustness of the models used in this work to changes in process conditions. Key mechanisms affecting such properties as long-chain branching or molecular weight must be extracted from the KMC simulations and applied to more computationally efficient models such as the rate-equation model if process models are to be developed to account for variations in chain microstructure. The comparisons made in this work between the rate-equation and well-mixed KMC models show that such model reduction may be achievable, but many aspects of these models remain to be considered before a process model can be realized.

REFERENCES

- [1] ABE, A. and FURUYA, H., "Orientational characteristics of main-chain polymer liquid-crystals as revealed by the rotational isomeric state analysis of deuterium NMR-spectra," *Macromolecules*, vol. 22, no. 7, pp. 2982–2987, 1989.
- [2] ACHILIAS, D. and KIPARISSIDES, C., "Modeling of diffusion-controlled free-radical polymerization reactions," *Journal of the American Chemical Society*, vol. 35, no. 5, pp. 1303–1323, 1988.
- [3] ACHILIAS, D. S. and KIPARISSIDES, C., "Development of a general mathematical framework for modeling diffusion-controlled free-radical polymerization reactions," *Macromolecules*, vol. 25, no. 14, pp. 3739–3750, 1992.
- [4] AHMAD, N. M., HEATLEY, F., and LOVELL, P. A., "Chain transfer to polymer in free-radical solution polymerization of n-butyl acrylate studied by NMR spectroscopy," *Macromolecules*, vol. 31, no. 9, pp. 2822–2827, 1998.
- [5] AHMAD, N. M., LOVELL, P. A., and UNDERWOOD, S. M., "Viscoelastic properties of branched polyacrylate melts," *Polymer International*, vol. 50, no. 6, pp. 625–634, 2001.
- [6] ALDUNCIN, J. A. and ASUA, J. M., "Molecular-weight distributions in the miniemulsion polymerization of styrene initiated by oil-soluble initiators," *Polymer*, vol. 35, no. 17, pp. 3758–3765, 1994.
- [7] ALLEN, M. P. and TILDESLEY, D. J., *Computer Simulation of Liquids*. New York: Oxford University Press, 1987.
- [8] ARCOS-CASARRUBIAS, J. A. and OLAYO, R., "Self-diffusion of styrene, 2,2'-azobisisobutyronitrile, and polystyrene in bulk polymerization by pulsed-gradient spin-echo nuclear magnetic resonance spectroscopy," *Journal of Polymer Science, Part B: Polymer Physics*, vol. 41, no. 14, pp. 1605–1614, 2003.
- [9] ARZAMENDI, G. and LEIZA, J. R., "Molecular weight distribution (soluble and insoluble fraction) in emulsion polymerization of acrylate monomers by Monte Carlo simulations," *Industrial & Engineering Chemistry Research*, vol. 47, no. 16, pp. 5934–5947, 2008.
- [10] ARZAMENDI, G., PLESSIS, C., LEIZA, J. R., and ASUA, J. M., "Effect of the intramolecular chain transfer to polymer on PLP/SEC experiments of alkyl acrylates," *Macromolecular Theory and Simulations*, vol. 12, no. 5, pp. 315–324, 2003.

- [11] ASUA, J. M., “Miniemulsion polymerization,” *Progress in Polymer Science*, vol. 27, no. 7, pp. 1283–1346, 2002.
- [12] ASUA, J. M., BEUERMANN, S., BUBACK, M., CASTIGNOLLES, P., CHARLEUX, B., GILBERT, R. G., HUTCHINSON, R. A., LEIZA, J. R., NIKITIN, A. N., VAIRON, J. P., and VAN HERK, A. M., “Critically evaluated rate coefficients for free-radical polymerization, 5: Propagation rate coefficient for butyl acrylate,” *Macromolecular Chemistry and Physics*, vol. 205, no. 16, pp. 2151–2160, 2004.
- [13] ASUA, J. M., RODRIGUEZ, V. S., SUDOL, E. D., and EL-AASSER, M. S., “The free-radical distribution in emulsion polymerization using oil-soluble initiators,” *Journal of Polymer Science, Part A: Polymer Chemistry*, vol. 27, no. 11, pp. 3569–3587, 1989.
- [14] BAI, Y. P., L., Z., and SHAO, L., “Hybrid emulsifiers enhancing polymerization stabilities and properties of pressure sensitive adhesives,” *Journal of Applied Polymer Science*, vol. 115, no. 2, pp. 1125–1130, 2010.
- [15] BAMFORD, C. H., BARB, W. G., JENKINS, A. D., and ONYON, P. F., *The Kinetics of Vinyl Polymerization by Radical Mechanisms*. New York: Academic Press, 1958.
- [16] BAMFORD, C. H., DYSON, R. W., and EASTMOND, G. C., “Network formation, 4: The nature of the termination reaction in free-radical polymerization,” *Polymer*, vol. 10, no. 11, pp. 885–899, 1969.
- [17] BARAN, E. T., OZER, N., and HASIRCI, V., “Poly(hydroxybutyrate-co-hydroxyvalerate) nanocapsules as enzyme carriers for cancer therapy: An in vitro study,” *Journal of Microencapsulation*, vol. 19, no. 3, pp. 363–376, 2002.
- [18] BARNER-KOWOLLIK, C., GUENZLER, F., and JUNKERS, T., “Pushing the limit: Pulsed laser polymerization of n-butyl acrylate at 500 hz,” *Macromolecules*, vol. 41, no. 23, pp. 8971–8973, 2008.
- [19] BEUERMANN, S. and BUBACK, M., “Rate coefficients of free-radical polymerization deduced from pulsed laser experiments,” *Progress in Polymer Science*, vol. 27, no. 2, pp. 191–254, 2002.
- [20] BEUERMANN, S., BUBACK, M., DAVIS, T. P., GILBERT, R. G., HUTCHINSON, R. A., OLAJ, O. F., RUSSELL, G. T., SCHWEER, J., and VANHERK, A. M., “Critically evaluated rate coefficients for free-radical polymerization, 2: Propagation rate coefficients for methyl methacrylate,” *Macromolecular Chemistry and Physics*, vol. 198, no. 5, pp. 1545–1560, 1997.
- [21] BILLMEYER, F. W. J., *Textbook of Polymer Science*. New York: Wiley, 3rd ed., 1984.

- [22] BINDER, K., BASCHNAGEL, J., and PAUL, W., "Glass transition of polymer melts: test of theoretical concepts by computer simulation," *Progress in Polymer Science*, vol. 28, no. 1, pp. 115–172, 2003.
- [23] BITSANIS, I. and HADZIOANNOU, G., "Molecular-dynamics simulations of the structure and dynamics of confined polymer melts," *Journal Of Chemical Physics*, vol. 92, no. 6, pp. 3827–3847, 1990.
- [24] BLOMQVIST, J., PIETILA, L. O., and MANNFORS, B., "RIS Metropolis Monte Carlo studies of some aliphatic main chain and side group polyesters," *Polymer*, vol. 42, no. 1, pp. 109–116, 2001.
- [25] BOVEY, F. A., SCHILLING, F. C., MCCRACKIN, F. L., and WAGNER, H. L., "Short-chain and long-chain branching in low-density polyethylene," *Macromolecules*, vol. 9, no. 1, pp. 76–80, 1976.
- [26] BRANDRUP, J., IMMERGUT, E. H., and GRULKE, E. A., eds., *Polymer Handbook*. New York: Wiley, 4th ed., 1999.
- [27] BREITENBACH, J. W. and SCHINDLER, A., "Polymerisationskinetische versuche mit alpha-azoisobuttersaurenitril und benzoylperoxyd an styrol zur aufklarung der geschwindigkeit von start und ubertragungsreaktion," *Monatshefte fuer Chemie*, vol. 83, no. 3, pp. 724–730, 1952.
- [28] BUBACK, M., GILBERT, R. G., HUTCHINSON, R. A., KLUMPERMAN, B., KUCHTA, F. D., MANDERS, B. G., O'DRISCOLL, K. F., RUSSELL, G. T., and SCHWEER, J., "Critically evaluated rate coefficients for free-radical polymerization, 1: Propagation rate coefficient for styrene," *Macromolecular Chemistry and Physics*, vol. 196, no. 10, pp. 3267–3280, 1995.
- [29] BUTTE, A., STORTI, G., and MORBIDELLI, M., "Miniemulsion living free radical polymerization by RAFT," *Macromolecules*, vol. 34, no. 17, pp. 5885–5896, 2001.
- [30] BUTTE, A., STORTI, G., and MORBIDELLI, M., "Evaluation of the chain length distribution in free-radical polymerization, 1: Bulk polymerization," *Macromolecular Theory And Simulations*, vol. 11, no. 1, pp. 22–36, 2002.
- [31] BUTTE, A., STORTI, G., and MORBIDELLI, M., "Evaluation of the chain length distribution in free-radical polymerization, 2: Emulsion polymerization," *Macromolecular Theory And Simulations*, vol. 11, no. 1, pp. 37–52, 2002.
- [32] CARMESIN, I. and KREMER, K., "The bond fluctuation method: A new effective algorithm for the dynamics of polymers in all spatial dimensions," *Macromolecules*, vol. 21, no. 9, pp. 2819–2823, 1988.
- [33] CAROTHERS, W. H., "Polymers and polyfunctionality," *Transactions of the Faraday Society*, vol. 32, no. 1, pp. 39–49, 1936.

- [34] CASTIGNOLLES, P., GRAF, R., PARKINSON, M., WILHELM, M., and GABORIEAU, M., “Detection and quantification of branching in polyacrylates by size-exclusion chromatography (SEC) and melt-state ^{13}C NMR spectroscopy,” *Polymer*, vol. 50, no. 11, pp. 2373–2383, 2009.
- [35] CHATTERJEE, A. and VLACHOS, D. G., “An overview of spatial microscopic and accelerated kinetic Monte Carlo methods,” *Journal of Computer-Aided Material Design*, vol. 14, no. 2, pp. 253–308, 2007.
- [36] CHERN, C. S. and POEHLEIN, G. W., “Polymerization in nonuniform latex-particles: Distribution of free-radicals,” *Journal of Polymer Science, Part A: Polymer Chemistry*, vol. 25, no. 2, pp. 617–635, 1987.
- [37] CLANCY, T. C. and MATTICE, W. L., “Rotational isomeric state chains on a high coordination lattice: Dynamic monte carlo algorithm details,” *Journal of Chemical Physics*, vol. 112, no. 22, pp. 10049–10055, 2000.
- [38] CLOIZEAUX, J. D., “Relaxation of entangled and partially entangled polymers in melts: Time-dependent reptation,” *Macromolecules*, vol. 25, no. 2, pp. 835–841, 1992.
- [39] DE GENNES, P. G., “Reptation of a polymer chain in the presence of fixed obstacles,” *Journal of Chemical Physics*, vol. 55, no. 2, pp. 572–579, 1971.
- [40] DONG, Y. and SUNDBERG, D. C., “Radical entry in emulsion polymerization: Estimation of the critical length of entry radicals via a simple lattice model,” *Macromolecules*, vol. 35, no. 21, pp. 8185–8190, 2002.
- [41] ERDEM, B., SUDOL, E. D., DIMONIE, V. L., and EL-AASSER, M. S., “Encapsulation of inorganic particles via miniemulsion polymerization, 1: Dispersion of titanium dioxide particles in organic media using OLOA 370 as stabilizer,” *Journal of Polymer Science, Part A: Polymer Chemistry*, vol. 38, no. 24, pp. 4419–4430, 2000.
- [42] ERDEM, B., SUDOL, E. D., DIMONIE, V. L., and EL-AASSER, M. S., “Encapsulation of inorganic particles via miniemulsion polymerization, 2: Preparation and characterization of styrene miniemulsion droplets containing TiO_2 particles,” *Journal of Polymer Science, Part A: Polymer Chemistry*, vol. 38, no. 24, pp. 4431–4440, 2000.
- [43] ERDEM, B., SUDOL, E. D., DIMONIE, V. L., and EL-AASSER, M. S., “Encapsulation of inorganic particles via miniemulsion polymerization, 3: Characterization of encapsulation,” *Journal of Polymer Science, Part A: Polymer Chemistry*, vol. 38, no. 24, pp. 4441–4450, 2000.
- [44] FICHTHORN, K. A. and WEINBERG, W. H., “Theoretical foundations of dynamic Monte-Carlo simulations,” *Journal of Chemical Physics*, vol. 95, no. 2, pp. 1090–1096, 1991.

- [45] FLORY, P. J., “Molecular size distribution in three dimensional polymers, 1: Gelation,” *Journal of the American Chemical Society*, vol. 63, pp. 3083–3090, 1941.
- [46] FLORY, P. J., “The configuration of real polymer chains,” *Journal of Chemical Physics*, vol. 17, no. 3, pp. 303–310, 1949.
- [47] FLORY, P. J., “Foundations of rotational isomeric state theory and general methods for generating configurational averages,” *Macromolecules*, vol. 7, no. 3, pp. 381–392, 1974.
- [48] FORMER, C., CASTRO, J., FELLOWS, C. M., TANNER, R. I., and GILBERT, R. G., “Effect of branching and molecular weight on the viscoelastic properties of poly(butyl acrylate),” *Journal of Polymer Science, Part A: Polymer Chemistry*, vol. 40, no. 20, pp. 3335–3349, 2002.
- [49] FRIIS, N. and HAMIELEC, A. E., “Kinetics of vinyl-chloride and vinyl-acetate emulsion polymerization,” *Journal Of Applied Polymer Science*, vol. 19, no. 1, pp. 97–113, 1975.
- [50] GILLESPIE, D. T., “Approximate accelerated stochastic simulation of chemically reacting systems,” *Journal of Chemical Physics*, vol. 115, no. 4, pp. 1716–1733, 2001.
- [51] GRIFFITHS, M. C., STRAUCH, J., MONTEIRO, M. J., and GILBERT, R. G., “Measurement of diffusion coefficients of oligomeric penetrants in rubbery polymer matrixes,” *Macromolecules*, vol. 31, no. 22, pp. 7835–7844, 1998.
- [52] HAGE, E., HALE, W., KESKKULA, H., and PAUL, D. R., “Impact modification of poly(butylene terephthalate) by ABS materials,” *Polymer*, vol. 38, no. 13, pp. 3237–3250, 1997.
- [53] HESS, W., “Self-diffusion and reptation in semidilute polymer solutions,” *Macromolecules*, vol. 19, no. 5, pp. 1395–1404, 1986.
- [54] HESS, W., “Generalized Rouse theory for entangled polymeric liquids,” *Macromolecules*, vol. 21, no. 8, pp. 2620–2632, 1988.
- [55] HESSE, P. PhD thesis, University of Gottingen, 2008.
- [56] IEDEMA, P. D., GRCEV, S., and HOEFSLOOT, H. C. J., “Molecular weight distribution modeling of radical polymerization in a CSTR with long chain branching through transfer to polymer and terminal double bond (TDB) propagation,” *Macromolecules*, vol. 36, no. 2, pp. 458–476, 2003.
- [57] IEDEMA, P. D. and HOEFSLOOT, H. C. J., “Conditional Monte Carlo sampling to find branching architectures of polymers from radical polymerizations with transfer to polymer,” *Macromolecules*, vol. 39, no. 8, pp. 3081–3088, 2006.

- [58] KARLSSON, O. J., STUBBS, J. M., CARRIER, R. H., and SUNDBERG, D. C., “Dynamic modeling of non-equilibrium latex particle morphology development during seeded emulsion polymerization,” *Polymer Reaction Engineering*, vol. 11, no. 4, pp. 589–625, 2003.
- [59] KARYAPPA, R. B. and NATARAJAN, U., “Monte Carlo simulations of chain dimensions and conformational properties of various poly(n-alkyl methacrylates) in solution,” *Journal of Macromolecular Science, Part B: Physics*, vol. 47, no. 6, pp. 1075–1086, 2008.
- [60] KHOLODENKO, A. L., “Reptation theory: Geometrical and topological aspects,” *Macromolecular Theory and Simulations*, vol. 5, no. 6, pp. 1031–1064, 1996.
- [61] KIM, D. M. and IEDEMA, P. D., “Modeling of branching density and branching distribution in low-density polyethylene polymerization,” *Chemical Engineering Science*, vol. 63, no. 8, pp. 2035–2046, 2008.
- [62] KRALLIS, A. and KIPARISSIDES, C., “Mathematical modeling of the bivariate molecular weight – long chain branching distribution of highly branched polymers. A population balance approach,” *Chemical Engineering Science*, vol. 62, no. 18–20, Sp. Iss. SI, pp. 5304–5311, 2007.
- [63] KRAUS, G. and STACY, C. J., “Method for characterization of long-chain branched polymers by GPC and intrinsic viscosity,” *Journal of Polymer Science: Polymer Symposia*, no. 43, pp. 329–343, 1973.
- [64] KREMER, K. and GREST, G. S., “Dynamics of entangled linear polymer melts: A molecular-dynamics simulation,” *Journal Of Chemical Physics*, vol. 92, no. 8, pp. 5057–5086, 1990.
- [65] KRYWKO, W. P., MCAULEY, K. B., and CUNNINGHAM, M. F., “Mathematical modeling of particle morphology development induced by radical concentration gradients in seeded styrene homopolymerization,” *Polymer Reaction Engineering*, vol. 10, no. 3, pp. 135–161, 2002.
- [66] LANE, W. H., “Determination of the solubility of styrene in water and of water in styrene,” *Industrial and Engineering Chemistry-Analytical Edition*, vol. 18, no. 5, pp. 295–296, 1946.
- [67] LIU, Y., SCHROEDER, W. F., HALEY, J. C., LAU, W., and WINNIK, M. A., “Effect of branching on polymer diffusion in branched poly(butyl methacrylate) latex films,” *Macromolecules*, vol. 41, no. 23, pp. 9104–9111, 2008.
- [68] LOVELL, P. A., “Personal communication.” Sept. 2009.
- [69] LUO, Y. W. and YU, B., “Monte Carlo simulation of droplet nucleation in RAFT free radical miniemulsion polymerization,” *Polymer-Plastics Technology and Engineering*, vol. 43, no. 5, pp. 1299–1321, 2004.

- [70] MAEDER, S. and GILBERT, R. G., “Measurement of transfer constant for butyl acrylate free-radical polymerization,” *Macromolecules*, vol. 31, no. 14, pp. 4410–4418, 1998.
- [71] MATHESON, M. S., AUER, E. E., BEVILACQUA, E. B., and HART, E. J., “Rate constants in free radical polymerization, 3: Styrene,” *Journal of the American Chemical Society*, vol. 73, no. 4, pp. 1700–1706, 1951.
- [72] MATSUMOTO, M. and NISHIMURA, T., “Mersenne twister: a 623-dimensionally equidistributed uniform pseudo-random number generator,” *ACM Transactions on Modeling and Computer Simulation*, vol. 8, no. 1, pp. 3–30, 1998.
- [73] MILCHEV, A., PAUL, W., and BINDER, K., “Off-lattice Monte-Carlo simulation of dilute and concentrated polymer solutions under theta conditions,” *Journal Of Chemical Physics*, vol. 99, no. 6, pp. 4786–4798, 1993.
- [74] MILLS, M. F., GILBERT, R. G., and NAPPER, D. H., “Effect of polymerization kinetics on particle morphology in heterogeneous systems,” *Macromolecules*, vol. 23, no. 19, pp. 4247–4257, 1990.
- [75] MOAD, G. and SOLOMON, D. H., *The Chemistry of Radical Polymerization*, ch. Termination, pp. 233–278. Oxford: Elsevier, 2nd ed., 2006.
- [76] MONTEIRO, M. J. and DE BARBEYRAC, J., “Preparation of reactive composite latexes by ‘living’ radical polymerization using the RAFT process. A new class of polymer materials,” *Macromolecular Rapid Communications*, vol. 23, no. 5-6, pp. 370–374, 2002.
- [77] NIKITIN, A. N. and HUTCHINSON, R. A., “Effect of intramolecular transfer to polymer on stationary free radical polymerization of alkyl acrylates, 2: Improved consideration of termination,” *Macromolecular Theory and Simulations*, vol. 15, no. 2, pp. 128–136, 2006.
- [78] NIKITIN, A. N., HUTCHINSON, R. A., BUBACK, M., and HESSE, P., “Determination of intramolecular chain transfer and midchain radical propagation rate coefficients for butyl acrylate by pulsed laser polymerization,” *Macromolecules*, vol. 40, no. 24, pp. 8631–8641, 2007.
- [79] NIKITIN, A. N., HUTCHINSON, R. A., KALFAS, G. A., RICHARDS, J. R., and BRUNI, C., “The effect of intramolecular transfer to polymer on stationary free-radical polymerization of alkyl acrylates, 3: Consideration of solution polymerization up to high conversions,” *Macromolecular Theory and Simulations*, vol. 18, no. 4–5, pp. 247–258, 2009.
- [80] NOMURA, M., IKOMA, J., and FUJITA, K., “Kinetics and mechanisms of emulsion polymerization initiated by oil-soluble initiators, 4: Kinetic

modeling of unseeded emulsion polymerization of styrene initiated by 2,2'-azobisisobutyronitrile," *Journal of Polymer Science, Part A: Polymer Chemistry*, vol. 31, no. 8, pp. 2103–2113, 1993.

- [81] NOMURA, M. and SUZUKI, K., "The kinetic and mechanistic role of oil-soluble initiators in micro- and macroemulsion polymerizations," *Industrial & Engineering Chemistry Research*, vol. 44, no. 8, pp. 2561–2567, 2005.
- [82] ODIAN, G., *Principles of Polymerization*, ch. Radical Chain Polymerization, pp. 198–349. Wiley, 4th ed., 2004.
- [83] PATNODE, W. and SCHEIBER, W. J., "The density, thermal expansion, vapor pressure, and refractive index of styrene, and the density and thermal expansion of polystyrene," *Journal of the American Chemical Society*, vol. 61, no. 12, pp. 3449–3451, 1939.
- [84] PAUL, W., BINDER, K., HEERMANN, D. W., and KREMER, K., "Dynamics of polymer solutions and melts: Reptation predictions and scaling of relaxation-times," *Journal of Chemical Physics*, vol. 95, no. 10, pp. 7726–7740, 1991.
- [85] PERALTA, R. D., INFANTE, R., CORTEZ, G., ELIZALDE, L. E., and WISNIAK, J., "Density, excess volumes and partial volumes of the systems of p-xylene plus ethyl acrylate, butyl acrylate, methyl methacrylate, and styrene at 298.15 K," *Thermochimica Acta*, vol. 421, no. 1–2, pp. 59–68, 2004.
- [86] PICKUP, S. and BLUM, F. D., "Self-diffusion of toluene in polystyrene solutions," *Macromolecules*, vol. 22, no. 10, pp. 3961–3968, 1989.
- [87] PITON, M. C., GILBERT, R. G., CHAPMAN, B. E., and KUCHEL, P. W., "Diffusion of oligomeric species in polymer solutions," *Macromolecules*, vol. 26, no. 17, pp. 4472–4477, 1993.
- [88] PLADIS, P. and KIPARISSIDES, C., "A comprehensive model for the calculation of molecular weight long-chain branching distribution in free-radical polymerizations," *Chemical Engineering Science*, vol. 53, no. 18, pp. 3315–3333, 1998.
- [89] PLESSIS, C., ARZAMENDI, G., LEIZA, J. R., ALBERDI, J. M., SCHOONBROOD, H. A. S., CHARMOT, D., and ASUA, J. M., "Seeded semi-batch emulsion polymerization of butyl acrylate: Effect of the chain-transfer agent on the kinetics and structural properties," *Journal of Polymer Science, Part A: Polymer Chemistry*, vol. 39, no. 7, pp. 1106–1119, 2001.
- [90] PLESSIS, C., ARZAMENDI, G., LEIZA, J. R., SCHOONBROOD, H. A. S., CHARMOT, D., and ASUA, J. M., "Seeded semibatch emulsion polymerization of n-butyl acrylate. Kinetics and structural properties," *Macromolecules*, vol. 33, no. 14, pp. 5041–5047, 2000.

- [91] PLESSIS, C., ARZAMENDI, G., LEIZA, J. R., SCHOONBROOD, H. A. S., CHARMOT, D., and ASUA, J. M., “Kinetics and polymer microstructure of the seeded semibatch emulsion copolymerization of n-butyl acrylate and styrene,” *Macromolecules*, vol. 34, no. 15, pp. 5147–5157, 2001.
- [92] PLESSIS, C., ARZAMENDI, G., LEIZA, J. R., SCHOONBROOD, H. A. S., CHARMOT, D., and ASUA, J. M., “Modeling of seeded semibatch emulsion polymerization of n-BA,” *Industrial & Engineering Chemistry Research*, vol. 40, no. 18, pp. 3883–3894, 2001.
- [93] POLSON, J. M. and GALLANT, J. P., “Equilibrium conformational dynamics of a polymer in a solvent,” *Journal Of Chemical Physics*, vol. 124, no. 18, 2006.
- [94] PRESCOTT, S. W., “Chain-length dependence in living/controlled free-radical polymerizations: Physical manifestation and Monte Carlo simulation of reversible transfer agents,” *Macromolecules*, vol. 36, no. 25, pp. 9608–9621, 2003.
- [95] RAKSHIT, A. and PICU, R. C., “Coarse grained model of entangled polymer melts,” *Journal Of Chemical Physics*, vol. 125, no. 16, 2006.
- [96] RANTOW, F. S., SOROUSH, M., GRADY, M. C., and KALFAS, G. A., “Spontaneous polymerization and chain microstructure evolution in high-temperature solution polymerization of n-butyl acrylate,” *Polymer*, vol. 47, no. 4, pp. 1423–1435, 2006.
- [97] RAPOLD, R. F. and MATTICE, W. L., “New high-coordination lattice model for rotational isomeric state polymer chains,” *Journal of the Chemical Society-Faraday Transactions*, vol. 91, no. 16, pp. 2435–2441, 1995.
- [98] RAPOLD, R. F. and MATTICE, W. L., “Introduction of short and long range energies to simulate real chains on the 2nd lattice,” *Macromolecules*, vol. 29, no. 7, pp. 2457–2466, 1996.
- [99] RAWLSTON, J. A., GUO, J., SCHORK, F. J., and GROVER, M. A., “A kinetic Monte Carlo study on the nucleation mechanisms of oil-soluble initiators in the miniemulsion polymerization of styrene,” *Journal of Polymer Science, Part A: Polymer Chemistry*, vol. 46, no. 18, pp. 6114–6128, 2008.
- [100] RAWLSTON, J. A., SCHORK, F. J., and GROVER, M. A., “Multiscale modeling of branch length in butyl acrylate solution polymerization,” *Macromolecular Theory and Simulations*, 2010. in press.
- [101] RICHTER, D., WILLNER, L., ZIRKEL, A., FARAGO, B., FETTERS, L. J., and HUANG, J. S., “Polymer motion at the crossover from Rouse to reptation dynamics,” *Macromolecules*, vol. 27, no. 25, pp. 7437–7446, 1994.
- [102] ROUSE, P. E., “A theory of the linear viscoelastic properties of dilute solutions of coiling polymers,” *Journal of Chemical Physics*, vol. 21, no. 7, pp. 1272–1280, 1953.

- [103] RUBIO, A. M., STOREY, M., LODGE, J. F. M., and FREIRE, J. J., “Dynamics of bond-fluctuation model chains in good and theta solvents,” *Macromolecular Theory And Simulations*, vol. 11, no. 2, pp. 171–183, 2002.
- [104] RUSSUM, J. P., BARBRE, N. D., JONES, C. W., and SCHORK, F. J., “Miniemulsion reversible addition fragmentation chain transfer polymerization of vinyl acetate,” *Journal of Polymer Science, Part A: Polymer Chemistry*, vol. 43, no. 10, pp. 2188–2193, 2005.
- [105] SCHORK, F. J., LUO, Y. W., SMULDERS, W., RUSSUM, J. P., BUTTE, A., and FONTENOT, K., *Polymer Particles, Advances in Polymer Science*, vol. 175, ch. Miniemulsion Polymerization. Berlin: Springer-Verlag Berlin, 2005.
- [106] SCHWEIZER, K. S., DAVID, E. F., SINGH, C., CURRO, J. G., and RAJASEKARAN, J. J., “Structure-property correlations of atomistic and coarse-grained models of polymer melts,” *Macromolecules*, vol. 28, no. 5, pp. 1528–1540, 1995.
- [107] SHANBHAG, S. and LARSON, R. G., “Identification of topological constraints in entangled polymer melts using the bond-fluctuation model,” *Macromolecules*, vol. 39, no. 6, pp. 2413–2417, 2006.
- [108] SMITH, W. V. and EWART, R. H., “Kinetics of emulsion polymerization,” *Journal of Chemical Physics*, vol. 16, no. 6, pp. 592–599, 1948.
- [109] STARR, F. W., SCHRODER, T. B., and GLOTZER, S. C., “Molecular dynamics simulation of a polymer melt with a nanoscopic particle,” *Macromolecules*, vol. 35, no. 11, pp. 4481–4492, 2002.
- [110] STICKLER, M. and MEYERHOFF, G., “Thermal polymerization of methylmethacrylate, 1: Polymerization in substance,” *Makromolekulare Chemie-Macromolecular Chemistry and Physics*, vol. 179, no. 11, pp. 2729–2745, 1978.
- [111] STOCKMAYER, W. H., “Theory of molecular size distribution and gel formation in branched-chain polymers,” *Journal of Chemical Physics*, vol. 11, no. 2, pp. 45–55, 1943.
- [112] SUDOL, E. D., DANIELS, E. S., and EL-AASSER, M. S., *Polymer Latexes: Preparation, Characterization, and Applications*, vol. ACS Symposium Series 492, ch. Overview of Emulsion Polymerization. Washington, D. C.: American Chemical Society, 1992.
- [113] TAYLOR, T. W. and REICHERT, K. H., “The influence of reactor type and operating-conditions on the molecular-weight distribution in vinyl-acetate polymerization,” *Journal of Applied Polymer Science*, vol. 30, no. 1, pp. 227–250, 1985.

- [114] TEYMOUR, F. and CAMPBELL, J. D., "Analysis of the dynamics of gelation in polymerization reactors using the numerical fractionation technique," *Macromolecules*, vol. 27, no. 9, pp. 2460–2469, 1994.
- [115] TOBITA, H., "Molecular-weight distribution in free-radical polymerization with long-chain branching," *Journal of Polymer Science, Part B: Polymer Physics*, vol. 31, no. 10, pp. 1363–1371, 1993.
- [116] TOBITA, H. and HATANAKA, K., "Branched structure formation in free radical polymerization of vinyl acetate," *Journal of Polymer Science, Part B: Polymer Physics*, vol. 34, no. 4, pp. 671–681, 1996.
- [117] UGELSTAD, J., EL AASSER, M. S., and VANDERHOFF, J. W., "Emulsion polymerization: Initiation of polymerization in monomer droplets," *Journal of Polymer Science, Part C: Polymer Letters*, vol. 11, no. 8, pp. 503–513, 1973.
- [118] VAN LEEMPUT, R. and STEIN, R., "Experimental data on dilute polymer solutions, 1: Hydrodynamic properties and statistical coil dimensions of poly (n-butyl methacrylate)," *Journal of Polymer Science, Part A: General Papers*, vol. 1, no. 3, pp. 985–992, 1963.
- [119] VAN LEEMPUT, R. and STEIN, R., "Experimental data on dilute polymer solutions, 2: Hydrodynamic properties and statistical coil dimensions of poly(n-butyl methacrylate)," *Journal of Polymer Science, Part A: General Papers*, vol. 2, no. 9, pp. 4039–4045, 1964.
- [120] VAN ZYL, A. J. P., SANDERSON, R. D., DE WET-ROOS, D., and KLUMPERMAN, B., "Core/shell particles containing liquid cores: Morphology prediction, synthesis, and characterization," *Macromolecules*, vol. 36, no. 23, pp. 8621–8629, 2003.
- [121] WALL, F., HILLER, L., and WHEELER, D., "Statistical computation of mean dimensions of macromolecules, 1.," *Journal of Chemical Physics*, vol. 22, no. 6, pp. 1036–1041, 1954.
- [122] WEILAND, L. M., LADA, E. K., SMITH, R. C., and LEO, D. J., "Application of rotational isomeric state theory to ionic polymer stiffness predictions," *Journal Of Materials Research*, vol. 20, no. 9, pp. 2443–2455, 2005.
- [123] WITTMER, J. P., CAVALLO, A., KREER, T., BASCHNAGEL, J., and JOHNER, A., "A finite excluded volume bond-fluctuation model: Static properties of dense polymer melts revisited," *Journal Of Chemical Physics*, vol. 131, no. 6, 2009.
- [124] YOUAN, B. B. C., JACKSON, T. L., DICKENS, L., HERNANDEZ, C., and OWUSU-ABABIO, G., "Protein release profiles and morphology of biodegradable microcapsules containing an oily core," *Journal of Controlled Release*, vol. 76, no. 3, pp. 313–326, 2001.

- [125] ZETTERLUND, P. B., SAKA, Y., MCHALE, R., NAKAMURA, T., ALDABAGH, F., and OKUBO, M., "Nitroxide-mediated radical polymerization of styrene: Experimental evidence of chain transfer to monomer," *Polymer*, vol. 47, no. 23, pp. 7900–7908, 2006.
- [126] ZIMM, B. H. and STOCKMAYER, W. H., "The dimensions of chain molecules containing branches and rings," *Journal of Chemical Physics*, vol. 17, no. 12, pp. 1301–1314, 1949.